Durham University

Durham Research Online

Deposited in DRO:

20 September 2019

Version of attached file:

Accepted Version

Peer-review status of attached file:

Peer-reviewed

Citation for published item:

Moghadam, Hadi Shafaii and Stern, R.J. and Griffin, W.L. and Khedr, M.Z. and Kirchenbaur, M. and Ottley, C.J. and Whattam, S. and Kimura, J.-I. and Ghorbani, G. and Gain, S. and O'Reilly, S.Y. and Tamura, A. (2020) 'Subduction initiation and back-arc opening north of Neo-Tethys : evidence from the Late Cretaceous Torbat-e-Heydarieh ophiolite of NE Iran.', GSA bulletin., 132 (5-6). pp. 1083-1105.

Further information on publisher's website:

https://doi.org/10.1130/B35065.1

Publisher's copyright statement:

Additional information:

Use policy

The full-text may be used and/or reproduced, and given to third parties in any format or medium, without prior permission or charge, for personal research or study, educational, or not-for-profit purposes provided that:

- a full bibliographic reference is made to the original source
- a link is made to the metadata record in DRO
- the full-text is not changed in any way

The full-text must not be sold in any format or medium without the formal permission of the copyright holders.

Please consult the full DRO policy for further details.

Durham University Library, Stockton Road, Durham DH1 3LY, United Kingdom
Tel : +44 (0)191 334 3042 | Fax : +44 (0)191 334 2971
https://dro.dur.ac.uk

Subduction initiation and back-arc opening north of Neo-Tethys: Evidence from the Late Cretaceous Torbat-e-Heydarieh ophiolite of NE Iran

Hadi Shafaii Moghadam[1,2*], R.J. Stern[3], W.L. Griffin[2], M.Z. Khedr[4], M. Kirchenbaur[5], C.J. Ottley[6], S. Whattam[7], J.-I. Kimura[8], G. Ghorbani[1], S. Gain[2], S.Y. O'Reilly[2], A. Tamura[9]

[1]*School of Earth Sciences, Damghan University, Damghan 36716-41167, Iran*

[2]*ARC Centre of Excellence for Core to Crust Fluid Systems and GEMOC ARC National Key Centre, Dept. of Earth and Planetary Sciences, Macquarie University, NSW 2109, Australia*

[3]*Geosciences Dept. University of Texas at Dallas, Richardson, TX 75083-0688, USA*

[4]*Dept. of Geology, Faculty of Science, Kafrelsheikh University, 33516 Kafr Elsheikh, Egypt*

[5]*Universitat zu Koln, 50674 Koln, Germany & Steinmann-Institut, Universitat Bonn, Germany*

[6]*Department of Earth Sciences, Northern Centre for Isotopic and Elemental Tracing, University of Durham, Durham, DH1 3LE, UK*

[7] Department of Geosciences, King Fahd University of Petroleum and Minerals, Dhahran 31261, Saudi Arabia

[8]*Department of Solid Earth Geochemistry, Japan Agency for Marine-Earth Science and Technology (JAMSTEC), Natsushima-Cho 2-15, Yokosuka, 237-0061, Japan*

[9]*Department of Earth Sciences, Kanazawa University, Ishikawa 920-1192, Japan*

[*]Corresponding author: hadishafaii@yahoo.com
Tel: +61, 484637418; Fax: +61, 2 98508943

ABSTRACT

How new subduction zones form is an ongoing scientific question with key implications for our understanding of how this process influences the behavior of the overriding plate. Here we focus on the effects of a Late Cretaceous subduction-initiation (SI) event in Iran and show how SI caused enough extension to open a back-arc basin in NE Iran. The Late Cretaceous Torbat-e-Heydarieh ophiolite (THO) is well exposed as part of the Sabzevar-Torbat-e-Heydarieh ophiolite belt. It is dominated by mantle peridotite, with a thin crustal sequence. The THO mantle sequence consists of harzburgite, clinopyroxene-harzburgite, plagioclase lherzolite, impregnated lherzolite and dunite. Spinel in THO mantle peridotites show variable Cr# (10-63), similar to both abyssal and fore-arc peridotites. The igneous rocks (gabbros and dikes intruding mantle peridotite, pillowed and massive lavas, amphibole gabbros, plagiogranites and associated diorites and diabase dikes) display rare earth element patterns similar to MORB, arc tholeiite and back-arc basin basalt. Zircons from six samples, including plagiogranites and dikes within mantle peridotite, yield U-Pb ages of *ca* 99-92 Ma, indicating that the THO formed during the Late Cretaceous and was magmatically active for ~7 Myr. THO igneous rocks have variable εNd(t) of +5.7 to +8.2 and εHf(t) ranging from +14.9 to +21.5; zircons have εHf(t) of +8.1 to +18.5. These isotopic compositions indicate that the THO rocks were derived from an isotopically depleted mantle source similar to that of the Indian Ocean, which was slightly affected by the recycling of subducted sediments. We conclude that the THO and other Sabzevar-Torbat-e-Heydarieh ophiolites formed in a back-arc basin well to the north of the Late Cretaceous fore-arc, now represented by the Zagros ophiolites, testifying that a broad region of Iran was affected by upper-plate

extension accompanying Late Cretaceous subduction initiation.

KEYWORDS: Hf-Nd isotopes, U-Pb geochronology, back-arc basin, ophiolite, Iran.

INTRODUCTION

Ophiolites are fragments of upper mantle and oceanic crust (Coleman, 1977; Nicolas, 1989) and are often tectonically incorporated into continental margins during continent-continent and arc-continent collisions (Dilek and Flower, 2003), ridge-trench interactions (Lagabrielle et al., 2000), and/or subduction-accretion events (Cawood, 1989). Ophiolites and their dismembered equivalents are especially common in suture zones in both collisional and accretionary orogens of Neoproterozoic and Phanerozoic age (e.g., (Furnes et al., 2014; Hébert et al., 2012; Saccani et al., 2013). (Dilek and Furnes, 2011) classified ophiolites into continental margin-, mid-ocean-ridge (MOR)-, plume-, supra-subduction zone-, volcanic arc- and accretionary- types according to their tectonic settings. Evidence is growing that many ophiolites form during subduction initiation in a fore-arc setting (Whattam and Stern, 2011), and this concept is useful for understanding the Late Cretaceous ophiolites of the Zagros mountains in Iran (Moghadam and Stern, 2011; Moghadam et al., 2010).

The emplacement of an ophiolite on continental crust can occur via various mechanisms, including obduction, subduction and then exhumation of oceanic lithosphere or even through trapping and compression of oceanic basins between two neighboring continental blocks, as is the case for NE Iran ophiolites. Despite the fact that it is geodynamically difficult to emplace ophiolites that form anywhere other than the

fore-arc (Stern, 2002), ophiolites are known to form in other extensional settings such as marginal basins or back-arc basins. Back-arc basins need strong extension to open and this can be achieved as a result of subduction initiation (SI). Back arc extension is not as easily accomplished if regional compression causes induced SI but is expected to accompany spontaneous SI, due to the large lateral density contrasts across the lithospheric weakness separating the pertinent plates (Stern, 2004; Stern and Gerya, 2017). Spontaneous SI, (i.e., when oceanic lithosphere begins to sink vertically before down-dip motion is established), will cause extension in the overlying plate, and this can open a back-arc basin. How subduction initiation causes extension in the overlying plate also depends on plate configuration and relative motions, thickness of the subducting oceanic slab, and whether SI is spontaneous or induced.

Marginal basin is a general term for basins of unknown origin associated with continental margins and island arcs. Back-arc basins are a type of marginal basin that open at a convergent plate margin behind an active magmatic arc. Most back-arc basins are associated with oceanic arcs, although rifting of continental lithosphere also produces back-arc basins (i.e. ensialic back-arc basins) (Gerya, 2011; Stern, 2002). Back-arc ophiolites are represented by MORB-like, BABB-like and calc-alkaline type intrusions and lavas, generated by partial melting of a MORB-type mantle source (through mantle wedge flow; e.g., (Long and Wirth, 2013)) into the sub-arc mantle wedge (Saccani et al., 2008). In many cases, the tectonic setting of ophiolites is obscured by alteration and deformation, so that workers rely heavily on relict mineralogy and immobile trace element geochemistry to resolve the original tectonic setting. This approach is problematic because BAB and fore-arc ophiolites share many geochemical and

111 petrographic features and can be difficult to distinguish solely on a basis of petrology and
112 geochemistry; other considerations are required to distinguish back-arc and fore-arc
113 ophiolites. This report addresses this problem by focusing on a well-preserved ophiolite
114 belt in NE Iran that clearly formed in a back-arc basin distal to coeval ophiolites that
115 formed in a fore-arc, subduction-initiation (SI) setting. Our research supports results from
116 recent IODP drilling in the Philippine Sea indicating that extensional magmatism related
117 to subduction initiation can affect much larger regions than just the immediate fore-arc
118 environment (Hickey-Vargas et al., 2018).

119 The Sabzevar-Torbat-e-Heydarieh ophiolites (= STHO) are excellent examples of
120 Late Cretaceous ophiolites of Iran. The STHO is exposed over a large area of NE Iran,
121 approximately 130 x 400 km (Fig. 1). From a regional-tectonic perspective, the STHO is
122 situated in a back-arc setting, separated by ~600km from the Zagros fore-arc ophiolites
123 (Moghadam and Stern, 2011; Monsef et al., 2018), the Urumieh-Dokhtar Magmatic Belt
124 (UDMB) and continental crust of the Lut block (Fig. 2). The faulted contact between the
125 southernmost STHO ophiolites and Ediacaran-Cambrian (Cadomian) basement to the
126 south is exposed on the southern margin of the STHO (Fig. 3). Cadomian basement
127 comprises granitoids, gabbros, rhyolites and pyroclastic rocks with ages of 531-553 Ma
128 (Moghadam et al., 2017b). There is no suture to which STHO ophiolites are clearly
129 related, which probably were exhumed during latest Cretaceous-Paleogene formation of
130 the Oryan Basin (Fig. 3). This is also confirmed by low-temperature thermo-
131 chronometric and structural evidence, which show that uplift of the ophiolite domain was
132 accompanied by dextral transpression beginning in early Paleocene (~60 Ma) and ended
133 in the Miocene-Pliocene (5 Ma) (Tadayon et al., 2018). This conclusion is supported by

134 the presence of an early Paleocene unconformity and deposition of middle Paleocene
135 conglomerates which seal the STHO ophiolites. These conglomerates were produced by
136 the erosion of the exhuming ophiolites during dextral transpression (Tadayon et al.,
137 2018).

138 The modern episode of subduction of the Zagros orogen subducted Neotethys and
139 began at 104-98 Ma, as determined by zircon U-Pb dating of Zagros fore-arc ophiolites
140 (Moghadam et al., 2013; Moghadam and Stern, 2015). Late Cretaceous subduction
141 initiation was accompanied by a major change in the direction and velocity of Arabia-
142 Eurasia convergence (Agard et al., 2007). We suggest that Late Cretaceous spontaneous
143 SI caused the observed change in plate motion; that subsidence of Mesozoic Neotethys
144 lithosphere commenced along a transform margin adjacent to buoyant Eurasian
145 lithosphere, causing proto-forearc seafloor spreading and producing the Zagros ophiolites
146 (Moghadam and Stern, 2011; Moghadam et al., 2010). Foundering Neotethys oceanic
147 lithosphere induced extension on the southern margin of Eurasia, producing back-arc
148 basins, tilting of crustal blocks, uplift and intense erosion of the Iranian plateau, as well
149 as core complex exhumation in some parts of the Iranian plateau (Malekpour-Alamdari et
150 al., 2017; Moritz et al., 2006; Verdel et al., 2007). For testing the Late Cretaceous SI
151 model for southern Eurasia, it is essential to understand the significance of the Late
152 Cretaceous back-arc basins in NE Iran, of which the Sabzevar-Oryan-Cheshmehshir-
153 Torbat-e-Heydarieh ophiolite is the largest representative (Fig. 3). Besides the suspected
154 back-arc basins in NE Iran, there are several other Late Cretaceous oceanic basins
155 (ophiolites) whose opening seems to be related to the Late Cretaceous extension within
156 the Iranian plateau caused by SI along the Zagros suture zone. These ophiolites include

the Khoy ophiolite in NW Iran (e.g, (Khalatbari-Jafari et al., 2004)) and scattered ophiolitic slices along the Talysh-Qare Dagh mountains in NNW Iran (e.g., (Burtman, 1994; Omidvar et al., 2018)).

We present here the results of our study of Late Cretaceous mantle peridotites, gabbros, lavas and plagiogranites from the Torbat-e-Heydarieh ophiolite. We provide zircon U-Pb ages for six samples of geochemically-distinct plagiogranites, gabbros and dikes, and compare these with geochronological data from the Sabzevar ophiolite to the NW (Fig. 3). Peridotite mineral compositions as well as major, trace and rare-earth element data and bulk rock Nd-Hf and zircon Hf isotopes for selected samples are used to constrain the tectonic setting of the different magmatic suites. We show that the mantle rocks and magmatic rocks were generated during back-arc basin extension and use these results and their magmatic-stratigraphic associations suggest that magmatism occurred in response to SW-directed rollback of a NE-dipping subduction zone during SI (Fig. 2).

GEOLOGICAL SETTING

The STHO is bordered to the north by the major Sangbast-Shandiz strike-slip fault delimiting the Binalud Mountains (Fig. 1). To the south, the STHO is bounded by the major Great Kavir-Dorouneh sinistral strike-slip fault (Figs. 1 & 3). The STHO comprises four main regions where ophiolites crop out (Fig. 3), separated by the Paleocene-Eocene Oryan sedimentary basin: (1) NNW of Sabzevar (the Sabzevar ophiolite, studied by (Moghadam et al., 2014b; Moghadam et al., 2015; Nasrabady et al., 2011; Omrani et al., 2013; Rossetti et al., 2014; Rossetti et al., 2010; Shojaat et al., 2003)); (2) SSW of Sabzevar (Oryan ophiolite, no published data); (3) Cheshmehshir in

the far south (Maghfouri et al., 2016), and (4) north of Torbat-e-Heydarieh, the focus of this study.

The STHO lies between the Lut block in the south and the Kopeh-Dagh (Turan platform (Thomas et al., 1999) in the north. The STHO formed during the Late Cretaceous (Moghadam and Stern, 2015) and contains a well-preserved mantle sequence, but some parts are fragmented and sheared. There is consensus that the STHO formed above a subduction zone (-SSZ) setting, as most Sabzevar ophiolite lavas show appropriate geochemical signatures (Ghazi et al., 1997; Moghadam et al., 2014a; Shojaat et al., 2003). Sabzevar mantle peridotites have spinels with both MORB-like (Cr#<50%) and SSZ-type (Cr#>50%) signatures but most peridotite spinels have high Cr# (>50) with low TiO_2 and resemble those of SSZ peridotites (Moghadam et al., 2014a). Some Sabzevar ophiolite pillow lavas have OIB-like whole-rock compositions, suggesting a plume or subcontinental lithospheric mantle source. The Sabzevar ophiolite is covered by Late Campanian to Early Maastrichtian (~75-68 Ma) pelagic sediments. Sabzevar plagiogranites yield zircon U-Pb ages of 99.9-77.8 Ma (Moghadam et al., 2014a). Magmatic rocks of the Sabzevar ophiolite have positive εNd (t) values (+5.4 to +8.3) and most have high $^{207}Pb/^{204}Pb$, indicating a significant contribution of subducted sediments to their mantle source (Moghadam et al., 2014a).

The Torbat-e-Heydarieh ophiolite (THO) constitutes the southeasternmost of the four STHO outcrops, covering an area 60 km long and 50 km wide (Fig. 4). The THO shows no contact with older rocks and is unconformably overlain by Paleocene-Eocene conglomerates and sandstones. The THO is mostly composed of mantle peridotites including lherzolites, impregnated lherzolites, minor harzburgites and discordant dunites

and chromitite lenses (Figs. 5, 6A). Harzburgites with 2-3 modal% clinopyroxene and plagioclase-lherzolites are also common. Dunites also occur as small veins and pods/lenses within the harzburgite. Diabasic-gabbroic-pyroxenitic dikes crosscut the mantle sequence and in most cases are boudinaged (Fig. 5). Diabasic-gabbroic dikes are locally converted into rodingite (Fig. 6B). Some diabasic dikes are metamorphosed to greenschist or lower amphibolite facies. Small intrusions of cumulate and fine-grained isotropic gabbro and pyroxenite (Figs. 6C, D) are common in harzburgites and lherzolites; pyroxene-rich gabbroic dikes are also common within these gabbros. Cumulate gabbroic lenses occasionally are layered, characterized by plagioclase-rich (anorthosite) and Opx- and Cpx-rich (olivine-beearing) bands (olivine-bearing melanocratic gabbros) (Fig. 6D). The gabbroic sequence is crosscut by diabasic and microgabbroic to more-evolved plagiogranitic dikes or small pockets (Fig. 6E). Some dikes within the gabbros also intrude the underlying peridotites. In some cases, angular gabbroic xenoliths are found within the plagiogranitic pockets (agmatite, Fig. 6F). Late plagiogranitic dikes were injected into both gabbros and underlying peridotites.

The THO crustal sequence is more poorly exposed than the mantle section but includes massive and pillow lavas (Fig. 6G), isotropic and coarse-grained massive gabbros and plagiogranite lenses/dikes within the gabbros (Fig. 5). The contact between the mantle sequence and crustal rocks in most cases is tectonized, but in some cases the mantle rocks are overlain by cumulate gabbros or by crustal lavas and pelagic limestones. The presence of pelagic limestone on top of the mantle section suggests that Late Cretaceous extension on the seafloor was locally amagmatic. Crustal gabbros differ from mantle gabbros by containing more diabasic dikes and large plagiogranitic lenses, but

plagiogranitic dikes are also common. Lava flows are slightly metamorphosed to greenschist or lower amphibolite facies. Other rocks from both crustal and mantle sequences show no trace of metamorphism, but instead they show slight to moderate alteration. High-temperature alteration of mantle dikes into rodingite is also common. Pillow lavas show pyrite-chalcopyrite mineralization. Massive and pillow lavas are occasionally tectonically interlayered with peridotites. There is no obvious geochemical difference between most pillow and massive lavas (see next section). Late Cretaceous (Cenomanian to Turonian, ~ 99-90 Ma) pelagic sediments and pyroclastic rocks are interlayered with and conformably cover the lavas (Figs. 6H, I). Cold breccia including basaltic fragments set in a pelagic limestone matrix is abundant. THO melanges include serpentinites, lavas and pelagic sediments. These melanges are especially abundant in the Sabzevar ophiolites, where various ophiolitic units, Paleocene-Eocene magmatic rocks and shallow-water limestones are dispersed with serpentinites, showing that these melanges are related to Eocene or younger deformation (Moghadam et al., 2014a).

PETROGRAPHY

Lherzolites are the predominant THO mantle rocks; they contain serpentinized olivine, orthopyroxene and large clinopyroxenes (Fig. 7A). Nearly all lherzolite samples are moderately (20-30%) serpentinized. Vermicular brown spinel is abundant and generally intergrown with clinopyroxene. Harzburgites are minor and contain serpentinized olivine and orthopyroxene porphyroclasts with fine-grained clinopyroxene (2-3 %, Fig. 7C) and deep brown spinel. Serpentinization of harzburgites (50-60%) is greater than in lherzolites (20-30 %). The content of clinopyroxene is higher in Cpx-

harzburgites (3-5 %). Here, fine clinopyroxenes occur in embayments of orthopyroxene porphyroclasts (Fig. 7B), associated with vermicular spinels (Fig. 8A). Part of the THO mantle section was impregnated with a percolating basaltic melt which filtered through peridotites, crystallizing plagioclase and clinopyroxene. Impregnated lherzolites have more coarse-grained clinopyroxene aggregates and lighter-brown spinel compared to normal lherzolites (Fig. 7C). Plagioclase lherzolites show traces of altered plagioclase (5-7 modal %) along with melt-impregnated clinopyroxenes (up to 20-30 %) and light brown vermicular spinel. Large clinopyroxenes enclose plagioclase and brown spinels (Figs. 6D and 7B). Plagioclase also occurs at the contact of orthopyroxene with impregnated clinopyroxenes (Fig. 8C). Blebs of sulfide minerals are also observed. Clinopyroxene accumulation in plagioclase lherzolites makes these rocks similar to olivine websterites (Fig. 9A). Plagioclase lherzolites show melt-assisted crystallization of new olivine grains in plagioclase and clinopyroxene embayments (Fig. 8C). Dunites are altered (50-70 % serpentinization) with mesh-textured olivines (>90%) and coarse-grained black spinel. Spinels contain abundant inclusions of serpentinized olivine, clinopyroxene and amphibole (Fig. 8D). Amphibole inclusions are altered to chlorite.

Gabbroic lenses within peridotites vary from gabbro (~1-2 % Opx) to gabbronorite (10-30 % Opx, Fig. 9B). Cumulate gabbros are heterogeneous, with dark bands rich in clinopyroxene, orthopyroxene and minor plagioclase and whitish bands rich in plagioclase with minor clinopyroxene. Olivine is rare, whereas coarse-grained, subhedral orthopyroxene and anhedral clinopyroxene are the main components of cumulate gabbros (Fig. 7E, F). Plagioclase is interstitial between pyroxene crystals (Fig. 8E, F). Fine-grained, isotropic gabbros containing plagioclase, orthopyroxene and clinopyroxene are

also common in the mantle sequence, closely associated with cumulate gabbros. Occasional primary brown amphiboles also occur as interstitial laths between other minerals. Rodingitized dikes contain fine-grained hydrogrossular, rare diopside and wollastonite as well as pectolite.

Coarse-grained crustal plutonic rocks contain plagioclase and amphibole in diorites and clinopyroxene and plagioclase in gabbros. Some gabbros contain interstitial amphibole. Plagiogranites have granular texture and are dominated by plagioclase, quartz and amphibole with secondary epidote, chlorite, sericite, iron oxide and titanite. Apatite and zircon are minor components. Plagiogranites can be petrographically divided into tonalites and diorites with more amphibole. Granophyric intergrowths of plagioclase and quartz are also common in these rocks.

Diabasic dikes are fine-grained and contain magnesio-hornblende and sodic plagioclase. Pillow lavas contain clinopyroxene microphenocrysts, plagioclase microlites and palagonitized glass. Fine-grained clinopyroxene is also common in the groundmass. Calcite, chalcedony, titanite, sericite, epidote, prehnite and chlorite are secondary phases.

Pillow lavas display hyaloporphyritic to intersertal texture with clinopyroxene and plagioclase micro-phenocrysts. Massive lavas are similar to pillow lavas but are less altered. The glassy groundmass of some massive lavas is altered into chlorite and clay, but most are holocrystalline without glass.

ANALYTICAL METHODS

We used six main analytical procedures to study THO rocks: 1) JEOL wavelength dispersive electron probe X-ray micro-analyzer (JXA 8800R) to determine the composition of minerals; 2) Inductively Coupled Plasma-Atomic Emission (ICP-AES) and Inductively Coupled Plasma-Mass Spectrometry (ICP-MS) to determine whole-rock contents of major- and trace elements; 3) Cathodoluminescence (CL) imaging of zircons; 4) Sensitive High Resolution Ion Microprobe (SHRIMP) analyses to determine zircon U-Pb ages; 5) Laser Ablation Inductively Coupled Plasma-Mass Spectrometry (LA-ICPMS) analyses to determine zircon U-Pb ages and to analyze the trace-element compositions of clinopyroxene and orthopyroxene from mantle peridotites and gabbros; 6) Multi Collector-Inductively Coupled Plasma-Mass Spectrometry (MC-ICPMS) equipped with LA for *in situ* analysis of zircon Hf isotopic compositions. The same MC-ICPMS was used to analyze the isotopic compositions of Nd and Hf in whole-rock samples.

We studied ~100 samples for petrography, 13 polished thin sections for electron microprobe analysis, 39 for whole-rock major- and trace-element compositions, 6 for U-Pb zircon ages, 8 for whole-rock Nd and Hf analyses, 6 for *in situ* mineral trace elements and 6 for *in situ* Lu-Hf isotope analyses of zircons. The Nd and Hf isotopic compositions discussed below are corrected for 100 Ma of radiogenic ingrowth. The details of each technique are given in Electronic Appendix A.

WHOLE ROCK GEOCHEMISTRY

Three mantle peridotites, fourteen mantle gabbros, ten pillowed and massive lavas, four amphibole gabbros, two mantle-intruding dikes, and six plagiogranites and associated diorites and diabase dikes samples were selected for whole rock analysis.

Sample locations are shown on Fig. 4. The analyzed samples are characterized by variable loss on ignition; 0.6-4.2 wt % for crustal rocks, 5.9-11.7 wt % for peridotites and 0.6-5.8 wt % for mantle gabbros. Because of the mobility of some major- and trace elements during alteration, emphasis is placed on immobile trace elements such as the REE and high field strength elements (HFSE) to evaluate the original composition and tectono-magmatic setting of Torbat-e-Heydarieh magmatic rocks. Fluid-mobile elements such as Cs, Rb, U, Pb, and Sr may be discussed but are generally de-emphasized in the following sections. Similarly, to avoid the effects of alteration and seawater exchange on isotopic composition of the rocks, alteration-resistant Nd and Hf isotopes are reported.

Mantle Units

Harzburgite has low contents of CaO and Al_2O_3 (~1.6 wt %), whereas Cpx-harzburgite and plagioclase lherzolite contain more CaO (~2.3 and ~8.9 wt % respectively) and Al_2O_3 (~2.3 and ~5.1 wt % respectively) (Supplementary Table 1). Harzburgites show highly depleted REE patterns, with steep slopes from LREEs to MREEs (Fig. 10A). REE abundances are higher in Cpx-harzburgite and plagioclase lherzolite with nearly flat patterns from MREEs to HREEs, but with steep slope from LREEs to MREEs. These patterns are similar to those of the cumulate gabbros (Fig. 10A). Enrichment in MREEs to HREEs for Cpx-harzburgite and plagioclase lherzolite is consistent with the formation of Cpx by metasomatism. Enrichment in fluid-mobile elements such as U, Rb, Ba, Sr, and Pb relative to LREEs is characteristic of THO mantle peridotites.

Mantle gabbroic rocks have variable contents of SiO_2 (~45-54 wt %), Al_2O_3 (~10-22

wt %), MgO (~4-16 wt %), and CaO (~10-20 wt %), reflecting different extents of fractionation and/or modal contents of olivine, orthopyroxene, clinopyroxene, and plagioclase. Gabbroic rocks are Ti-poor, with ~0.06-0.9 wt % TiO_2; a microgabbro dike within the gabbro cumulate contains more TiO_2 (0.9 wt %). Isotropic gabbros show an IAT signature in the Ti *vs* V diagram (Shervais, 1982) (Fig. 11B). Gabbroic rocks show three distinct patterns of rare earths and other trace elements (Fig. 10A and B). Cumulate gabbros have low REE concentrations compared to fine-grained isotropic gabbros and the microgabbro dike. Cumulate gabbros are highly depleted in LREE ($La_{(n)}/Yb_{(n)}$ = 0.04-0.23) but with nearly flat REE patterns from HREE to MREE ($Gd_{(n)}/Yb_{(n)}$ = 0.7-1.2). Eu enrichment is also noticeable. Extreme depletion in Nb, Ta and Zr (e.g., $Nb_{(n)}/La_{(n)}$ = 0.05-0.2) and enrichment in U, Pb, Ba and Sr (e.g., $Sr_{(n)}/La_{(n)}$ = 93-338) relative to LREE is characteristic of these rocks (Fig. 10B).

Isotropic gabbros are enriched in bulk REE compared to the cumulate gabbros and show LREE-depletion to almost flat patterns ($La_{(n)}/Yb_{(n)}$ = 0.3-0.7). These rocks are slightly depleted in Nb and Zr (e.g., $Nb_{(n)}/La_{(n)}$ = 0.3-0.9) and enriched in Sr, Th, and U (Fig. 10B). The microgabbro dike shows a flat REE pattern ($La_{(n)}/Yb_{(n)}$ = 1.2), weak negative anomalies in Nb-Ta and enrichment in Sr, Th, U, Ba and Rb.

Crustal rocks

The Torbat-e-Heydarieh massive lavas have similar contents of SiO_2 (~47-49 wt%) and TiO_2 (1.1-1.6 wt %) and Mg# ($100Mg/Mg+Fe^{+2}$) (54-63) (Supplementary Table 4). Pillow lavas show greater variability, ranging from 49-55 wt % SiO_2, Mg# values of 33-60, and TiO_2 contents of 0.4-2.4 wt %. These volcanic rocks exhibit both tholeiitic and

calc-alkaline tendencies in the FeO^t/MgO *vs* SiO_2 diagram (Miyashiro, 1974) (Fig. 11A). In a Ti *vs* V diagram (Shervais, 1982), THO volcanic rocks tend to plot in both the island-arc tholeiitic (IAT) and MORB fields. Sample TH11-39 shows affinity to E-MORB-type lavas (Fig. 11B).

Massive lavas are depleted in LREE relative to HREE ($La_{(n)}/Yb_{(n)}$=0.5-0.8) and have a slight to moderate depletion in Nb ($Nb_{(n)}/La_{(n)}$=0.4-0.7). They are not enriched in Ba, Th and U ($Th_{(n)}/La_{(n)}$=0.7-1) relative to N-MORB (Figs. 10 C and D). These characteristics are similar to back-arc basin basalts or early arc tholeiites (Peate and Pearce, 1998). These lavas differ from Sabzevar calc-alkaline lavas, which are enriched in LREE, Th, U and extremely depleted in Nb (Moghadam et al., 2014a).

Pillow lavas can show both enrichment and depletion in LREE relative to HREE ($La_{(n)}/Yb_{(n)}$~0.6-2.7) as well as variable Nb-Ta depletion and Th enrichment (e.g., $Nb_{(n)}/La_{(n)}$=0.3-0.8 and $Th_{(n)}/La_{(n)}$=1.2-4.3) relative to N-MORB (Fig. 10 C and D). They are geochemically similar to E-MORB and depleted tholeiitic lavas. There is no clear relationship between these two types of pillow lavas in the field.

Plagiogranites and their host rocks

Plagiogranites and their host rocks (diorites and diabasic dikes) have variable SiO_2 (71-79 wt % for plagiogranites and 56-58 wt % SiO_2 for host rocks) and TiO_2 (0.2-0.5 wt %) contents (Supplementary Table 4). Plagiogranites and their host rocks have LREE-enriched and flat REE patterns respectively ($La_{(n)}/Yb_{(n)}$=0.8-3.7) with depleted Nb and Ta contents ($Nb_{(n)}/La_{(n)}$=0.3-0.9) accompanied by Ba, U, K, and Th enrichment ($Th_{(n)}/La_{(n)}$~2-9) relative to N-MORB (Fig. 10F). Plagiogranites also show strong positive anomalies in Sr and sometimes in Eu. These geochemical features are similar to Sabzevar

plagiogranites (Moghadam et al., 2014a) and felsic igneous rocks of convergent plate margins (Pearce et al., 1984). These geochemical signatures are also similar to the geochemical characteristics of plagiogranites from other Tethyan ophiolites of the eastern Mediterranean realm (e.g., (Anenburg et al., 2015; Bonev and Stampfli, 2009; Dilek and Thy, 2006; Osozawa et al., 2012; Uner et al., 2014).

Mantle dikes

Diabasic and dioritic dikes injected into mantle peridotites have SiO_2~50-57 wt %, with Mg# ranging between 43 and 82 (Supplementary Table 4). Their TiO_2 contents are low, ranging from 0.1-1.2 wt %. In the FeO^t/MgO *vs* SiO_2 diagram, the dikes are broadly calc-alkaline, excluding sample TH11-19 (Fig. 11A). In a Ti *vs* V diagram (Shervais, 1982), these rocks plot in the IAT field (Fig. 11B). Diabasic dikes are characterized by flat REE patterns ($La_{(n)}/Yb_{(n)}$=1.1-1.8), depletions in Nb and Ta ($Nb_{(n)}/La_{(n)}$=0.3-0.5) and Ba, U, Sr, and Th enrichment ($Th_{(n)}/La_{(n)}$=2.6-3.2), resembling island arc tholeiites (IAT). Amphibole gabbros are characterized by an IAT signature in the Ti *vs* V diagram (Fig. 11B). They show LREE-enriched concave-upward patterns ($La_{(n)}/Yb_{(n)}$~2-10) and depletion in Nb and Ta ($Nb_{(n)}/La_{(n)}$~0.4-0.6).

MINERAL COMPOSITION

Major element compositions of the main rock-forming minerals were determined in mantle peridotites and cumulate gabbroic rocks: olivine, spinel, orthopyroxene, clinopyroxene, plagioclase and amphibole. Trace element contents of clinopyroxenes are also presented. These results are discussed below.

Olivine

Olivine in dunite has forsterite contents ranging from 92.8% to 93.1% ($Fo_{92.8-93.1}$) with high NiO content (~0.3-0.4 wt %) (Supplementary Table 1), typical for mantle olivine. Olivine in the harzburgites and Cpx-harzburgites is slightly less magnesian (but still mantle-like) with Mg# and NiO between 91.4-91.9 ($Fo_{91.4-91.9}$) and 0.34-0.43 wt % respectively. Lherzolites and impregnated lherzolites are characterized by olivine Mg# and NiO content of 89.5-91.3 ($Fo_{89.5-91.3}$) and 0.34-0.52 wt% respectively, also mantle-like. Olivine in plagioclase lherzolites has lower Fo and NiO contents ($Fo_{84.8-85.6}$ and 0.18-0.24 wt %) than commonly are found in mantle peridotite. These olivines have a magmatic composition (compared to high Mg# mantle olivines) and are interpreted to have crystallized from impregnating mafic melts.

Spinel

Peridotite spinels show variable Cr# (100Cr/(Cr+Al); 10-63), similar to those in abyssal, back-arc basin, and fore-arc peridotites (Dick and Bullen, 1984) (Fig. 12). Spinel from dunites has higher Cr# (59-63) and TiO_2 contents (0.18-0.25 wt %) and follows the peridotite-boninitic melt interaction trend of (Pearce et al., 2000a) (Figs. 12A and B). Spinels from harzburgites and Cpx-harzburgites have variable contents of TiO_2 (0.03-0.07 wt % in harzburgites and 0.1 to ~0.3 in Cpx-harzburgites) and FeO (~12.2-12.8 wt % in harzburgites and 14.2-15.5 wt % in Cpx-harzburgites). Harzburgite spinels have lower Cr# (22-24) than Cpx-harzburgite spinels (24-36).

Spinels of lherzolites and impregnated lherzolites have variable contents of TiO_2 (0.02-0.12 wt %) and Cr# (10-20). Spinel compositions of lherzolites and impregnated lherzolites overlap at low Cr#. This is because these two rocks have same mineral

assemblages; impregnated lherzolites have more coarse-grained clinopyroxene aggregates with the lightest brown spinels. The Cr# of their spinels is similar to that of abyssal peridotites (Dick and Bullen, 1984). Spinels from plagioclase lherzolites have high TiO_2 (0.15-0.25 wt%) and FeO (~31-39 wt%) content and high Cr# (41-48).

Orthopyroxene

Orthopyroxene in harzburgite and Cpx-harzburgite has Mg# (91-92) and elevated contents of Al_2O_3 (2.7-5 wt %) and Cr_2O_3 (0.56-1 wt %) (Supplementary Table 1). Orthopyroxene in lherzolites and impregnated lherzolites has constant Mg# (89-91) but variable Al_2O_3 (~3-6.1 wt %) content. Plagioclase-lherzolite orthopyroxenes have low Mg# (86) and Al_2O_3 (2.1-2.3 wt %) compared to orthopyroxene from other THO peridotites. Orthopyroxene in gabbros has lower Mg# (79-84) and Al_2O_3 contents (1.5-2.1 wt %). The Al_2O_3 content of the THO peridotite orthopyroxenes are relatively high, ranging from 1.5-6.1 wt %; the higher values are encountered in impregnated lherzolites. However, the Al_2O_3 content of orthopyroxene from fertile spinel peridotites from ophiolites in other worldwide localities (e.g., the Vardar ophiolite, (Bazylev et al., 2009) and fertile peridotites from the Yarlung Zangbo suture zone, (Bedard et al., 2009)) and oceanic back-arcs (e.g., Mariana Trough, (Ohara et al., 2002) and South Sandwich arc-basin, (Pearce et al., 2000b)) are also high, resembling the THO impregnated lherzolites, and show the fertile nature of the host mantle rocks.

Clinopyroxene

Clinopyroxene is abundant in dunite as inclusions in large chromites. Its composition is $Wo_{49-51}En_{47-49}Fs_{2-3}$. It has high Mg# (94-97) and low TiO_2 (0.06-0.19 wt. %) and Al_2O_3

(0.6-~2 wt. %). Harzburgites and Cpx-harzburgites contain clinopyroxene with $Wo_{44-52}En_{48-49}Fs_{3-4}$. Clinopyroxene in Cpx-harzburgites have higher TiO_2 (0.26-0.35 wt. %), but lower Al_2O_3 (3.9-4.6 wt. %) compared to those in harzburgites (TiO_2=0.12-0.17 wt. %; Al_2O_3=3-5.2 wt. %) (Fig. 12C) with identical Mg# (92-94). Clinopyroxene in mantle lherzolites and impregnated lherzolites has variable composition ($Wo_{36-51}En_{45-59}Fs_{4-6}$) with high Mg# (91-93), Al_2O_3 (4.9-7.1 wt %) and TiO_2 (0.3-0.5 wt %) (Supplementary Table 1). Plagioclase lherzolites have clinopyroxene with more constant composition ($Wo_{41-48}En_{46-52}Fs_{6-7}$) but with low TiO_2 (0.06-0.16 wt %) and Al_2O_3 (2.2-3.8 wt %) and lower Mg# (87-89) compared to clinopyroxene from other THO lherzolites. On a TiO_2 *vs* Mg# diagram (Fig. 12C) clinopyroxenes from THO peridotites are similar to those found in both abyssal and supra-subduction zone peridotites. Clinopyroxene and spinel from nearly all mantle units of Tethyan ophiolites show both abyssal and supra-subduction-zone geochemical signatures (e.g., (Aldanmaz, 2012; Ghazi et al., 2010; Monsef et al., 2010)). This geochemical duality can be also observed in the crustal lavas of Neotethyan ophiolites (e.g., (Dilek and Furnes, 2009; Dilek et al., 2007; Sarifakioglu et al., 2009)).

Clinopyroxene in gabbro has variable composition ($Wo_{37-47}En_{45-51}Fs_{7-13}$). The more evolved compositions (with low Ca but high Fe) are found in smaller crystals between large clinopyroxenes. Gabbroic clinopyroxenes have TiO_2 and Al_2O_3 contents from 0.07-0.21 and 1.7-2.8 wt % respectively; these are lower than in Sabzevar gabbroic clinopyroxenes.

Plagioclase

Plagioclase in plagioclase lherzolites is highly altered; unaltered portions show very high An contents (96.2-98.3%). Gabbro plagioclase is also anorthite-rich (~An 91.1-98.2)

(Supplementary Table 1); amphibole-bearing gabbros with less orthopyroxene contain An_{91-92} plagioclase. Comparison of the clinopyroxene Mg# against anorthite content in plagioclase (Sanfilippo et al., 2013), shows a pattern similar to SSZ-type gabbros (Fig. 12D).

Amphibole

Analyses of amphibole inclusions within dunite chromites, plotted in the Mg# *vs* Si diagram (*not shown*), show that these are pargasite to edenite according to (Leake et al., 1997). The Cr_2O_3 contents of these amphiboles are high (2.4-3.1 wt. %).

Clinopyroxene: Trace Element Geochemistry

Trace-element abundances (including REEs) in THO lherzolites, impregnated lherzolites, plagioclase lherzolites and cumulate gabbros are listed in Supplementary Table 2.

All mantle clinopyroxenes from the Torbat-e-Heydarieh ophiolite are enriched in REEs with LREE-depleted patterns. They are similar to REE abundances in Cpx from mid-ocean ridge (MOR) cumulates and abyssal peridotites and are much more enriched that those in SSZ peridotites (Fig. 13A, C).

Chondrite-normalized REE patterns of clinopyroxenes from THO lherzolites are strongly depleted in light REEs (LREE) but are flat in middle to heavy REEs (MREE-HREE). These patterns are similar to those of Cpx in oceanic abyssal peridotites (Bizimis et al., 2000; Johnson et al., 1990), although total REE concentrations are greater (Fig. 11A). The REE content of THO lherzolite Cpx is even higher than Cpx from Sabzevar plagioclase lherzolites (Fig. 13B) (Shafaii Moghadam et al., 2015). Clinopyroxene trace-

element patterns are depleted in Ti and Zr, but not in Sr and Eu (Fig. 13B). Clinopyroxene in THO impregnated lherzolites exhibits REE patterns similar to Cpx from THO lherzolites, characterized by higher total REE contents compared to Cpx from abyssal peridotites and Sabzevar lherzolites (Fig. 13C). Negative anomalies in Ti and Zr are also obvious (Fig. 13D).

Cpx in THO plagioclase lherzolites have REE patterns similar to those of Cpx from MOR cumulates (Ross and Elthon, 1993), but with more depleted LREE (La-Sm, Fig. 13C). These patterns are also similar to those for Cpx from Sabzevar Cpx-harzburgites. MREE-HREE abundances in Cpx of plagioclase lherzolite ar depleted compared to Cpx from THO lherzolites and impregnated lherzolites (Fig. 13C). Slight depletion in Ti and strong Zr negative anomalies are conspicuous in plagioclase lherzolites (Fig. 13D).

The REE abundances and patterns of clinopyroxenes in THO gabbro cumulates are in the range of those exhibited by MOR cumulates (Ross and Elthon, 1993) (Fig. 13A), but with more convex-upward MREEs with Sm-Ho peaks. They are similar to clinopyroxene patterns from Sabzevar cumulate gabbros but with lower REE abundances (Fig. 13A). The Cpx from cumulate gabbros are depleted in Zr and Ti but enriched in Sr (Fig. 13B). Trace element patterns of Cpx in cumulate gabbros are between those from Cpx of plagioclase and impregnated lherzolites.

Nd-Hf Isotopes

Eight samples were selected including depleted tholeiitic pillow lavas, back-arc basin-type massive lavas, supra-subduction zone-type plagiogranites, IAT-like diabasic dike and back-arc to fore-arc-type gabbros for analysis of whole-rock Nd and Hf

518 isotopes. Hf-Nd isotope compositions are useful for inferring mantle source
519 characteristics and the role of sediments and older continental crust in generating
520 subduction-related magmas (Vervoort and Blichert-Toft, 1999b; Vervoort et al., 1999;
521 Woodhead et al., 2012; Yogodzinski et al., 2010).

522 The εNd(t) and εHf(t) values for THO rocks vary between +5.7 to +8.2 and +14.9 to
523 +21.5 respectively; gabbro shows especially high εHf(t) (+21.5) (Fig. 14A). All the
524 samples plot near the field for modern Indian Ocean MORBs, suggesting a similar
525 mantle source (Chauvel and Blichert-Toft, 2001b). Figure 13B shows the results of bulk-
526 mixing calculations between mantle-derived MORB melts and various types of sediments
527 (Chauvel et al., 2009). Involvement of subducted Fe-Mn rich sediments (as well as
528 calcareous clays) in the mantle source affects Nd- more than Hf isotopic compositions
529 (Fig. 14B). In contrast, addition of continental sands will affect Hf as well as Nd isotopic
530 compositions, depending upon whether bulk assimilation of sediments or sediment melts
531 are involved. Also, the different Hf/Nd ratios of sediments are expected to have a large
532 influence, especially with the contribution of zircons in the subducted sediments.

533 In contrast to the Oman plagiogranites, which show strong involvement of sediment
534 melts in their magmatic reservoir (Haase et al., 2015), the mantle sources of the Torbat-e-
535 Heydarieh plagiogranites were not significantly affected by sediment melt addition or
536 crustal assimilation. However, the mantle source of the Torbat-e-Heydarieh magmatic
537 rocks could have been slightly affected by subducted pelagic sediments (high Nd/Hf
538 ratio), because they vary considerably in εNd(t). They have less radiogenic Nd- isotope
539 compositions than the igneous rocks of the Dehshir Late Cretaceous ophiolite (inner belt
540 Zagros ophiolites, Fig. 1 (Moghadam et al., 2010)). The Nd-isotope compositions of the

THO magmatic rocks are similar to those of the Sabzevar ophiolite from NE Iran, which have high but variable εNd (t) values (+5.4 to +8.3) and moderately high $^{207}Pb/^{204}Pb$ ratios (15.50-15-65) (Moghadam et al., 2014a). The Nd-Hf-Pb isotopic compositions of the Sabzevar-Torbat-e-Heydarieh rocks suggest a minor contribution of subducted sediments to the mantle source of these ophiolites from NE Iran.

ZIRCON GEOCHRONOLOGY

Four plagiogranites and two diabasic and gabbroic mantle-intruding dikes from the Torbat-e-Heydarieh ophiolite have been dated. We also analyzed five of these zircon separates for Hf-isotope compositions.

Sample TH11-23

This sample is taken from a plagiogranitic dike injected into the mantle diabasic dikes. Zircons are euhedral and prismatic and show magmatic concentric zoning (Fig. 15). These zircons contain 215-762 ppm U and have high Th/U ratios of 0.6-1.7 (Supplementary Table 6), consistent with a magmatic origin. Twenty-one analyses define a mean $^{206}Pb/^{238}U$ age of 99.32 ± 0.72 Ma (MSWD=1.4) (Fig. 15). This is interpreted as the time of plagiogranite crystallization. Zircons from this sample show a wide range of εHf (t), between ~ +8 and +16.1 (Supplementary Table 8).

Sample TH11-12

This sample is taken from a rodingitized gabbroic dike injected into mantle peridotites. The Th/U ratio of analyzed zircons varies between 0.47-0.69, consistent with a magmatic origin. Six analyzed grains yield a mean $^{206}Pb/^{238}U$ age of 96.7 ± 2.1 Ma (MSWD=0.32) (Fig. 15). This is the age of gabbroic dike intrusion and provides a

minimum age for the Torbat-e-Heydarieh ophiolite formation. Zircons from this sample show εHf (t) values that vary from ~ +9 to +16.9.

Sample TH11-82B

This plagiogranite intrudes mantle cumulate gabbros. Twenty-five zircons from this sample were dated by LA-ICPMS. Cathodoluminescence (CL) images show that the grains are medium-grained (<100 μm) and euhedral to subhedral (Fig. 15). Zircons have low to medium U (25-420 ppm) and Th (10-208 ppm) concentrations, and Th/U ratios vary between 0.4 and 0.7 (Supplementary Table 7), consistent with a magmatic origin. The $^{206}Pb/^{238}U$ and $^{207}Pb/^{235}U$ data define a concordia age of 91.9 ± 0.33 Ma (MSWD = 1.7). This is interpreted as the age of plagiogranite crystallization. Zircons from this sample show εHf (t) values of ~ +9.8 to +15.1 (Supplementary Table 8).

Sample TH11-74

This plagiogranite intrudes mantle cumulate gabbros. We analyzed fourteen zircons from this sample. CL images indicate magmatic zonation. Zircons have low to medium U (53-613 ppm) and Th (26-364 ppm) concentrations, and Th/U ratios vary between 0.5 and 1.3 (Supplementary Table 7). In the concordia diagram, fourteen analyses yield an age of 97.0 ± 1.3 (MSWD = 0.2) (Fig. 15). Zircons from this sample show εHf (t) values that vary from ~ +11.3 to +17.6.

Sample TH11-29

This sample is a diabasic dike within the mantle peridotites and contained only eight zircons. Zircons from this sample are prismatic (~<50 μm to ~100 μm). CL images show oscillatory zoning in some grains and some are less luminescent with weak zonation. Eight analyzed spots have high Th/U values (0.3 to 1.6). Five of the analyzed zircons

show concordant ages with weighted mean of $^{206}Pb/^{238}U$ age of 97.1 ± 1.2 (MSWD=0.6) (Fig. 15). The striking feature of this sample is the presence of three xenocrystic zircons with $^{207}Pb/^{235}U$ ages of ~1.1-1.5 Ga. Late Cretaceous zircons from this sample show εHf (t) values that vary from ~ +8.1 to +12.7, whereas the old zircons have εHf (t) values between +1.7 and +6.2 (Supplementary Table 8).

Sample TH11-20

Zircon grains from this sample, a plagiogranitic dike within the crustal gabbros, are long-prismatic and euhedral. Most crystals have magmatic zonation. Twenty-five analyses show low to moderate Th/U (~0.2-0.7) (Supplementary Table 7). Analyses are concordant, yielding a weighted mean age of 97.9 ± 0.6 Ma (MSWD= 1.4). This is interpreted as the crystallization age for this dike. Zircons from this sample show εHf (t) values that vary from ~ +13 to +18.5.

DISCUSSION

This new geochemical and isotopic dataset from the Torbat-e-Heydarieh ophiolites allows a detailed investigation of the mantle characteristics and the source of crustal rocks; the timing of back-arc basin opening and the relationship of this ophiolite to other Iranian ophiolites; the tectonic setting in which the Torbat-e-Heydarieh ophiolite formed; and the implications for understanding Late Cretaceous tectonic evolution in the region.

Sources of mantle peridotites and crustal melts

Mineral- and whole-rock compositions of various mantle peridotites, crustal gabbros, and effusive lavas classify the rocks into four different tectonic settings: abyssal

609 peridotite, supra-subduction zone fore-arc (FA), island-arc (IA), and back-arc basin
610 (BAB) settings.

611 ***Mantle peridotites of MOR origin***

612 Lherzolites and impregnated lherzolites show affinities with abyssal (MOR)
613 peridotites. Compositions of Cr-spinel and co-existing olivine all plot in a confined field
614 between fertile MORB-source mantle (FMM) and its partial melts (Figs. 9A-B). The
615 clinopyroxene and spinel compositions of impregnated lherzolites are similar to the
616 mineral compositions of lherzolites, suggesting these phases precipitated from the same
617 melts during the impregnation. The overall compositional trends show mixing between a
618 FMM source and its partial melting residue (F = ~ 9%). The trend may also represent
619 various degrees of extraction (lherzolite) and addition (impregnated lherzolite) of basaltic
620 melts (Fig. 10A). Clinopyroxene compositions in these rocks also plot within the
621 enriched part (TiO_2>0.2 wt. %) of the abyssal-peridotite field (Fig. 10C). Such variations
622 can form in the fractional to reactive melting regime in the spinel-stability field beneath a
623 spreading ridge (Kimura and Sano, 2012), as envisaged by the clinopyroxene REE
624 patterns with flat MREE to HREE and depleted LREE (Figs. 10A-C).

625 ***Dunite of SSZ fore-arc origin***

626 Spinels in dunite samples are rich in Cr and Ti and their compositions plot close to
627 the boninite and IAT basalt field (Figs. 9A-B). They plot away from the abyssal
628 peridotite field, into the SSZ field. Because of the proximity of the compositions of spinel
629 and clinopyroxene to those of boninite or IAT, these are most like SSZ fore-arc
630 peridotites.

631 ***Plagioclase lherzolite and cumulate gabbro of SSZ-IA origin***

632 Cumulate gabbros contain low-Mg# clinopyroxene and An-rich (~90) plagioclase.
633 These are features of assemblages formed from water-rich arc basalt magmas (e.g.,
634 (Hamada and Fujii, 2008)). Therefore, the gabbros are most similar to arc magmas
635 (Ishizuka et al., 2014).
636 Spinels in plagioclase lherzolites show intermediate abundances of Cr and Ti (Figs.
637 9A-B). Clinopyroxenes have low Mg# and are poor in Ti, similar to cumulate gabbros.
638 The low Ti content of clinopyroxenes from plagioclase lherzolites suggest crystallization
639 from a SSZ-derived melt during magmatic impregnation. The Cr and Ti compositions of
640 plagioclase lherzolite spinels lie between the fields of abyssal peridotite and basalt (Fig.
641 10A); however, Mg# in the spinel plots away from abyssal peridotite but close to SSZ-
642 FA peridotite. Considering the Mg#-rich spinel and Mg-poor clinopyroxene together
643 (Figs. 9B-C), the plagioclase lherzolites suggest affinities with island-arc tholeiites.
644 The REE patterns of clinopyroxenes from cumulate gabbros show depleted MREE to
645 HREE relative to MOR gabbros with elevated Sr (Fig. 11B). Plagioclase lherzolites show
646 the same feature, with more depleted MREE to HREE and elevated Sr (Fig. 11D). Low
647 REE abundance is the signature of a depleted mantle source and elevated Sr may reflect
648 addition of metasomatic slab-derived fluid. Sr enrichment in plagioclase-bearing
649 peridotites is also suggested to postdate melt impregnation and could be the result of
650 high-temperature (370-850 °C) breakdown of plagioclase, which liberated Sr to enrich
651 adjacent pyroxenes (Pirnia et al., 2014).
652 The lower abundances of Zr in plagioclase lherzolites relative to lherzolites and
653 depletion in HFSE in the mantle and gabbro sources are consistent with hydrous

654 metasomatism (Arai et al., 2006; Khedr and Arai, 2009). This feature is most consistent
655 with a SSZ-FA origin of the mantle-crust lithologies.

656 ***Harzburgite and Cpx-harzburgite of BAB origin***

657 Spinels in harzburgite have intermediate Mg# (66-76) and partially overlap lherzolite
658 fields (Figs. 9A-B). In contrast, spinels with lower Ti and higher Cr than those of
659 lherzolite are more depleted (Figs. 9A-B). Ti contents are low in both clinopyroxenes and
660 dunite, suggesting a SSZ signature (Fig. 10C). Any further constraints on harzburgite
661 tectonic affinities are difficult to identify.

662 Cpx-harzburgite forms common geochemical trends with harzburgite. They plot
663 between abyssal basalt, abyssal peridotite, and SSZ dunite (Figs. 9A-C). The depleted
664 nature of these rocks implies that harzburgite was impregnated by MORB or IAT melt
665 (Figs. 9A-C). It is difficult to identify the impregnated melts as either MOR or IA.
666 However, the harzburgites are distinct from abyssal peridotites suggesting involvement of
667 strongly depleted mantle (F = ~12%: Fig. 9A). Such highly depleted sources can occur in
668 fore-arc or BAB settings (Hirahara et al., 2015). We thus conclude that harzburgite and
669 cpx-harzburgite probably formed in a fore-arc or BAB.

670 No Cpx-REE data are available for the Cpx-harzburgites. Some insight may be
671 gained by considering harzburgite clinopyroxenes from the nearby Sabzevar ophiolite.
672 These are extremely depleted (Fig. 11D) consistent with a SSZ mantle origin of the NE
673 Iran ophiolite harzburgites and impregnated harzburgites.

674 ***Isotropic and cumulate gabbros: back-arc basin or fore-arc origin?***

675 Isotropic gabbros show flat to slightly LREE-depleted patterns with lower total
676 abundances than N-MORB, along with Nb-Ta troughs and elevated La and Th (Fig.

12B). These geochemical features are close to those of FAB from the IBM fore-arc (Reagan et al., 2010), although Nb-Ta depletions are greater in THO rocks. One microgabbroic dike is similar, with more elevated trace element abundances and no Eu anomaly (Figs. 11A-B). This may represent a melt-rich part of the gabbros. Although some depleted IA basalts generated during BAB opening show similar trace element patterns, these are generally richer in Pb, Th, and LREEs (e.g., (Shinjo et al., 1999)). Similarly, enriched E-type MORB erupted in the Sea of Japan back-arc basin during its opening at ~17 Ma (Hirahara et al., 2015). Depleted D-type MORB is also associated with the opening of the Sea of Japan (Hirahara et al., 2015). Sea of Japan D-type basalts are geochemically

similar to THO isotropic gabbros, apart from depleted HREE due to residual garnet in the source of the former basalts (Hirahara et al., 2015). According to these considerations, we find that the isotropic gabbros are most similar to FA or BAB.

In contrast to the isotropic gabbros, cumulate gabbros show elevated Sr, Pb, Ba, and Eu anomalies due to plagioclase accumulation. LREE-depleted patterns reflect cumulate clinopyroxene, but the patterns still show Nb-Ta depletion relative to La and Th. This is similar to gabbros of FA or BAB origin. The loss of melt from cumulate gabbros and the concentration of some cumulate minerals could explain the different chemistries of isotropic and cumulate gabbros (Figs. 11A-B). Plagioclase is anorthite-rich (Fig. 10D), suggesting that these gabbros most likely originated from water-rich basaltic melts (Hamada and Fujii, 2008). All of the above observations indicate that the THO gabbros are most similar to FA or BAB basalts.

699 It is hard to specify the tectonic setting of the SSZ gabbros from geochemistry alone;
700 this is consistent with fore-arc, arc, or back-arc basin settings.

701 ***Pillow and massive basaltic lavas, dikes within mantle of IA-BAB origin***

702 Most lavas show slightly LREE-depleted flat patterns with slight Nb depletion and
703 slight Th enrichment. The pattern is akin to N-MORB, FAB, or BABB. These features
704 are further examined below using Th/Yb and Th/Ce ratios.

705 A useful observation is the lack of boninite in the THO. Fore-arc volcanic sequences
706 are frequently but not always associated with boninite and high-Mg andesite ((Ishizuka et
707 al., 2014; Reagan et al., 2010) for IBM; (Ishikawa et al., 2002) for Oman ophiolite). In
708 the fore-arc setting, boninites are suggested to be generated 2-4 m.yr. later than fore-arc
709 basalts, when the residual, highly depleted mantle melted at shallow levels after
710 interaction with a water-rich fluid derived from the subducting slab (Ishizuka et al., 2014;
711 Reagan et al., 2010). However, boninite does not occur in the THO, suggesting that it did
712 not form in a fore-arc subduction-initiation setting.

713 One pillow-lava sample is enriched in LREE, like E-MORB (Fig. 12D). This sample
714 is similar to OIB-like pillow and massive lavas from the Sabzevar ophiolite (Moghadam
715 et al., 2014a). E-MORB occurs either in MOR or in BAB as an along-ridge geochemical
716 variation (e.g., (Kelley et al., 2013)). E-MORB also occurred in the SW Japan FA when
717 subduction re-initiated at 15 Ma (Kimura et al., 2005). E-MORB occurs all over MOR-
718 FA-BAB settings, so its presence does not constrain the setting of THO. Melting of
719 enriched subcontinental lithosphere might be responsible for generating THO E-MORB-
720 like lavas.

721 Two of the most depleted samples have strong Nb depletions and strong Th
722 enrichments (Fig. 12D). REEs are more depleted than MORBs, but with elevated LILEs
723 such as Sr, U, and Ba. These are IAT-like basalts; such basalts occur in BAB and in fore-
724 arcs.

725 ***Plagiogranites and amphibole gabbros of IA-BAB origin***

726 Plagiogranites and amphibole gabbros all have arc-magma signatures including Nb-
727 Ta troughs and strong Th enrichment (Fig. 12F). HREEs are strongly depleted, similar to
728 IAT-type pillow lavas. LREEs are highly enriched in both lithologies with greater LILE
729 enrichment in amphibole gabbros. Sample TH11-9B geochemically resembles E-MORBs
730 with enriched LREEs and less Nb depletion. Elevated Sr and Eu contents in the
731 plagiogranites are probably due to plagioclase accumulation. Positive Zr-Hf anomalies in
732 the amphibole gabbros and host rocks of plagiogranites are likely to reflect preferential
733 partitioning of these elements into amphibole during fractional crystallization (Tiepolo et
734 al., 2007) (Fig. 12F).

735 ***Nb/Yb - Th/Yb discrimination***

736 (Pearce, 2008) proposed that Th/Yb *vs* Nb/Yb relationships could distinguish
737 MORB-OIB from SSZ igneous rocks. Most THO lavas and crustal gabbros show
738 elevated Th/Yb at moderate to low Nb/Yb, consistent with subduction contributions
739 (sediment melt) to a moderately depleted mantle source (Fig. 16A). Exceptions are
740 TH11-70, TH11-33, TH11-32, TH11-64, TH11-67, TH11-66, which plot along the
741 MORB-OIB array within the N-MORB field, and TH11-39 pillow lava and TH11-9B
742 amphibole gabbro, which plot along the MORB-OIB array within the E-MORB field.
743 Other lavas and gabbros have Nb/Yb similar to N- and E-MORB, but have elevated

744 Th/Yb (Fig. 16A). Pillow and massive lavas, mantle dikes and cumulate gabbros have
745 low Nb/Yb, whereas amphibole gabbros and plagiogranites show high Nb/Yb indicating
746 derivation of these magmas from more- and less-depleted mantle sources, respectively
747 (Pearce, 2008).

748 ***Th/Nb - Ce/Nb discrimination***

749 Similar conclusions are reached based on the Th/Nb - Ce/Nb plot (Fig. 16B)
750 (Sandeman et al., 2006). Most lava flows (TH11-70, TH11-33, TH11-32, TH11-64,
751 TH11-67, TH11-66) and the TH11-9A amphibole gabbro have MORB signatures
752 whereas TH11-39 pillow lava and TH11-9B amphibole gabbro are similar to Sabzevar
753 OIB-type lavas. These are in turn similar to Lau Basin BAB and Okinawa Trough intra-
754 arc rift lavas. In contrast, other IA-BAB-type lavas, isotropic gabbros, amphibole
755 gabbros, and mantle dikes have lower Ce/Th, plotting close to Okinawa Trough BABs.
756 Overall, THO magmatic rocks including lavas, gabbros, and plagiogranites plot between
757 MORB and Mariana arc lavas, and therefore indicate generation from a heterogeneous
758 DMM source mantle that was variably fluxed by slab fluids.

759 The above considerations support a BAB origin for the THO magmatic rocks. Only
760 plagiogranites and amphibole gabbros show strong IAT signatures (Fig. 12D). These
761 geochemical signatures resemble Sabzevar ophiolite magmatic rocks (Moghadam et al.,
762 2014a).

763 ***Zr/Nb - Hf/Nb and Th/Nd - $^{143}Nd/^{144}Nd$ discrimination diagrams***

764 The composition of BAB basalts varies significantly, indicating that BABB melts are
765 derived from heterogeneous mantle sources, which range from depleted to enriched and
766 from MORB-like to arc-like (Stern, 2002; Taylor and Martinez, 2003). The THO igneous

767 rocks are LREE-depleted or slightly enriched relative to N-MORB, similar to BABB
768 (Fig. 12) like those of the Lau Basin (Tian et al., 2011) and Okinawa Trough (Shinjo,
769 1999). The THO igneous rocks involve both depleted (FAB and D-type BABB-like
770 igneous rocks) and enriched (E-BABB and E-MORB-like rocks) mantle components, a
771 conclusion which is supported by the plot of Hf/Nb *vs* Zr/Nb (Sorbadere et al., 2013)
772 (Fig. 16C).

773 To better understand the contribution of slab-derived components to the mantle
774 source of THO igneous rocks, we used a plot of Th/Nb *vs* $^{143}Nd/^{144}Nd$ (Fig. 16D). THO
775 igneous rocks reflect variable enrichment by sediment melts, as shown on Fig. 16D
776 (Sorbadere et al., 2013). THO melts are like those of the Sabzevar ophiolite, which
777 sampled multiple mantle and slab components, again consistent with a BAB
778 interpretation.

779 ***Whole rock Nd-Hf and zircon Hf isotopes***

780 Whole rock (εHf=+14.9 - +21.5) and zircon (εHf= +8.1 - +18.5) Hf- isotope data
781 from the Torbat-e-Heydarieh ophiolite are comparable. These data indicate that the
782 mantle source beneath the THO back-arc was broadly MORB-like (Todd et al., 2011;
783 Woodhead et al., 2012; Woodhead and Devey, 1993). However, this mantle source also
784 had slightly enriched components (Stracke et al., 2005), as shown by Hf and Nd isotopic
785 data (Fig. 14).

786 All THO lavas seem to be derived from an Indian MORB source mantle (I-DMM),
787 similar to the source of the Oman ophiolitic gabbros. The addition of HFSE such as Hf
788 occurs if subducted sediments are melted or if supercritical fluids are involved (Kessel et
789 al., 2005). The THO igneous rocks vary modestly in εHf and εNd, indicating restricted

790 contributions of subducted sediment melts. We conclude that the THO pillow lavas and
791 massive lavas reflect derivation from an Indian Ocean DMM mantle that may have been
792 slightly affected by melts of subducted sediments, although some isotropic gabbros and
793 E-MORB lavas show a modestly-enriched mantle signature.

794 It is worth noting that THO Hf-isotope compositions are similar to those of the
795 Zagros fore-arc ophiolites, both inner belt (Nain-Baft; εHf (t) = +8 - +21) and outer belt
796 (Neyriz-Kermanshah; εHf (t) = +10 - +23) ophiolites, confirming a broadly similar
797 mantle source for the generation of Late Cretaceous Iranian ophiolitic magmas. However,
798 the conspicuous variations in the zircon εHf values (+8.1 - +18.5) (which are similar to
799 the whole rock Hf isotope variations; εHf=+14.9 - +21.5), can reflect mixing with new
800 pulses of similar magmas but with slight isotopic differences entering the magma
801 chamber duringcooling of the plagiogranitic melts (Shaw and Flood, 2009).

802 ***Heterogeneous mantle sources for THO magmas: further thoughts***

803 Table 1 summarizes possible sources and tectonic affinities of the studied THO
804 rocks. As discussed above, lherzolites and impregnated lherzolites are similar to MOR
805 abyssal peridotite. Dunites are most like SSZ-FA mantle whereas plagioclase lherzolites
806 are most like sub-arc mantle. Plagiogranites and amphibole gabbros also have strong arc
807 affinities. Lavas, dikes in peridotite, other gabbros, and harzburgites have the strongest
808 affinities with BAB (Table 1).

809 Cumulate gabbros are melt-deficient equivalents of isotropic gabbros; both are
810 probably derived from Nb-Ta depleted N-MORB-like magmas like THO pillow and
811 sheet lavas. Harzburgite is probably melt-depleted residual BAB mantle as indicated by
812 Cr# and TiO_2 contents of its spinels (Fig. 10). The Cpx-harzburgite is similar to melt-

impregnated harzburgite but with greater addition of abyssal basalt melt (Fig. 10A). "Abyssal basalt" in this case is not N-MORB but BAB basalt with signatures of slab-derived fluids. Cpx-harzburgites may represent reactive melt flow channels (Kimura and Sano, 2012). Magmas so generated could have formed dikes within the mantle near the Moho mantle and could have fractionated to form isotropic and cumulate gabbros. Some of this magma may have erupted as pillow lavas and sheet lavas to form BAB oceanic crust Layer 2 (Hirahara et al., 2015).

The presence of heterogeneous mantle rocks (with affinities to FA, IA, and MOR) associated with THO BAB is consistent with the inferred tectonic setting of the THO.

Tectonic significance of the Torbat-e-Heydarieh ophiolite

Timing of back-arc basin opening and its relation to Zagros subduction initiation

Strong upper plate extension accompanies the initiation of some subduction zones such the Izu-Bonin-Mariana convergent margin, south of Japan. Strong extension on the upper plate of a nascent subduction zone, above the sinking lithosphere, allows asthenospheric upwelling and leads to seafloor spreading, forming infant arc crust of the proto-forearc (Stern, 2004; Stern and Gerya, 2017). (Gurnis et al., 2004; Hall et al., 2003) suggest that rapid trench retreat and extension in the overriding plate also occur after subduction becomes self-sustaining, others believe that trench roll-back (and back-arc extension) can start after the slab pull becomes greater than the far-field push (Baes et al., 2011).

Late Cretaceous Zagros ophiolites and their ~3000 km long equivalents in Oman and from the Mediterranean area (Cyprus, Turkey, Syria to Iraq) show a site of Late

836 Cretaceous subduction initiation along the southern margin of Eurasia (Moghadam and
837 Stern, 2011; Monsef et al., 2018). The chemo-stratigraphic relationships of the lavas from
838 these ophiolites, integrated with mantle geochemistry and paleomagnetic data, support
839 the idea of arc infancy at the southern margin of Eurasia during the Late Cretaceous
840 (Dilek et al., 2007; Maffione et al., 2017; Moghadam and Stern, 2011; Monsef et al.,
841 2018; Pearce and Robinson, 2010). It is also suggested that the earliest subduction stage
842 after the SI coincided with the transient transfer of high-pressure rocks from the top of
843 the subducting slab to the overriding plate (van Hinsbergen et al., 2015). Late Cretaceous
844 high-pressure rocks are common within the Oman and Zagros ophiolites (Guilmette et al.,
845 2018; Moghadam et al., 2017a), and further attest to the transfer of deep-seated rocks
846 during the earliest stage of subduction.

847 Because of their setting far to the north of the Late Cretaceous Zagros SI plate
848 margin, STHO ophiolites must have formed in a back-arc basin. They are easily related to
849 the Late Cretaceous (~104-98 Ma) formation of a new subduction zone along the
850 southern margin of Iran, where seafloor spreading formed new oceanic lithosphere
851 (Zagros inner and outer belts ophiolites) (Moghadam and Stern, 2015). Subduction
852 initiation was followed quickly by arc magmatism to form the Urumieh-Dokhtar
853 Magmatic Belt (e.g., (Chiu et al., 2013; Ghasemi and Manesh, 2015; Ghorbani et al.,
854 2014; Honarmand et al., 2014)). Opening of the STHO BAB probably reflected strong
855 regional extension of the overriding plate during subduction initiation. Our zircon U-Pb
856 ages range from ~99 to 92 Ma, reflecting a period of ~7 Myr for formation of the THO
857 ophiolite. A similar age range is also indicated by Cenomanian to Turonian (~ 99-90 Ma)
858 carbonates deposited over the massive and pillow lavas.

Such a broad zone of extension accompanying SI is consistent with IODP 351 drilling results west of the IBM arc, where scientists were surprised to find Eocene basalts far west of where subduction began at ~51 Ma (Hickey-Vargas et al., 2018). The dominance of Late Cretaceous extension in NE Iran is also confirmed by the presence of a sheeted dike complex in the Sabzevar ophiolites with U-Pb ages of ~90 Ma obtained from the felsic dikes (Moghadam et al., 2014b). This extension was also associated with basement-involved low-angle normal faulting, core complex exhumation, block tilting and sedimentary basin formation in some parts of Iran (e.g., in Saghand, Fig. 1 (Verdel et al., 2007), in Golpayegan (Moritz and Ghazban, 1996) and in Torud (Malekpour-Alamdari et al., 2017), attested by ^{39}Ar-^{40}Ar and K-Ar ages. These results show that extensional deformation prevailed during Late Cretaceous in what is now the Iranian plateau. Extension in NE Iran also generated a volcano-sedimentary basin (Southern Sabzevar basin, N-NW of Oryan) which was filled by Late Cretaceous pelagic sediments, green siliceous tuffs and submarine volcanic rocks (Kazemi et al., 2019). Late Cretaceous extension also allowed asthenospheric melts with radiogenic isotopic compositions to invade the continental crust and generate granitoids and lavas with radiogenic Nd and zircon Hf isotopic compositions (e.g., (Alaminia et al., 2013; Kazemi et al., 2019)).

Tectonic setting of the Torbat-e-Heydarieh ophiolite

Three key questions concerning the Tobat-e-Heydarieh ophiolite are addressed here: 1) What is the relationship between the Sabzevar and Torbat-e-Heydarieh ophiolites? 2) What is the relationship between STHO ophiolites and other ophiolites of similar age in eastern Iran? 3) What is the relationship between the Zagros fore-arc ophiolites and the STHO?

882 The ages obtained here agree with U-Pb zircon ages of 100 to 78 Ma for the
883 Sabzevar ophiolite (Moghadam et al., 2014a). THO ages are also similar to zircon U-Pb
884 ages obtained for dacitic-andesitic lavas from the Cheshmeshir and Oryan ophiolites
885 (~102-76 Ma, Fig. 3; *Moghadam et al., unpublished data*). Some of the younger ages
886 may reflect arc magmatism. Together, results from the THO, Sabzevar and
887 Cheshmehshir-Oryan ophiolites indicate a Late Cretaceous oceanic basin that was
888 magmatically active and perhaps open for ~26 Ma. Our age results indicate that the
889 Zagros SI may be somewhat older than the formation of the NE Iran back-arc basins
890 (104-98 Ma *vs* 99-92).
891 Late Cretaceous mantle upwelling accompanying extension led to the emplacement
892 of several juvenile intrusions and associated extrusive rocks (Late Cretaceous-Eocene
893 magmatic belt in Fig. 3). These Late Cretaceous igneous rocks are abundant in NE Iran
894 and are mostly juvenile additions from the mantle to the crust. Xenocrystic zircons (with
895 ages of 1.1-1.5 Ga) from sample TH11-29 (diabasic dike within peridotites) suggest that
896 recycling of ancient subducted materials accompanied back-arc opening. These
897 xenocrytic zircons are found in many Neotethyan ophiolites in China and the
898 Mediterranean realm (e.g., (Gong et al., 2016; Robinson et al., 2015)).
899 The Torbat-e-Heydarieh ophiolite probably represents an extension of the Sabzevar
900 ophiolite. Although the formation age of these ophiolites (Sabzevar and THO) is nearly
901 synchronous, there are striking differences in the tectono-metamorphic evolution of the
902 two ophiolite belts. The main differences include: 1- mantle peridotites are more
903 important in the THO and spinels from Sabzevar mantle peridotites have SSZ- or fore-
904 arc-type signatures, characterized by higher Cr# (Shafaii Moghadam et al., 2015) (Fig.

905 10B). 2- Podiform chromitites are rare in the THO and abundant in the Sabzevar
906 ophiolite; 3 -Acidic volcanic rocks are abundant in Sabzevar, whereas mafic volcanics
907 are more important in the THO (Fig. 13A). Sabzevar volcanic rocks show more
908 pronounced arc signatures than do those of the THO, indicated by higher Th/Yb, Th/Nb
909 and Ce/Nb ratios (Figs. 15A-B). 4- OIB-type lavas are present in Sabzevar (Moghadam et
910 al., 2014a) but are absent in the THO, although the latter contains minor E-MORB. 5-
911 The Sabzevar ophiolite marks an orogenic suture, with a Paleocene HP/LT metamorphic
912 core (Omrani et al., 2013; Rossetti et al., 2014) and an external thrust-and-fold belt,
913 showing evidence of a ductile-to-brittle top-to-the-SSE sense of tectonic transport
914 (Rossetti et al., 2014). Moreover, a HP granulite event, Albian in age, may exist in the
915 Sabzevar zone (Nasrabady et al., 2011; Rossetti et al., 2010). Conversely, the Torbat-e-
916 Heydarieh ophiolite realm does not show evidence of orogenic metamorphism, and the
917 post-Cretaceous tectonic evolution has been controlled by polyphase strike-slip shearing
918 (Tadayon et al., 2017).

919 The observation that all Sabzevar lavas and mantle peridotites have SSZ signatures
920 whereas THO lavas and peridotites have mostly MORB-like signatures, as well as the
921 presence of older high-P rocks in the Sabzevar and their absence in the Torbat-e-
922 Heydarieh, may indicate that the Torbat-e-Heydarieh and Sabzevar ophiolites represent
923 distinct back-arc basins, differing proximities to the arc, or different stages in BAB
924 opening. It is probably not realistic to consider two neighboring oceanic basins so close
925 together in NE Iran during Late Cretaceous time, although distinct rift basins existed due
926 to strike-slip faulting accompanying break-up of the continental lithosphere in NE Iran.
927 We prefer to interpret STHO ophiolite fragments as having formed in a single back-arc

basin, perhaps in distinct extensional basins (grabens), developed during Late Cretaceous hyperextension in the region.

Regarding the second question, what is the relationship of STHO to other Late Cretaceous oceanic remnants in eastern Iran? We believe that back-arc opening experienced distinct spatio-temporal and geodynamic evolution, but nearly all formed due to the extensional regime which prevailed in the region during the latest Early to Late Cretaceous (~110-70 Ma). The Birjand-Zahedan ophiolites in eastern Iran (Fig. 1) are similar in age to the STHO. SHRIMP U-Pb zircon dating of metafelsic rocks and eclogites from the Birjand-Zahedan ophiolites gave ages of ~ 86-89 Ma (Bröcker et al., 2013) (Fig. 13). In addition, zircon U-Pb ages from Birjand-Zahedan gabbros are somewhat older than STHO ophiolites; 113-107 Ma (Zarrinkoub et al., 2012). These may be related to a different episode of Early Cretaceous subduction in the region. Zircon and titanite from felsic segregations in mafic granulites from the Sabzevar ophiolite yield U-Pb ages of 107.4±2.4 and 105.9±2.3 Ma, respectively (Fig. 13; (Rossetti et al., 2010)). This evidence might suggest the formation of Early Cretaceous (i.e. pre-Albian) Sabzevar-Birjand-Zahedan single oceanic realm in the upper plate above a Neothethys subduction zone. In fact, the formation of these high HP granulites in a subduction zone is questionable, as these rocks contain no high-P minerals and its zircon U-Pb age (ca. 107 Ma) is similar to its titanite age (ca. 105 Ma) and both are similar to the zircon U-Pb ages reported from the felsic to mafic magmatic rocks from the Sabzevar area (Fig. 3). Therefore, we believe these metamorphic rocks (with amphibole-plagioclase-garnet ± titanite as rock-forming minerals) had a mafic protolith and were not metamorphosed in a subduction zone. It seems that a MORB precursor related to 105 Ma granulites existed in

951 the Sabzevar area during the Lower Cretaceous (Nasrabady et al., 2011). This may imply
952 that an oceanic crust older than 105 Ma was present in NE Iran, before the Torbat-e-
953 Heydarieh back-arc basin start to open.

954 Finally, what is the relationship between Zagros ophiolites and the STHO? There are
955 geochemical similarities, but Zagros ophiolites are mostly slightly older (*ca* 104-98 Ma)
956 than the STHO (*ca* 99-80 Ma). This may reflect the migration of extension accompanying
957 subduction initiation; first in what becomes the fore-arc, then as the slab descends the
958 locus of extension migrates to the back-arc region (Fig. 17A). In this scenario, the STHO
959 represents a back-arc basin that formed behind the Zagros fore-arc and the nascent
960 Urumieh-Dokhtar magmatic arc (Fig. 17B). Back-arc opening would have disrupted
961 Cadomian continental crust, including Cadomian subcontinental lithospheric mantle
962 (SCLM; the Lu-Hf *vs* Hf plot, *not shown*, indicates an isochron with a Cadomian mantle-
963 depletion age of ~585 Ma). Involvement of such SCLM may explain the origin of OIB-
964 type lavas in the Sabzevar ophiolite and E-MORB in THO. How far west this back-arc
965 basin can be traced remains unclear, because the region to the SW between the STHO
966 and the Nain ophiolites of similar age is covered by younger deposits for ~400 km (Fig.
967 1). Geophysical studies of this region including magnetics and gravity may help answer
968 this question.

969 It is also unresolved when and why the STHO BAB collapsed. U-Pb ages for THO
970 indicate a lifespan of ~7 million years, slightly less than the lifespan of 12.5±4.7 Ma for
971 global extinct BABs (Stern and Dickinson, 2010). One possibility is that the Iranian
972 continental lithosphere had been weakened by prolonged arc igneous activity, allowing
973 the basin to collapse when regional stress changed from extension to compression as the

974 subduction zone evolved. There is abundant evidence for prolonged arc igneous activity
975 from Late Cretaceous time onwards (e.g., (Chiu et al., 2013; Honarmand et al., 2014;
976 Hosseini et al., 2017; Verdel et al., 2011)). The volcano-pelagic series above the STHO
977 includes Cenomanian to Maastrichtian deep-sea pelagic sediments interbedded with
978 pyroclastic and andesitic to dacitic lavas. Dacitic-andesitic lavas from the Cheshmehshir
979 and Oryan ophiolites have Late Cretaceous (~102-76 Ma) U-Pb ages (*Moghadam et al., unpublished data*). This sequence grades upward into a series of Maastrichtian to
980
981 Paleocene shallow water sediments and then into the Oryan marine sediments (lower and
982 middle Oryan sediments) from early Eocene to early middle Eocene. Moreover, zircon U-
983 Pb ages for plutonic rocks from south of Sabzevar and Neyshabour (Fig. 3, between the
984 Sabzevar ophiolite in the north and the Cheshmeshir ophiolite in the south) are of
985 Cenomanian-Maastrichtian (97.0± 0.2 Ma; 67.5±0.5 Ma) to Oligo-Miocene (29.8 ± 0.2
986 Ma) (*Moghadam et al., unpublished data*; (Alaminia et al., 2013)). The Late Cretaceous
987 ages are similar to the U-Pb zircon ages of the Sabzevar plagiogranites (100 to 78 Ma).
988
989 **CONCLUSIONS**
990 Our study of the THO confirms that it formed in Late Cretaceous time. Dikes
991 intruding THO mantle peridotites and plagiogranites have U-Pb ages of 99-92 Ma. THO
992 igneous rocks have a range of εNd(t) between +5.7 - +8.2 and their εHf(t) values range
993 from +14.9 to +21.5; THO zircons have εHf(t) values of +8.1 - +18.5. Like all NE Iran
994 ophiolites, the THO is found in a tectonic position well to the north of slightly older
995 Zagros fore-arc ophiolites and the Urumieh-Dokhtar magmatic belt, and thus appears to
996 have formed as a continental back-arc basin. Petrological, geochemical, and isotopic

997 compositions are consistent with this interpretation. THO peridotites contain spinels and
998 clinopyroxenes with compositions like those in peridotites from mid-ocean ridges and
999 back-arc basins. THO igneous rocks have Hf-Nd isotopic compositions that are similar to
1000 Indian Ocean MORBs, and do not show clear evidence for addition of sediment-derived
1001 melts or fluids from a subducted slab. Magmatic rocks in the Torbat-e-Heydarieh
1002 ophiolite show both MORB-like and SSZ geochemical signatures. We conclude that
1003 formation of the Sabzevar- Torbat-e-Heydarieh ophiolite reflects opening of a Late
1004 Cretaceous back-arc basin as a result of regional hyper-extension accompanying
1005 subduction initiation along southern Iran.
1006

1007 **ACKNOWLEDMENTS**

1008 This is contribution 1236 from the ARC Centre of Excellence for Core to Crust Fluid
1009 Systems (http://www.ccfs.mq.edu.au), 1275 from the GEMOC Key Centre
1010 (http://www.gemoc.mq.edu.au), and UTD Geosciences contribution number 1343 and is
1011 related to IGCP-662. Zircon U-Pb geochronology, clinopyroxene *in situ* trace elements
1012 and zircon Lu-Hf isotope data were obtained using instrumentation funded by DEST
1013 Systemic Infrastructure Grants, ARC LIEF, NCRIS/AuScope, industry partners, and
1014 Macquarie University. We thank Prof S. Arai for his support during EMP analysis at
1015 Kanazawa University. We are very grateful to Federico Rossetti, an anonymous reviewer
1016 and GSA Bulletin's associate editor for their constructive reviews of the manuscript.
1017 Editorial suggestions by Brad Singer are appreciated. All logistical support for field
1018 studies came from Damghan University.
1019

FIGURE CAPTIONS

Fig. 1- Simplified geological map of Iran emphasizing Cadomian rocks, the main ophiolitic belts (thick dashed lines) and Cenozoic magmatic rocks. A-B line shows the cross-section position in Fig. 2C.

Fig. 2- (A) and (B) Schematic model showing the opening and evolution of the Sabzevar-Torbat-e-Heydarieh back-arc basin relative to the Zagros, Neotethyan Ocean (modified after (Dercourt et al., 1986; Kazmin et al., 1986).

Fig. 3- Geological map of the Sabzevar-Torbat-e-Heydarieh region, north of the Dorouneh Fault, with emphasis on the distribution of ophiolitic and arc-related rocks. (Abbreviations are M et al.= *Moghadam et al., unpublished data*; K et al.= (Kazemi et al., 2019); M et al., 2014= (Moghadam et al., 2014a)).

Fig. 4- Simplified geological map of the Torbat-e-Heydarieh ophiolite (modified after (Vaezi Pour et al., 1992)).

Fig. 5- Simplified stratigraphic column displaying idealized internal lithologic successions in THO.

Fig. 6- Outcrop photos of the THO rock units. (A) outcrops of mantle peridotites. (B) Rodingitized dikes within the THO mantle peridotites. (C) Outcrop of interlayered cumulate gabbros (layered gabbros) and clinopyroxenites. (D) Small intrusions of cumulate (layered) gabbros within the THO mantle sequence. (E) Plagiogranitic dikes within the mantle gabbroic intrusions. (F) Angular gabbroic xenoliths within the plagiogranitic pockets. (G) Outcrops of crustal massive and pillow lavas. (H-I) Late Cretaceous (Cenomanian to Turonian, ~ 99-90 Ma) pelagic sediments are interlayered with and conformably cover the lavas.

Fig. 7- Photomicrographs of the THO mantle peridotites and gabbros. (A) Opx, Cpx and serpentinized olivine in lherzolites. (B) Serpentinized olivines, Opx and Cpx grains as embayment within the Opx in Cpx-harzburgites. (C) Serpentinized olivine, Opx and Cpx aggregates within the impregnated lherzolites. (D) Coarse-grained Cpx crystals and altered plagioclase in plagioclase-bearing lherzolites. (E) and (F) Opx, Cpx and plagioclase in mantle cumulate gabbros.

Fig. 8- Back-scattered images of THO mantle rocks. (A) Association of clinopyroxene and vermicular spinels at the embayments of orthopyroxene porphyroclasts in Cpx-harzburgites. (B) Altered plagioclase enclosed by large Cpx grains in plagioclase lherzolites. (C) Olivine, Opx, Cpx and plagioclase in plagioclase lherzolites. (D) Cpx and chloritized amphibole inclusions in the chromite of dunites. (E) and (F) Cumulate texture in mantle cumulate gabbros with early crystallized Opx and Cpx and late-stage, interstitial plagioclase crystals.

Fig. 9- Modal composition of THO mantle peridotites (A) and gabbros (B).

Fig. 10- (A) Relationship between Cr# and TiO_2 contents of spinel in mantle peridotites of the Torbat-e-Heydarieh ophiolite. The thick gray arrow shows the effect of melts (with composition of Troodos boninites) on refractory subduction-zone peridotites. Compositions of Tonga and Izu-Bonin-Mariana island arc tholeiites and abyssal basalts are from (Pearce et al., 2000a) and the composition of Troodos boninite is from (Dick and Bullen, 1984). (B) Relationship between Cr# and Mg# of spinels in Torbat-e-Heydarieh mantle peridotites. Abyssal-peridotite fields are from (Dick and Bullen, 1984), fore-arc-peridotite field is from (Pearce et al., 2000a). Data on Sabzevar peridotites are from (Moghadam et al., 2014a). (C) Mg# *vs* TiO_2 contents of clinopyroxene from

peridotite and mantle gabbro (abyssal and fore-arc peridotite fields are from (Bedard et al., 2009). (D)- Anorthite content *vs* clinopyroxene Mg# (modified after (Sanfilippo et al., 2013)) in Torbat-e-Heydarieh gabbroic rocks. The Kizildag ophiolite data are from (Bagci et al., 2005). Fields of MORB and arc gabbro are from (Burns, 1985).

Fig. 11- Abundances of Rare Earth Elements and other trace elements in clinopyroxene in lherzolites and cumulate gabbros (A-B) and impregnated and plagioclase lherzolites (C-D), from the Torbat-e-Heydarieh ophiolite. Chondrite normalization values are from (Mcdonough and Sun, 1995). Fields for abyssal and supra-subduction zone (SSZ-) peridotite clinopyroxenes are from (Bizimis et al., 2000; Johnson et al., 1990). The composition of MOR cumulate Cpx is from (Ross and Elthon, 1993). Data on Sabzevar ophiolite rocks are from (Shafaii Moghadam et al., 2015).

Fig. 12- Chondrite-normalized REE patterns (chondritic abundances from (Mcdonough and Sun, 1995)) and primary mantle and N-MORB normalized multi-element patterns (N-MORB and primary mantle concentrations from (Mcdonough and Sun, 1995)) for Torbat-e-Heydarieh peridotites, mantle gabbros, plagiogranites and crustal magmatic rocks.

Fig. 13- (A) FeO^{*}/MgO *vs* SiO_2 (Miyashiro, 1974) and (B) Ti *vs* V diagrams (Shervais, 1982) for THO rocks. Data for the Sabzevar ophiolite are from (Moghadam et al., 2014a).

Fig. 14- εHf *vs* εNd for the Torbat-e-Heydarieh magmatic rocks, recalculated at 100 Ma (modified after (Chauvel et al., 2009)). In panel (A), our samples are compared to the MORB and OIB-type lavas, whereas in panel (B), the mixing trend between depleted mantle reservoir and different-types of sediments is shown. Data for Oman plagiogranites are from (Haase et al., 2015) and data from Dehshir ophiolites are from (Moghadam et

al., 2012). MORB and OIB data are from (Chauvel and Blichert-Toft, 2001a; Nowell et al., 1998; Pearce et al., 1999; Woodhead et al., 2001). Mantle array data are after (Vervoort and Blichert-Toft, 1999a).

Fig. 15- Zircon SHRIMP and LA-ICPMS U-Pb data from the Torbat-e-Heydarieh plagiogranite and diabasic-gabbroic dikes.

Fig. 16- (A) Th/Yb *vs* Ta/Yb (Pearce and Peate, 1995) and (B) Ce/Nb *vs* Th/Nb (Sandeman et al., 2006) diagrams for the Torbat-e-Heydarieh magmatic rocks. Hf/Nb *vs* Zr/Nb (C) and Th/Nb *vs* $^{143}Nd/^{144}Nd$ plots (D) (Sorbadere et al., 2013) for THO magmatic rocks, Okinawa Trough, Central Lau basin and Sabzevar ophiolitic igneous rocks, comparing the effect of enrichment and depletion in the mantle sources of these magmas, with respect to the N-MORB source. Pale red field shows bulk mixing between N-MORB and sediment and between N-MORB and fluid and thus represents the slab contribution (modified after (Sorbadere et al., 2013)). Data from the Sabzevar ophiolite are from (Moghadam et al., 2014a). Data from the Lau back-arc basin and the Okinawa Trough are from (Tian et al., 2011) and (Shinjo, 1999) respectively.

Fig. 17- Schematic model showing the generation of the Sabzevar-Torbat-e-Heydarieh ophiolites. (A) Subduction initiation and Neotethys sinking caused strong extension in the region above the sinking lithosphere, leading to seafloor spreading and forming the proto-fore-arc crust. Strong extension in the Iranian continental crust lead to extensional basins opening and nucleation of the STHO back-arc basin. (B) Beginning of true subduction (~100 Ma), and formation of the Urumieh-Dokhtar arc and the STHO back-arc basin.

TABLE CAPTION

Table 1- Provenance of the mantle-crust-lava units of THO.

SUPPLEMENTARY DATA

Supplementary Table 1- Representative compositions of minerals in the Torbat-e-Heydarieh ophiolites.

Supplementary Table 2- Trace elements composition of minerals from THO mantle peridotites and cumulate gabbros.

Supplementary Table 3- Whole rock data of the THO mantle peridotites and gabbros.

Supplementary Table 4- Whole rock analysis of the THO magmatic rocks.

Supplementary Table 5- Whole rock Nd-Hf isotope data for the Torbat-e-Heydarieh ophiolitic rocks.

Supplementary Table 6- SHRIMP U-Pb data for zircon from magmatic rocks of the Torbat-e-Heydarieh ophiolites.

Supplementary Table 7- LA-ICPMS U-Pb data for zircon from magmatic rocks of the Torbat-e-Heydarieh ophiolites.

Supplementary Table 8- Lu-Hf isotope data for zircon from magmatic rocks of the Torbat-e-Heydarieh ophiolites.

ELECTRONIC APPENDIX A

Major element compositions of minerals were analyzed using JEOL wavelength dispersive electron probe X-ray micro-analyzer (JXA 8800R) at Kanazawa University. Accelerating voltage, beam current, and beam diameter for the analyses were 20 kV, 20 nA, and 3 μm, respectively. Representative mineral compositions are reported in Supplementary Table 1.

Trace-element contents of minerals from peridotites and gabbros were analyzed on polished thick-sections in the Geochemical Analysis Unit (GAU) at CCFS/GEMOC, Macquarie University; Sydney, Australia. An Agilent 7700 laser ablation system has been used to analyze trace element abundances in minerals. The Agilent 7700 was coupled with a New Wave UP-266 nm Nd:YAG laser microprobe. Data were collected and processed using the GLITTER software, which allows for the cleanest part of the time-resolved spectrum to be selected, avoiding inclusion phases and host silicate phases. NIST-612 and BCR-2 glasses were used as an external calibration. The trace-element compositions of minerals are reported in Supplementary Table 2.

Major and trace element analyses of pillow lavas, massive lavas, plagiogranites and dikes were carried out using ICP-AES and ICP-MS at CNRS-SARM, Nancy University (France), using BR, DR-N, UB-N, AN-G and GH standards. For major elements, the uncertainty (1 sigma) is better than 2% for concentrations higher than 5 wt.% and better than 5% in the range 0.1-5 wt.%. For trace elements and REEs, the precision is 5% in the range 1-100 ppm and 10% in the range 0.1-1 ppm. The bulk rock major and trace elements analyses for pillow lavas, massive lavas, plagiogranites and dikes are shown in Supplementary Table 4.

Major elements of the Torbat-e-Heydarieh mantle gabbroids and peridotites were analyzed using ICP-AES and ICP-MS at ACME Analytical Laboratories Ltd, Canada. Concentrations of trace elements in Torbat-e-Heydarieh gabbroids and peridotites were determined by Inductively Coupled Plasma Mass Spectroscopy (ICP-MS) using a Thermo Scientific X-Series 2 in the Department of Earth Sciences at the University of Durham, following a standard nitric and hydrofluoric acid digestion (Ottley et al., 2003).

Sample preparation was undertaken in clean air laminar flow hoods. Briefly the procedure is as follows; into a Teflon vial 4ml HF and 1ml HNO_3 (SPA, ROMIL Cambridge) is added to 100 mg of powdered sample, the vial is sealed and left on a hot plate at 150 °C for 48 h. The acid mixture was evaporated to near dryness, the moist residue has 1 ml HNO_3 added and evaporated again to near dryness. 1 ml HNO_3 was again added and evaporated to near dryness. These steps convert insoluble fluoride species into soluble nitrate species. Finally, 2.5 ml HNO_3 was added and diluted to 50 ml after the addition of an internal standard giving a final concentration of 20 ppb Re and Rh. The internal standard was used to compensate for analytical drift and matrix suppression effects. Calibration of the ICP-MS was via international rock standards (BHVO-1, AGV-1, W-2, and NBS688) with the addition of an in-house standard (GP13) (Ottley et al., 2003). These standards and analytical blanks were prepared by the same techniques as for the THO samples. To improve the signal-to-noise threshold for low abundances of incompatible trace elements in ultramafic rocks, instrument dwell times were increased (Ottley et al., 2003). The composition of the reference samples (W-2, AGV-1, BHVO-1, BE-N, NBS688) was analyzed as unknowns during the same analytical runs. For the analyzed elements, reproducibility of these reference samples is generally better than 2% and the measured composition compares favorably with that published information in (Potts et al., 1992). The bulk rock major and trace elements analyses for cumulate gabbroids and peridotites are shown in Supplementary Table 3. Eight whole-rock samples were analyzed for their Nd and Hf isotope compositions (Supplementary Table 5). Chemical separation of Nd and Hf used c. 100 mg of sample powder that was spiked with mixed ^{176}Lu-^{180}Hf and ^{149}Sm-^{150}Nd tracers and subsequently

1181 digested on a hotplate in a 1:1 mixture of concentrated HF-HNO_3 (24 hours, 120°C).
1182 Subsequently, the acid mixture was dried and the samples were digested in a 3:2 mixture
1183 of concentrated HF-HNO_3 in steel-jacketed Parr pressure vessels (3 days, 180°C).
1184 Subsequently, fluorides were decomposed by drying with 1 ml of perchloric acid and
1185 three additional dry-down steps with concentrated HNO_3. The chemical separation of Hf
1186 and Lu from the matrix follows the procedure of (Munker et al., 2001). Samarium and Nd
1187 were separated from the residue after Hf separation, using Bio-Rad AG50W-X8 cation
1188 resin (200-400 mesh) and Ln-Spec resin (Pin and Zalduegui, 1997).
1189 The Nd and Hf isotope compositions as well as Lu-Hf and Sm-Nd concentrations
1190 were determined using a Thermo-Finnigan Neptune multi-collector ICP-MS at the joint
1191 clean lab facilities in Cologne/Bonn. Data was collected in static multi-collection mode.
1192 Values of $^{143}Nd/^{144}Nd$ and $^{176}Hf/^{177}Hf$ were corrected for mass fractionation using the
1193 exponential law and $^{146}Nd/^{144}Nd=0.7219$ and $^{179}Hf/^{177}Hf=0.7325$, respectively. Repeated
1194 analyses of the standards La Jolla Nd and Hf AMES (isotopically identical to JMC-475)
1195 yield mean values of $^{143}Nd/^{144}Nd= 0.511835$ (n=2) and $^{176}Hf/^{177}Hf=0.282156$ (n=18). The
1196 external long-term reproducibility is c. ±40 ppm for Nd and Hf isotopes (2 RSD).
1197 Reported values are given relative to 0.511859 for La Jolla and 0.282160 for Hf AMES.
1198 Procedural blanks were typically below 60 pg for Hf and Nd. The external precision of
1199 the Nd and Hf measurements was further assessed by multiple digestions of six samples
1200 (see Supplementary Table 5). External precision (2 RSD) for the replicates was better
1201 than 30 ppm for $^{143}Nd/^{144}Nd$ and 40 ppm for $^{176}Hf/^{177}Hf$.
1202 In order to have precise ages for the Torbat-e-Heydarieh ophiolite, zircons from
1203 plagiogranites (4 samples) and diabasic (1 sample)- rodingitized gabbroic dike (1 sample)

within the mantle harzburgite were analyzed by SHRIMP at the Korea Basic Science Institute, Ochang, South Korea and LA-ICPMS at Geochemical Analysis Unit (GAU), CCFS/GEMOC, Macquarie University. For SHRIMP analysis, zircon grains were mechanically separated using conventional mineral separation techniques that employed crushing, grinding, sieving, and magnetic separation steps, followed by handpicking of zircons under a binocular microscope. The internal structure of these zircon grains was studied using transmitted and reflected light optical microscopy, and by scanning electron microscope-cathodoluminescence (CL) imaging. Analytical procedures including instrumental set-up, and the acquisition and treatment of data employed in this SHRIMP U-Pb zircon dating study, are outlined in (Compston et al., 1984). For the reduction of raw data and in making the final age calculations, we used the programs SQUID and Isoplot/Ex (Ludwig, 2003, 2009). The SHRIMP U-Pb zircon analytical data are summarized in Supplementary Table 6.

For LA-ICPMS analysis, zircons were separated following electrostatic disaggregation (selFrag) of the rock sample, then using standard gravimetric and magnetic techniques; grains were picked under a binocular microscope and mounted in epoxy discs for analysis. All grains were imaged by CL and BSE to provide maps to guide the choice of analytical spots. Zircon U-Pb ages were obtained using a 193 nm ArF EXCIMER laser with an Agilent 7700 ICP-MS system. Detailed method descriptions have been given by (Jackson et al., 2004). The ablation conditions included beam size (30 µm), pulse rate (5Hz) and energy density (7.59 J/cm^2). Analytical runs comprised 16 analyses with 12 analyses of unknowns bracketed by two analyses of a standard zircon GJ-1 at the beginning and end of each run, using the established TIMS values

($^{207}Pb/^{206}Pb$ age= 608.5 Ma, (Jackson et al., 2004)). U-Pb ages were calculated from the raw signal data using the on-line software package GLITTER (Griffin et al., 2008). U-Pb age data were subjected to a common-lead correction, except for those with common-Pb concentrations lower than detection limits. The results were processed using the ISOPLOT program of (Ludwig, 2003). The external standards, zircons 91500 and Mud Tank, gave mean $^{206}Pb/^{238}U$ ages of 1063.5±1.8 Ma (MSWD=1.3) and 731.1±1.2 Ma (MSWD=0.77), respectively, which are similar to the recommended $^{206}Pb/^{238}U$ ages of 1062.4±0.4 Ma and 731.9±3.4 Ma respectively (Chang et al., 2006; Woodhead and Hergt, 2005; Yuan et al., 2008). LA-ICPMS U-Pb zircon analytical data is summarized in Supplementary Table 7.

In situ zircon Lu-Hf isotopic analyses were performed using a Nu Plasma multi-collector ICP-MS, coupled to a Photon Machines 193 nm ArF excimer laser system at CCFS (Macquarie University). The analyses were carried out using the Nu Plasma time-resolved analysis software. The methods, including calibration and correction for mass bias, are described by (Griffin et al., 2004; Griffin et al., 2000). The ablation spots (55 µm) for the Hf isotope analyses were situated close to the U-Pb analysis positions on each grain. The accuracy of the Yb and Lu corrections during LA-MC-ICPMS analysis of zircon has been demonstrated by repeated analysis of standard zircons with a range in $^{176}Yb/^{177}Hf$ and $^{176}Lu/^{177}Hf$. Four secondary standards (Mud Tank and Temora) were analyzed between every ten unknowns to check instrumental stability. $^{176}Hf/^{177}Hf$ ratios of the Mud Tank zircon gave an average of 0.2825355±0.0000041 (2SD; n=122); those of Temora gave 0.2826971±0.0000078 (2SD; n=42). These values are identical to those recommended for Mud Tank (0.282507±0.000003) and Temora (0.282693±0.000052)

(Fisher et al., 2014). The isobaric interferences of ^{176}Lu and ^{176}Yb on ^{176}Hf are very limited, because of the extremely low ratios of Lu/Hf and Yb/Hf in the measured standard zircons. The interference of ^{176}Yb on ^{176}Hf was corrected by measuring the interference-free ^{172}Yb isotope and using $^{176}Yb/^{172}Yb$ to calculate $^{176}Yb/^{177}Hf$. The appropriate value of $^{176}Yb/^{172}Yb$ was determined by successive spiking the JMC475 Hf standard (1 ppm solution) with Yb, and iteratively finding the value of $^{176}Yb/^{172}Yb$ required to yield the value of $^{176}Hf/^{177}Hf$ obtained on the pure Hf solution (Griffin et al., 2004; Griffin et al., 2000). Zircon Hf isotope data are presented in Supplementary Table 8.

REFERENCES

Agard, P., Jolivet, L., Vrielynck, B., Burov, E., and Monie, P., 2007, Plate acceleration: The obduction trigger?: Earth and Planetary Science Letters, v. 258, no. 3-4, p. 428-441.

Alaminia, Z., Karimpour, M. H., Homam, S. M., and Finger, F., 2013, The magmatic record in the Arghash region (northeast Iran) and tectonic implications: International Journal of Earth Sciences, v. 102, no. 6, p. 1603-1625.

Aldanmaz, E., 2012, Trace element geochemistry of primary mantle minerals in spinel-peridotites from polygenetic MOR-SSZ suites of SW Turkey: constraints from an LA-ICP-MS study and implications for mantle metasomatism: Geological Journal, v. 47, no. 1, p. 59-76.

Anenburg, M., Katzir, Y., Rhede, D., Jons, N., and Bach, W., 2015, Rare earth element evolution and migration in plagiogranites: a record preserved in epidote and allanite of the Troodos ophiolite: Contributions to Mineralogy and Petrology, v. 169, no. 3.

1274 Arai, S., Kadoshima, K., and Morishita, T., 2006, Widespread arc-related melting in the
1275 mantle section of the northern Oman ophiolite as inferred from detrital chromian
1276 spinels: Journal of the Geological Society, v. 163, p. 869-879.

1277 Baes, M., Govers, R., and Wortel, R., 2011, Subduction initiation along the inherited
1278 weakness zone at the edge of a slab: Insights from numerical models: Geophysical
1279 Journal International, v. 184, no. 3, p. 991-1008.

1280 Bagci, U., Parlak, O., and Hock, V., 2005, Whole-rock and mineral chemistry of cumulates
1281 from the Kizildag (Hatay) ophiolite (Turkey): clues for multiple magma generation
1282 during crustal accretion in the southern Neotethyan ocean: Mineralogical
1283 Magazine, v. 69, no. 1, p. 53-76.

1284 Bazylev, B. A., Popevic, A., Karamata, S., Kononkova, N. N., Simakin, S. G., Olujic, J.,
1285 Vujnovic, L., and Memovic, E., 2009, Mantle peridotites from the Dinaridic
1286 ophiolite belt and the Vardar zone western belt, central Balkan: A petrological
1287 comparison: Lithos, v. 108, no. 1-4, p. 37-71.

1288 Bedard, E., Hebert, R., Guilmette, C., Lesage, G., Wang, C. S., and Dostal, J., 2009,
1289 Petrology and geochemistry of the Saga and Sangsang ophiolitic massifs, Yarlung
1290 Zangbo Suture Zone, Southern Tibet: Evidence for an arc-back-arc origin: Lithos,
1291 v. 113, no. 1-2, p. 48-67.

1292 Berberian, M., 1983, The southern Caspian: a compressional depression floored by a
1293 trapped, modified oceanic crust: Canadian Journal of Earth Sciences, v. 20, no. 2,
1294 p. 163-183.

1295 Bizimis, M., Salters, V. J., and Bonatti, E., 2000, Trace and REE content of clinopyroxenes
1296 from supra-subduction zone peridotites. Implications for melting and enrichment
1297 processes in island arcs: Chemical Geology, v. 165, no. 1-2, p. 67-85.

1298 Bonev, N., and Stampfli, G., 2009, Gabbro, plagiogranite and associated dykes in the
1299 supra-subduction zone Evros Ophiolites, NE Greece: Geological Magazine, v. 146,
1300 no. 1, p. 72-91.

1301 Bröcker, M., Fotoohi Rad, G. F., Burgess, R., Theunissen, S., Paderin, I., Rodionov, N.,
1302 and Salimi, Z., 2013, New age constraints for the geodynamic evolution of the
1303 Sistan Suture Zone, eastern Iran: Lithos, v. 170, p. 17-34.

1304 Burns, L. E., 1985, The Border Ranges Ultramafic and Mafic Complex, South-Central
1305 Alaska - Cumulate Fractionates of Island-Arc Volcanics: Canadian Journal of Earth
1306 Sciences, v. 22, no. 7, p. 1020-1038.

1307 Burtman, V., 1994, Meso-Tethyan oceanic sutures and their deformation: Tectonophysics,
1308 v. 234, no. 4, p. 305-327.

1309 Cawood, P. A., 1989, Acadian Remobilization of a Taconian Ophiolite, Hare Bay
1310 Allochthon, Northwestern Newfoundland: Geology, v. 17, no. 3, p. 257-260.

1311 Chang, Z. S., Vervoort, J. D., McClelland, W. C., and Knaack, C., 2006, U-Pb dating of
1312 zircon by LA-ICP-MS: Geochemistry Geophysics Geosystems, v. 7.

1313 Chauvel, C., and Blichert-Toft, J., 2001a, A hafnium isotope and trace element perspective
1314 on melting of the depleted mantle: Earth and Planetary Science Letters, v. 190, no.
1315 3, p. 137-151.

1316 Chauvel, C., and Blichert-Toft, J., 2001b, A hafnium isotope and trace element perspective
1317 on melting of the depleted mantle: Earth and Planetary Science Letters, v. 190, no.
1318 3-4, p. 137-151.

1319 Chauvel, C., Marini, J. C., Plank, T., and Ludden, J. N., 2009, Hf-Nd input flux in the Izu-
1320 Mariana subduction zone and recycling of subducted material in the mantle:
1321 Geochemistry Geophysics Geosystems, v. 10, no. 1, p. n/a-n/a.

1322 Chiu, H. Y., Chung, S. L., Zarrinkoub, M. H., Mohammadi, S. S., Khatib, M. M., and
1323 Iizuka, Y., 2013, Zircon U-Pb age constraints from Iran on the magmatic evolution
1324 related to Neotethyan subduction and Zagros orogeny: Lithos, v. 162, p. 70-87.

1325 Coleman, R. G., 1977, Ophiolites, New York, Springer-Verlag, 220 p.:

Compston, W., Williams, I., and Meyer, C., 1984, U‐Pb geochronology of zircons from lunar breccia 73217 using a sensitive high mass‐resolution ion microprobe: Journal of Geophysical Research: Solid Earth, v. 89, no. S02.

Dercourt, J., Zonenshain, L. P., Ricou, L. E., Kazmin, V. G., Lepichon, X., Knipper, A. L., Grandjacquet, C., Sbortshikov, I. M., Geyssant, J., Lepvrier, C., Pechersky, D. H., Boulin, J., Sibuet, J. C., Savostin, L. A., Sorokhtin, O., Westphal, M., Bazhenov, M. L., Lauer, J. P., and Bijuduval, B., 1986, Geological Evolution of the Tethys Belt from the Atlantic to the Pamirs since the Lias: Tectonophysics, v. 123, no. 1-4, p. 241-315.

Dick, H. J. B., and Bullen, T., 1984, Chromian Spinel as a Petrogenetic Indicator in Abyssal and Alpine-Type Peridotites and Spatially Associated Lavas: Contributions to Mineralogy and Petrology, v. 86, no. 1, p. 54-76.

Dilek, Y., and Flower, M. F. J., 2003, Arc-trench rollback and forearc accretion: 2. A model template for ophiolites in Albania, Cyprus, and Oman: Ophiolites in Earth History, v. 218, p. 43-68.

Dilek, Y., and Furnes, H., 2009, Structure and geochemistry of Tethyan ophiolites and their petrogenesis in subduction rollback systems: Lithos, v. 113, no. 1-2, p. 1-20.

-, 2011, Ophiolite genesis and global tectonics: Geochemical and tectonic fingerprinting of ancient oceanic lithosphere: Geological Society of America Bulletin, v. 123, no. 3-4, p. 387-411.

Dilek, Y., Furnes, H., and Shallo, M., 2007, Suprasubduction zone ophiolite formation along the periphery of Mesozoic Gondwana: Gondwana Research, v. 11, no. 4, p. 453-475.

Dilek, Y., and Thy, P., 2006, Age and petrogenesis of plagiogranite intrusions in the Ankara melange, central Turkey: Island Arc, v. 15, no. 1, p. 44-57.

1351 Fisher, C. M., Vervoort, J. D., and DuFrane, S. A., 2014, Accurate Hf isotope
1352 determinations of complex zircons using the "laser ablation split stream" method:
1353 Geochemistry Geophysics Geosystems, v. 15, no. 1, p. 121-139.

1354 Furnes, H., de Wit, M., and Dilek, Y., 2014, Four billion years of ophiolites reveal secular
1355 trends in oceanic crust formation: Geoscience Frontiers, v. 5, no. 4, p. 571-603.

1356 Gerya, T., 2011, Intra-oceanic Subduction Zones, *in* Brown D., R., P.D., ed., Arc-Continent
1357 Collision, Frontiers: Berlin, Springer-Verlag, p. 23-53.

1358 Ghasemi, A., and Manesh, S. M. T., 2015, Geochemistry and petrogenesis of Ghohroud
1359 Igneous Complex (Urumieh-Dokhtar zone): evidence for Neotethyan subduction
1360 during the Neogene: Arabian Journal of Geosciences, v. 8, no. 11, p. 9599-9623.

1361 Ghazi, A., Hassanipak, A., and Wallace, K., 1997, Geochemistry, petrology and geology
1362 of the Sabzevar ophiolite, Northeastern Iran: Implication on Tethyan tectonics:
1363 Geological Society of America, v. 29.

1364 Ghazi, J. M., Moazzen, M., Rahgoshay, M., and Moghadam, H. S., 2010, Mineral chemical
1365 composition and geodynamic significance of peridotites from Nain ophiolite,
1366 central Iran: Journal of Geodynamics, v. 49, no. 5, p. 261-270.

1367 Ghorbani, M. R., Graham, I. T., and Ghaderi, M., 2014, Oligocene-Miocene geodynamic
1368 evolution of the central part of Urumieh-Dokhtar Arc of Iran: International Geology
1369 Review, v. 56, no. 8, p. 1039-1050.

1370 Gong, X. H., Shi, R. D., Griffin, W. L., Huang, Q. S., Xiong, Q., Chen, S. S., Zhang, M.,
1371 and O'Reilly, S. Y., 2016, Recycling of ancient subduction-modified mantle
1372 domains in the Purang ophiolite (southwestern Tibet): Lithos, v. 262, p. 11-26.

1373 Griffin, W., Powell, W., Pearson, N., and O'reilly, S., 2008, GLITTER: data reduction
1374 software for laser ablation ICP-MS: Laser Ablation-ICP-MS in the earth sciences.
1375 Mineralogical association of Canada short course series, v. 40, p. 204-207.

1376 Griffin, W. L., Belousova, E. A., Shee, S. R., Pearson, N. J., and O'Reilly, S. Y., 2004,
1377 Archean crustal evolution in the northern Yilgam Craton: U-Pb and Hf-isotope
1378 evidence from detrital zircons: Precambrian Research, v. 131, no. 3-4, p. 231-282.

1379 Griffin, W. L., Pearson, N. J., Belousova, E., Jackson, S. E., van Achterbergh, E., O'Reilly,
1380 S. Y., and Shee, S. R., 2000, The Hf isotope composition of cratonic mantle: LAM-
1381 MC-ICPMS analysis of zircon megacrysts in kimberlites: Geochimica Et
1382 Cosmochimica Acta, v. 64, no. 1, p. 133-147.

1383 Guilmette, C., Smit, M. A., van Hinsbergen, D. J. J., Gürer, D., Corfu, F., Charette, B.,
1384 Maffione, M., Rabeau, O., and Savard, D., 2018, Forced subduction initiation
1385 recorded in the sole and crust of the Semail Ophiolite of Oman: Nature Geoscience,
1386 v. 11, p. 688–695.

1387 Gurnis, M., Hall, C., and Lavier, L., 2004, Evolving force balance during incipient
1388 subduction: Geochemistry Geophysics Geosystems, v. 5.

1389 Haase, K. M., Freund, S., Koepke, J., Hauff, F., and Erdmann, M., 2015, Melts of
1390 sediments in the mantle wedge of the Oman ophiolite: Geology, v. 43, no. 4, p. 275-
1391 278.

1392 Hall, C. E., Gurnis, M., Sdrolias, M., Lavier, L. L., and Muller, R. D., 2003, Catastrophic
1393 initiation of subduction following forced convergence across fracture zones: Earth
1394 and Planetary Science Letters, v. 212, no. 1-2, p. 15-30.

1395 Hamada, M., and Fujii, T., 2008, Experimental constraints on the effects of pressure and
1396 H2O on the fractional crystallization of high-Mg island arc basalt: Contributions to
1397 Mineralogy and Petrology, v. 155, no. 6, p. 767-790.

1398 Hébert, R., Bezard, R., Guilmette, C., Dostal, J., Wang, C. S., and Liu, Z. F., 2012, The
1399 Indus–Yarlung Zangbo ophiolites from Nanga Parbat to Namche Barwa syntaxes,
1400 southern Tibet: First synthesis of petrology, geochemistry, and geochronology with
1401 incidences on geodynamic reconstructions of Neo-Tethys: Gondwana Research, v.
1402 22, no. 2, p. 377-397.

1403 Hickey-Vargas, R., Yogodzinski, G., Ishizuka, O., McCarthy, A., Bizimis, M., Kusano, Y.,
1404 Savov, I., and Arculus, R., 2018, Origin of depleted basalts during subduction
1405 initiation and early development of the Izu-Bonin-Mariana Island arc: Evidence
1406 from IODP Expedition 351 Site U1438, Amami-Sankaku Basin: Geochimica et
1407 Cosmochimica Acta.

1408 Hirahara, Y., Kimura, J. I., Senda, R., Miyazaki, T., Kawabata, H., Takahashi, T., Chang,
1409 Q., Vaglarov, B. S., Sato, T., and Kodaira, S., 2015, Geochemical variations in
1410 Japan Sea back‐arc basin basalts formed by high‐temperature adiabatic melting
1411 of mantle metasomatized by sediment subduction components: Geochemistry,
1412 Geophysics, Geosystems, v. 16, no. 5, p. 1324-1347.

1413 Honarmand, M., Omran, N. R., Neubauer, F., Emami, M. H., Nabatian, G., Liu, X. M.,
1414 Dong, Y. P., von Quadt, A., and Chen, B., 2014, Laser-ICP-MS U-Pb zircon ages
1415 and geochemical and Sr-Nd-Pb isotopic compositions of the Niyasar plutonic
1416 complex, Iran: constraints on petrogenesis and tectonic evolution: International
1417 Geology Review, v. 56, no. 1, p. 104-132.

1418 Hosseini, M. R., Hassanzadeh, J., Alirezaei, S., Sun, W. D., and Li, C. Y., 2017, Age
1419 revision of the Neotethyan arc migration into the southeast Urumieh-Dokhtar belt
1420 of Iran: Geochemistry and U-Pb zircon geochronology: Lithos, v. 284, p. 296-309.

1421 Ishikawa, T., Nagaishi, K., and Umino, S., 2002, Boninitic volcanism in the Oman
1422 ophiolite: Implications for thermal condition during transition from spreading ridge
1423 to arc: Geology, v. 30, no. 10, p. 899-902.

1424 Ishizuka, O., Tani, K., and Reagan, M. K., 2014, Izu-Bonin-Mariana forearc crust as a
1425 modern ophiolite analogue: Elements, v. 10, no. 2, p. 115-120.

1426 Jackson, S. E., Pearson, N. J., Griffin, W. L., and Belousova, E. A., 2004, The application
1427 of laser ablation-inductively coupled plasma-mass spectrometry to in situ U-Pb
1428 zircon geochronology: Chemical Geology, v. 211, no. 1-2, p. 47-69.

1429 Johnson, K., Dick, H. J., and Shimizu, N., 1990, Melting in the oceanic upper mantle: an
1430 ion microprobe study of diopsides in abyssal peridotites: Journal of Geophysical
1431 Research: Solid Earth, v. 95, no. B3, p. 2661-2678.

1432 Kazemi, Z., Ghasemi, H., Tilhac, R., Griffin, W., Moghadam, H. S., O'Reilly, S., and
1433 Mousivand, F., 2019, Late Cretaceous subduction-related magmatism on the
1434 southern edge of Sabzevar basin, NE Iran: Journal of the Geological Society, p.
1435 jgs2018-2076.

1436 Kazmin, V. G., Sbortshikov, I. M., Ricou, L. E., Zonenshain, L. P., Boulin, J., and Knipper,
1437 A. L., 1986, Volcanic Belts as Markers of the Mesozoic-Cenozoic Active Margin
1438 of Eurasia: Tectonophysics, v. 123, no. 1-4, p. 123-152.

1439 Kelley, K. A., Kingsley, R., and Schilling, J. G., 2013, Composition of plume‐influenced
1440 mid‐ocean ridge lavas and glasses from the Mid‐Atlantic Ridge, East Pacific
1441 Rise, Galápagos Spreading Center, and Gulf of Aden: Geochemistry, Geophysics,
1442 Geosystems, v. 14, no. 1, p. 223-242.

1443 Kessel, R., Schmidt, M. W., Ulmer, P., and Pettke, T., 2005, Trace element signature of
1444 subduction-zone fluids, melts and supercritical liquids at 120-180 km depth:
1445 Nature, v. 437, no. 7059, p. 724-727.

1446 Khalatbari-Jafari, M., Juteau, T., Bellon, H., Whitechurch, H., Cotten, J., and Emami, H.,
1447 2004, New geological, geochronological and geochemical investigations on the
1448 Khoy ophiolites and related formations, NW Iran: Journal of Asian Earth Sciences,
1449 v. 23, no. 4, p. 507-535.

1450 Khedr, M. Z., and Arai, S., 2009, Geochemistry of metasomatized peridotites above
1451 subducting slab: a case study of hydrous metaperidotites from Happo-O'ne
1452 complex, central Japan: Journal of Mineralogical and Petrological Sciences, v. 104,
1453 no. 5, p. 313-318.

1454 Kimura, J.-I., and Sano, S., 2012, Reactive melt flow as the origin of residual mantle
1455 lithologies and basalt chemistries in mid-ocean ridges: Implications from the Red
1456 Hills peridotite, New Zealand: Journal of Petrology, v. 53, no. 8, p. 1637-1671.

1457 Kimura, J.-I., Stern, R. J., and Yoshida, T., 2005, Reinitiation of subduction and magmatic
1458 responses in SW Japan during Neogene time: Geological Society of America
1459 Bulletin, v. 117, no. 7-8, p. 969-986.

1460 Lagabrielle, Y., Guivel, C., Maury, R. C., Bourgois, J., Fourcade, S., and Martin, H., 2000,
1461 Magmatic-tectonic effects of high thermal regime at the site of active ridge
1462 subduction: the Chile Triple Junction model: Tectonophysics, v. 326, no. 3-4, p.
1463 255-268.

1464 Leake, B. E., Woolley, A. R., Arps, C. E. S., Birch, W. D., Gilbert, M. C., Grice, J. D.,
1465 Hawthorne, F. C., Kato, A., Kisch, H. J., Krivovichev, V. G., Linthout, K., Laird,
1466 J., Mandarino, J., Maresch, W. V., Nickel, E. H., Rock, N. M. S., Schumacher, J.
1467 C., Smith, D. C., Stephenson, N. C. N., Ungaretti, L., Whittaker, E. J. W., and
1468 Youzhi, G., 1997, Nomenclature of amphiboles: Report of the Subcommittee on
1469 Amphiboles of the International Mineralogical Association Commission on New
1470 Minerals and Mineral Names: Mineralogical Magazine, v. 61, no. 2, p. 295-321.

1471 Long, M. D., and Wirth, E. A., 2013, Mantle flow in subduction systems: The mantle
1472 wedge flow field and implications for wedge processes: Journal of Geophysical
1473 Research: Solid Earth, v. 118, no. 2, p. 583-606.

1474 Ludwig, K. R., 2003, User's Manual for Isoplot 3.00: A Geochronological Toolkit for
1475 Microsoft Excel.

1476 -, 2009, SQUID 2: A User's manual: Berkeley Geochronology Center Special Publications
1477 4.

1478 Maffione, M., van Hinsbergen, D. J. J., de Gelder, G. I. N. O., van der Goes, F. C., and
1479 Morris, A., 2017, Kinematics of Late Cretaceous subduction initiation in the Neo-

Tethys Ocean reconstructed from ophiolites of Turkey, Cyprus, and Syria: Journal of Geophysical Research-Solid Earth, v. 122, no. 5, p. 3953-3976.

Maghfouri, S., Rastad, E., Mousivand, F., Lin, Y., and Zaw, K., 2016, Geology, ore facies and sulfur isotopes geochemistry of the Nudeh Besshi-type volcanogenic massive sulfide deposit, southwest Sabzevar basin, Iran: Journal of Asian Earth Sciences, v. 125, p. 1-21.

Malekpour-Alamdari, A., Axen, G., Heizler, M., and Hassanzadeh, J., 2017, Large-magnitude continental extension in the northeastern Iranian Plateau: Insight from K-feldspar 40Ar/39Ar thermochronology from the Shotor Kuh–Biarjmand metamorphic core complex: Geosphere, v. 13, no. 4, p. 1207-1233.

Mcdonough, W. F., and Sun, S. S., 1995, The Composition of the Earth: Chemical Geology, v. 120, no. 3-4, p. 223-253.

Miyashiro, A., 1974, Volcanic rock series in island arcs and active continental margins: American journal of science, v. 274, no. 4, p. 321-355.

Moghadam, H. S., Brocker, M., Griffin, W. L., Li, X. H., Chen, R. X., and O'Reilly, S. Y., 2017a, Subduction, high-P metamorphism, and collision fingerprints in South Iran: Constraints from zircon U-Pb and mica Rb-Sr geochronology: Geochemistry Geophysics Geosystems, v. 18, no. 1, p. 306-332.

Moghadam, H. S., Corfu, F., Chiaradia, M., Stern, R. J., and Ghorbani, G., 2014a, Sabzevar Ophiolite, NE Iran: Progress from embryonic oceanic lithosphere into magmatic arc constrained by new isotopic and geochemical data: Lithos.

Moghadam, H. S., Corfu, F., Chiaradia, M., Stern, R. J., and Ghorbani, G., 2014b, Sabzevar Ophiolite, NE Iran: Progress from embryonic oceanic lithosphere into magmatic arc constrained by new isotopic and geochemical data: Lithos, v. 210, p. 224-241.

Moghadam, H. S., Corfu, F., and Stern, R. J., 2013, U-Pb zircon ages of Late Cretaceous Nain-Dehshir ophiolites, central Iran: Journal of the Geological Society, v. 170, no. 1, p. 175-184.

1507 Moghadam, H. S., Khedr, M. Z., Arai, S., Stern, R. J., Ghorbani, G., Tamura, A., and
1508 Ottley, C. J., 2015, Arc-related harzburgite-dunite-chromitite complexes in the
1509 mantle section of the Sabzevar ophiolite, Iran: A model for formation of podiform
1510 chromitites: Gondwana Research, v. 27, no. 2, p. 575-593.

1511 Moghadam, H. S., Li, X.-H., Santos, J. F., Stern, R. J., Griffin, W. L., Ghorbani, G., and
1512 Sarebani, N., 2017b, Neoproterozoic magmatic flare-up along the N. margin of
1513 Gondwana: The Taknar complex, NE Iran: Earth and Planetary Science Letters, v.
1514 474, p. 83-96.

1515 Moghadam, H. S., and Stern, R. J., 2011, Geodynamic evolution of Upper Cretaceous
1516 Zagros ophiolites: formation of oceanic lithosphere above a nascent subduction
1517 zone: Geological Magazine, v. 148, no. 5-6, p. 762-801.

1518 -, 2015, Ophiolites of Iran: Keys to understanding the tectonic evolution of SW Asia: (II)
1519 Mesozoic ophiolites: Journal of Asian Earth Sciences, v. 100, p. 31-59.

1520 Moghadam, H. S., Stern, R. J., Kimura, J. I., Hirahara, Y., Senda, R., and Miyazaki, T.,
1521 2012, Hf-Nd isotope constraints on the origin of Dehshir Ophiolite, Central Iran:
1522 Island Arc, v. 21, no. 3, p. 202-214.

1523 Moghadam, H. S., Stern, R. J., and Rahgoshay, M., 2010, The Dehshir ophiolite (central
1524 Iran): Geochemical constraints on the origin and evolution of the Inner Zagros
1525 ophiolite belt: Geological Society of America Bulletin, v. 122, no. 9-10, p. 1516-
1526 1547.

1527 Monsef, I., Monsef, R., Mata, J., Zhang, Z., Pirouz, M., Rezaeian, M., Esmaeili, R., and
1528 Xiao, W., 2018, Evidence for an early-MORB to fore-arc evolution within the
1529 Zagros suture zone: Constraints from zircon U-Pb geochronology and
1530 geochemistry of the Neyriz ophiolite (South Iran): Gondwana Research.

1531 Monsef, I., Rahgoshay, M., Mohajjel, M., and Moghadam, H. S., 2010, Peridotites from
1532 the Khoy Ophiolitic Complex, NW Iran: Evidence of mantle dynamics in a supra-

1533 subduction-zone context: Journal of Asian Earth Sciences, v. 38, no. 3-4, p. 105-
1534 120.

1535 Moritz, R., and Ghazban, F., 1996, Geological and fluid inclusion studies in the Muteh
1536 gold district, Sanandaj-Sirjan zone, Isfahan Province, Iran: Schweizerische
1537 Mineralogische Und Petrographische Mitteilungen, v. 76, no. 1, p. 85-89.

1538 Moritz, R., Ghazban, F., and Singer, B. S., 2006, Eocene gold ore formation at Muteh,
1539 Sanandaj-Sirjan tectonic zone, western Iran: A result of late-stage extension and
1540 exhumation of metamorphic basement rocks within the Zagros orogen: Economic
1541 Geology, v. 101, no. 8, p. 1497-1524.

1542 Munker, C., Weyer, S., Scherer, E., and Mezger, K., 2001, Separation of high field strength
1543 elements (Nb, Ta, Zr, Hf) and Lu from rock samples for MC-ICPMS
1544 measurements: Geochemistry, Geophysics, Geosystems, v. 2.

1545 Nasrabady, M., Rossetti, F., Theye, T., and Vignaroli, G., 2011, Metamorphic history and
1546 geodynamic significance of the Early Cretaceous Sabzevar granulites (Sabzevar
1547 structural zone, NE Iran): Solid Earth, v. 2, no. 2, p. 219-243.

1548 Nicolas, A., 1989, Structure of Ophiolites and Dynamics of Oceanic Lithosphere,
1549 Dordrecht, the Netherlands, Kluwer Academic Publishers, 367 p.:

1550 Nowell, G., Kempton, P., Noble, S., Fitton, J., Saunders, A., Mahoney, J., and Taylor, R.,
1551 1998, High precision Hf isotope measurements of MORB and OIB by thermal
1552 ionisation mass spectrometry: insights into the depleted mantle: Chemical Geology,
1553 v. 149, no. 3, p. 211-233.

1554 Ohara, Y., Stern, R. J., Ishii, T., Yurimoto, H., and Yamazaki, T., 2002, Peridotites from
1555 the Mariana Trough: first look at the mantle beneath an active back-arc basin:
1556 Contributions to Mineralogy and Petrology, v. 143, no. 1, p. 1-18.

1557 Omidvar, M., Safari, A., Vaziri-Moghaddam, H., and Ghalavand, H., 2018, Foraminiferal
1558 biostratigraphy of Upper Cretaceous (Campanian–Maastrichtian) sequences in the

1559 Peri-Tethys basin; Moghan area, NW Iran: Journal of African Earth Sciences, v.
1560 140, p. 94-113.

1561 Omrani, H., Moazzen, M., Oberhansli, R., Altenberger, U., and Lange, M., 2013, The
1562 Sabzevar blueschists of the North-Central Iranian micro-continent as remnants of
1563 the Neotethys-related oceanic crust subduction: International Journal of Earth
1564 Sciences, v. 102, no. 5, p. 1491-1512.

1565 Osozawa, S., Shinjo, R., Lo, C. H., Jahn, B. M., Hoang, N., Sasaki, M., Ishikawa, K., Kano,
1566 H., Hoshi, H., Xenophontos, C., and Wakabayashi, J., 2012, Geochemistry and
1567 geochronology of the Troodos ophiolite: An SSZ ophiolite generated by subduction
1568 initiation and an extended episode of ridge subduction?: Lithosphere, v. 4, no. 6, p.
1569 497-510.

1570 Ottley, C., Pearson, D., and Irvine, G., 2003, A routine method for the dissolution of
1571 geological samples for the analysis of REE and trace elements via ICP-MS: Plasma
1572 source mass spectrometry: Applications and emerging technologies, no. 288, p.
1573 221.

1574 Pearce, J., Kempton, P., Nowell, G., and Noble, S., 1999, Hf-Nd element and isotope
1575 perspective on the nature and provenance of mantle and subduction components in
1576 Western Pacific arc-basin systems: Journal of Petrology, v. 40, no. 11, p. 1579-
1577 1611.

1578 Pearce, J. A., 2008, Geochemical fingerprinting of oceanic basalts with applications to
1579 ophiolite classification and the search for Archean oceanic crust: Lithos, v. 100, no.
1580 1-4, p. 14-48.

1581 Pearce, J. A., Barker, P. F., Edwards, S. J., Parkinson, I. J., and Leat, P. T., 2000a,
1582 Geochemistry and tectonic significance of peridotites from the South Sandwich arc-
1583 basin system, South Atlantic: Contributions to Mineralogy and Petrology, v. 139,
1584 no. 1, p. 36-53.

1585 Pearce, J. A., Barker, P. F., Edwards, S. J., Parkinson, I. J., and Leat, P. T., 2000b,
1586 Geochemistry and tectonic significance of peridotites from the South Sandwich arc-
1587 basin system, South Atlantic: Contributions to Mineralogy and Petrology, v. 139,
1588 p. 36-53.

1589 Pearce, J. A., Harris, N. B. W., and Tindle, A. G., 1984, Trace-Element Discrimination
1590 Diagrams for the Tectonic Interpretation of Granitic-Rocks: Journal of Petrology,
1591 v. 25, no. 4, p. 956-983.

1592 Pearce, J. A., and Peate, D. W., 1995, Tectonic Implications of the Composition of
1593 Volcanic Arc Magmas: Annual Review of Earth and Planetary Sciences, v. 23, p.
1594 251-285.

1595 Pearce, J. A., and Robinson, P. T., 2010, The Troodos ophiolitic complex probably formed
1596 in a subduction initiation, slab edge setting: Gondwana Research, v. 18, no. 1, p.
1597 60-81.

1598 Peate, D. W., and Pearce, J. A., 1998, Causes of spatial compositional variations in Mariana
1599 arc lavas: Trace element evidence: Island Arc, v. 7, no. 3, p. 479-495.

1600 Pin, C., and Zalduegui, J. F. S., 1997, Sequential separation of light rare-earth elements,
1601 thorium and uranium by miniaturized extraction chromatography: Application to
1602 isotopic analyses of silicate rocks: Analytica Chimica Acta, v. 339, p. 79-89.

1603 Pirnia, T., Arai, S., Tamura, A., Ishimaru, S., and Torabi, G., 2014, Sr enrichment in mantle
1604 pyroxenes as a result of plagioclase alteration in lherzolite: Lithos, v. 196, p. 198-
1605 212.

1606 Potts, P. J., Tindle, A. G., and Webb, P., 1992, Geochemical reference material
1607 compositions: rocks, minerals, sediments, soils, carbonates, refractories & ores
1608 used in research & industry, Taylor & Francis.

1609 Reagan, M. K., Ishizuka, O., Stern, R. J., Kelley, K. A., Ohara, Y., Blichert-Toft, J.,
1610 Bloomer, S. H., Cash, J., Fryer, P., Hanan, B. B., Hickey-Vargas, R., Ishii, T.,
1611 Kimura, J. I., Peate, D. W., Rowe, M. C., and Woods, M., 2010, Fore-arc basalts

and subduction initiation in the Izu-Bonin-Mariana system: Geochemistry Geophysics Geosystems, v. 11.

Robinson, P. T., Trumbull, R. B., Schmitt, A., Yang, J. S., Li, J. W., Zhou, M. F., Erzinger, J., Dare, S., and Xiong, F. H., 2015, The origin and significance of crustal minerals in ophiolitic chromitites and peridotites: Gondwana Research, v. 27, no. 2, p. 486-506.

Ross, K., and Elthon, D., 1993, Cumulates from strongly depleted mid-ocean-ridge basalt: Nature, v. 365, no. 6449, p. 826.

Rossetti, F., Nasrabady, M., Theye, T., Gerdes, A., Monie, P., Lucci, F., and Vignaroli, G., 2014, Adakite differentiation and emplacement in a subduction channel: The late Paleocene Sabzevar magmatism (NE Iran): Geological Society of America Bulletin, v. 126, no. 3-4, p. 317-343.

Rossetti, F., Nasrabady, M., Vignaroli, G., Theye, T., Gerdes, A., Razavi, M. H., and Vaziri, H. M., 2010, Early Cretaceous migmatitic mafic granulites from the Sabzevar range (NE Iran): implications for the closure of the Mesozoic peri-Tethyan oceans in central Iran: Terra Nova, v. 22, no. 1, p. 26-34.

Saccani, E., Allahyari, K., Beccaluva, L., and Bianchini, G., 2013, Geochemistry and petrology of the Kermanshah ophiolites (Iran): Implication for the interaction between passive rifting, oceanic accretion, and OIB-type components in the Southern Neo-Tethys Ocean: Gondwana Research, v. 24, no. 1, p. 392-411.

Saccani, E., Bortolotti, V., Marroni, M., Pandolfi, L., Photiades, A., and Principi, G., 2008, The Jurassic Association of Backarc Basin Ophiolites and Calc-Alkaline Volcanics in the Guevgueli Complex (Northern Greece): Implication for the Evolution of the Vardar Zone: Ofioliti, v. 33, no. 2, p. 209-227.

Sandeman, H. A., Hanmer, S., Tella, S., Armitage, A. A., Davis, W. J., and Ryan, J. J., 2006, Petrogenesis of Neoarchaean volcanic rocks of the MacQuoid supracrustal

belt: A back-arc setting for the northwestern Hearne subdomain, western Churchill Province, Canada: Precambrian Research, v. 144, no. 1-2, p. 140-165.

Sanfilippo, A., Dick, H. J. B., and Ohara, Y., 2013, Melt-Rock Reaction in the Mantle: Mantle Troctolites from the Parece Vela Ancient Back-Arc Spreading Center: Journal of Petrology, v. 54, no. 5, p. 861-885.

Sarifakioglu, E., Ozen, H., and Winchester, J. A., 2009, Petrogenesis of the Refahiye Ophiolite and its Tectonic Significance for Neotethyan Ophiolites Along the Izmir-Ankara-Erzincan Suture Zone: Turkish Journal of Earth Sciences, v. 18, no. 2, p. 187-207.

Shafaii Moghadam, H., Zaki Khedr, M., Arai, S., Stern, R. J., Ghorbani, G., Tamura, A., and Ottley, C. J., 2015, Arc-related harzburgite–dunite–chromitite complexes in the mantle section of the Sabzevar ophiolite, Iran: A model for formation of podiform chromitites: Gondwana Research, v. 27, no. 2, p. 575-593.

Shaw, S. E., and Flood, R. H., 2009, Zircon Hf Isotopic Evidence for Mixing of Crustal and Silicic Mantle-derived Magmas in a Zoned Granite Pluton, Eastern Australia: Journal of Petrology, v. 50, no. 1, p. 147-168.

Shervais, J. W., 1982, Ti-V plots and the petrogenesis of modern and ophiolitic lavas: Earth and planetary science letters, v. 59, no. 1, p. 101-118.

Shinjo, R., 1999, Geochemistry of high Mg andesites and the tectonic evolution of the Okinawa Trough Ryukyu arc system: Chemical Geology, v. 157, no. 1-2, p. 69-88.

Shinjo, R., Chung, S. L., Kato, Y., and Kimura, M., 1999, Geochemical and Sr‐Nd isotopic characteristics of volcanic rocks from the Okinawa Trough and Ryukyu Arc: Implications for the evolution of a young, intracontinental back arc basin: Journal of Geophysical Research: Solid Earth, v. 104, no. B5, p. 10591-10608.

1662 Shojaat, B., Hassanipak, A. A., Mobasher, K., and Ghazi, A. M., 2003, Petrology,
1663 geochemistry and tectonics of the Sabzevar ophiolite, North Central Iran: Journal
1664 of Asian Earth Sciences, v. 21, no. 9, p. 1053-1067.

1665 Sorbadere, F., Schiano, P., Metrich, N., and Bertagnini, A., 2013, Small-scale coexistence
1666 of island-arc- and enriched-MORB-type basalts in the central Vanuatu arc:
1667 Contributions to Mineralogy and Petrology, v. 166, no. 5, p. 1305-1321.

1668 Stern, R. J., 2002, Subduction zones: Reviews of Geophysics, v. 40, no. 4.

1669 Stern, R. J., 2004, Subduction initiation: spontaneous and induced: Earth and Planetary
1670 Science Letters, v. 226, no. 3-4, p. 275-292.

1671 Stern, R. J., and Dickinson, W. R., 2010, The Gulf of Mexico is a Jurassic backarc basin:
1672 Geosphere, v. 6, no. 6, p. 739-754.

1673 Stern, R. J., and Gerya, T., 2017, Subduction initiation in nature and models: A review:
1674 Tectonophysics.

1675 Stracke, A., Hofmann, A. W., and Hart, S. R., 2005, FOZO, HIMU, and the rest of the
1676 mantle zoo: Geochemistry Geophysics Geosystems, v. 6.

1677 Tadayon, M., Rossetti, F., Zattin, M., Calzolari, G., Nozaem, R., Salvini, F., Faccenna, C.,
1678 and Khodabakhshi, P., 2018, The long‐term evolution of the Doruneh Fault region
1679 (Central Iran): A key to understanding the spatio‐temporal tectonic evolution in
1680 the hinterland of the Zagros convergence zone: Geological Journal, p. 1-26.

1681 Tadayon, M., Rossetti, F., Zattin, M., Nozaem, R., Calzolari, G., Madanipour, S., and
1682 Salvini, F., 2017, The Post-Eocene Evolution of the Doruneh Fault Region (Central
1683 Iran): The Intraplate Response to the Reorganization of the Arabia-Eurasia
1684 Collision Zone: Tectonics, v. 36, p. 3038-3064.

1685 Taylor, B., and Martinez, F., 2003, Back-arc basin basalt systematics: Earth and Planetary
1686 Science Letters, v. 210, no. 3-4, p. 481-497.

1687 Thomas, J.-C., Grasso, J.-R., Bossu, R., Martinod, J., and Nurtaev, B., 1999, Recent
1688 deformation in the Turan and South Kazakh platforms, western central Asia, and
1689 its relation to Arabia-Asia and India-Asia collisions: Tectonics, v. 18, no. 2, p. 201-
1690 214.

1691 Tian, L. Y., Castillo, P. R., Hilton, D. R., Hawkins, J. W., Hanan, B. B., and Pietruszka, A.
1692 J., 2011, Major and trace element and Sr-Nd isotope signatures of the northern Lau
1693 Basin lavas: Implications for the composition and dynamics of the back-arc basin
1694 mantle: Journal of Geophysical Research-Solid Earth, v. 116.

1695 Tiepolo, M., Oberti, R., Zanetti, A., Vannucci, R., and Foley, S. F., 2007, Trace-element
1696 partitioning between amphibole and silicate melt: Reviews in mineralogy and
1697 geochemistry, v. 67, no. 1, p. 417-452.

1698 Todd, E., Gill, J. B., Wysoczanski, R. J., Hergt, J., Wright, I. C., Leybourne, M. I., and
1699 Mortimer, N., 2011, Hf isotopic evidence for small-scale heterogeneity in the mode
1700 of mantle wedge enrichment: Southern Havre Trough and South Fiji Basin back
1701 arcs: Geochemistry Geophysics Geosystems, v. 12.

1702 Uner, T., Cakir, U., Ozdemir, Y., and Arat, I., 2014, Geochemistry and origin of
1703 plagiogranites from the Eldivan Ophiolite, Cankiri (Central Anatolia, Turkey):
1704 Geologica Carpathica, v. 65, no. 3, p. 195-205.

1705 Vaezi Pour, M. J., Alavi Tehrani, N., Behrouzi, A., and Kholghi, M. H., 1992, Geologocal
1706 Map of the Torbat-e-Heydarieh: Geological Survey of Iran.

1707 van Hinsbergen, D. J. J., Peters, K., Maffione, M., Spakman, W., Guilmette, C., Thieulot,
1708 C., Plumper, O., Gurer, D., Brouwer, F. M., Aldanmaz, E., and Kaymakci, N., 2015,
1709 Dynamics of intraoceanic subduction initiation: 2. Suprasubduction zone ophiolite
1710 formation and metamorphic sole exhumation in context of absolute plate motions:
1711 Geochemistry Geophysics Geosystems, v. 16, no. 6, p. 1771-1785.

1712 Verdel, C., Wernicke, B. P., Hassanzadeh, J., and Guest, B., 2011, A Paleogene extensional
1713 arc flare-up in Iran: Tectonics, v. 30.

1714 Verdel, C., Wernicke, B. P., Ramezani, J., Hassanzadeh, J., Renne, P. R., and Spell, T. L.,
1715 2007, Geology and thermochronology of Tertiary Cordilleran-style metamorphic
1716 core complexes in the Saghand region of central Iran: Geological Society of
1717 America Bulletin, v. 119, no. 7-8, p. 961-977.

1718 Vervoort, J. D., and Blichert-Toft, J., 1999a, Evolution of the depleted mantle: Hf isotope
1719 evidence from juvenile rocks through time: Geochimica et Cosmochimica Acta, v.
1720 63, no. 3, p. 533-556.

1721 Vervoort, J. D., and Blichert-Toft, J., 1999b, Evolution of the depleted mantle: Hf isotope
1722 evidence from juvenile rocks through time: Geochimica Et Cosmochimica Acta, v.
1723 63, no. 3-4, p. 533-556.

1724 Vervoort, J. D., Patchett, P. J., Blichert-Toft, J., and Albarede, F., 1999, Relationships
1725 between Lu-Hf and Sm-Nd isotopic systems in the global sedimentary system:
1726 Earth and Planetary Science Letters, v. 168, no. 1-2, p. 79-99.

1727 Whattam, S. A., and Stern, R. J., 2011, The 'subduction initiation rule': a key for linking
1728 ophiolites, intra-oceanic forearcs, and subduction initiation: Contributions to
1729 Mineralogy and Petrology, v. 162, no. 5, p. 1031-1045.

1730 Woodhead, J., Hergt, J., Davidson, J., and Eggins, S., 2001, Hafnium isotope evidence for
1731 ‘conservative’element mobility during subduction zone processes: Earth and
1732 Planetary Science Letters, v. 192, no. 3, p. 331-346.

1733 Woodhead, J., Stern, R. J., Pearce, J., Hergt, J., and Vervoort, J., 2012, Hf-Nd isotope
1734 variation in Mariana Trough basalts: The importance of "ambient mantle" in the
1735 interpretation of subduction zone magmas: Geology, v. 40, no. 6, p. 539-542.

1736 Woodhead, J. D., and Devey, C. W., 1993, Geochemistry of the Pitcairn Seamounts .1.
1737 Source Character and Temporal Trends: Earth and Planetary Science Letters, v.
1738 116, no. 1-4, p. 81-99.

1739 Woodhead, J. D., and Hergt, J. M., 2005, A preliminary appraisal of seven natural zircon
1740 reference materials for in situ Hf isotope determination: Geostandards and
1741 Geoanalytical Research, v. 29, no. 2, p. 183-195.

1742 Yogodzinski, G. M., Vervoort, J. D., Brown, S. T., and Gerseny, M., 2010, Subduction
1743 controls of Hf and Nd isotopes in lavas of the Aleutian island arc: Earth and
1744 Planetary Science Letters, v. 300, no. 3-4, p. 226-238.

1745 Yuan, H. L., Gao, S., Dai, M. N., Zong, C. L., Gunther, D., Fontaine, G. H., Liu, X. M.,
1746 and Diwu, C., 2008, Simultaneous determinations of U-Pb age, Hf isotopes and
1747 trace element compositions of zircon by excimer laser-ablation quadrupole and
1748 multiple-collector ICP-MS: Chemical Geology, v. 247, no. 1-2, p. 100-118.

1749 Zarrinkoub, M. H., Pang, K. N., Chung, S. L., Khatib, M. M., Mohammadi, S. S., Chiu, H.
1750 Y., and Lee, H. Y., 2012, Zircon U-Pb age and geochemical constraints on the
1751 origin of the Birjand ophiolite, Sistan suture zone, eastern Iran: Lithos, v. 154, p.
1752 392-405.
1753

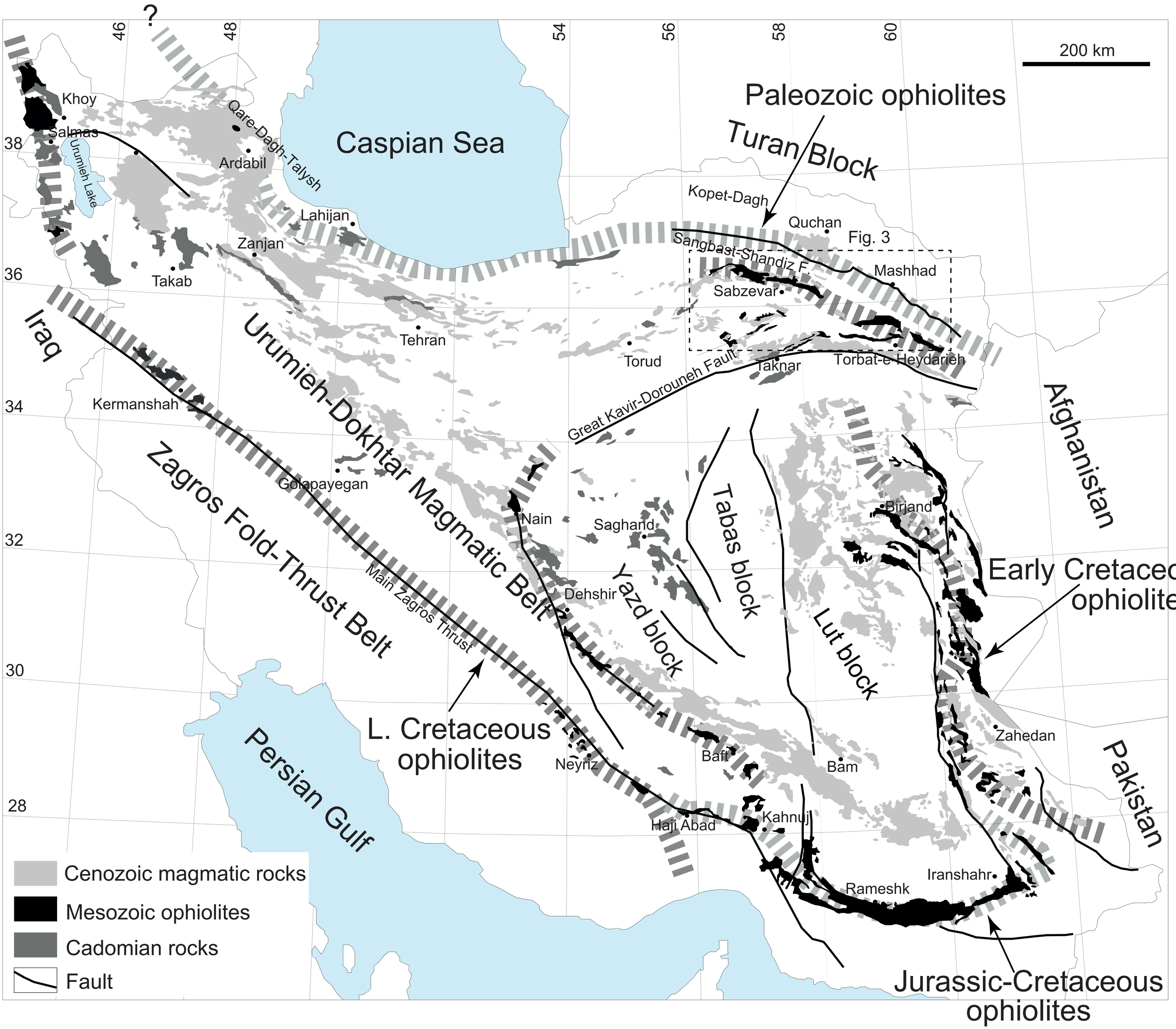
?
46
48
54
56
58
60
200 km
Paleozoic ophiolites
Turan Block
Caspian Sea
Khoy
Salmas
Urumieh Lake
Ardabil
Qare-Dagh-Talysh
Kopet-Dagh
Quchan
Fig. 3
Sangbast-Shandiz F.
Mashhad
Sabzevar
Lahijan
Zanjan
Takab
Tehran
Torud
Taknar
Torbat-e Heydarieh
Great Kavir-Dorouneh Fault
Afghanistan
38
36
34
32
30
28
Iraq
Kermanshah
Urumieh-Dokhtar Magmatic Belt
Zagros Fold-Thrust Belt
Golapayegan
Main Zagros Thrust
Nain
Saghand
Dehshir
Yazd block
Tabas block
Lut block
Birjand
Early Cretaceous ophiolites
L. Cretaceous ophiolites
Persian Gulf
Neyriz
Baft
Bam
Zahedan
Pakistan
Haji Abad
Kahnuj
Iranshahr
Rameshk
Jurassic-Cretaceous ophiolites
Cenozoic magmatic rocks
Mesozoic ophiolites
Cadomian rocks
Fault

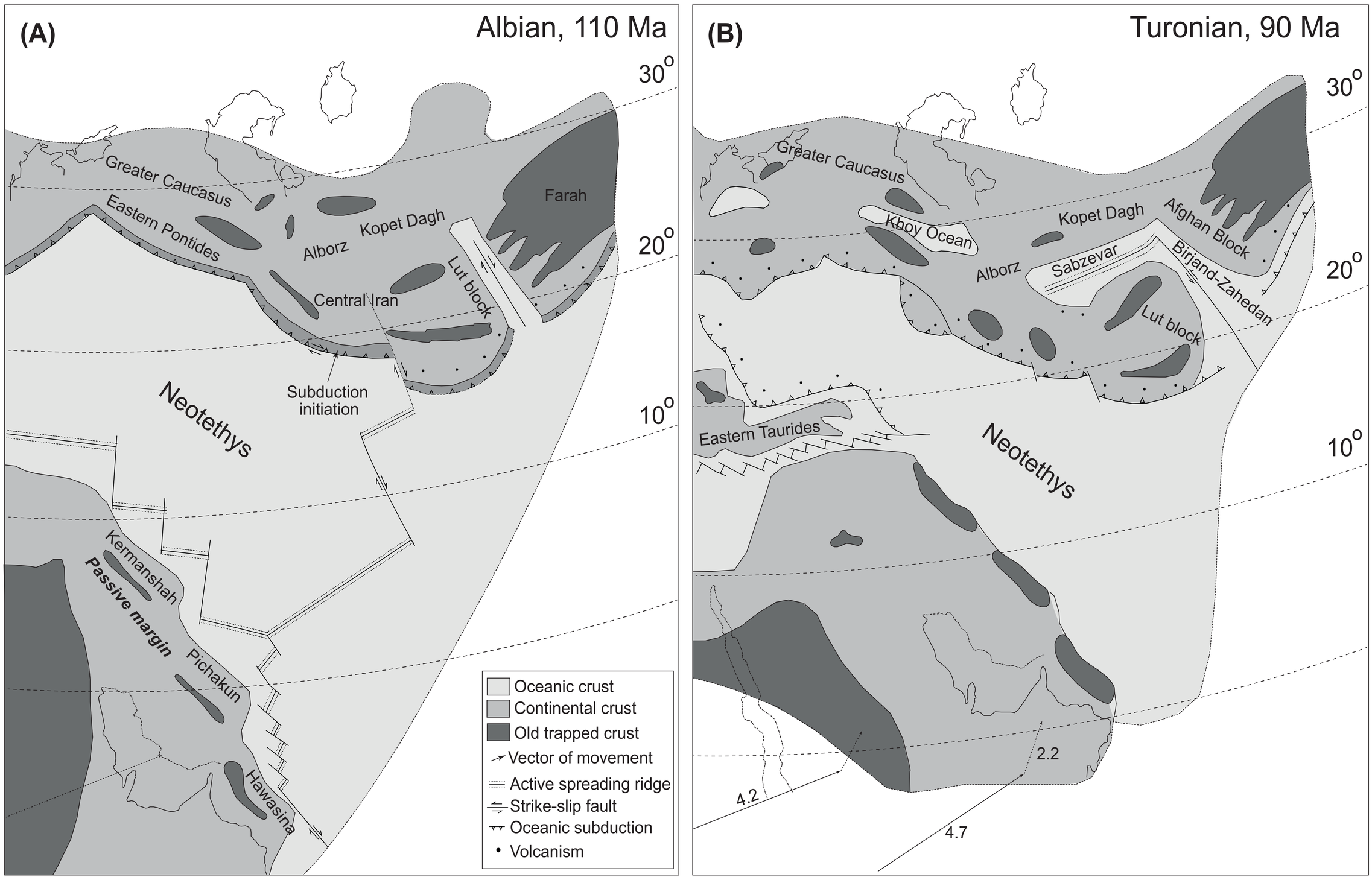
(A)
Albian, 110 Ma
30°
20°
10°
Greater Caucasus
Eastern Pontides
Alborz
Kopet Dagh
Farah
Central Iran
Lut block
Subduction initiation
Neotethys
Kermanshah
Passive margin
Pichakun
Hawasina
Oceanic crust
Continental crust
Old trapped crust
Vector of movement
Active spreading ridge
Strike-slip fault
Oceanic subduction
Volcanism
(B)
Turonian, 90 Ma
30°
20°
10°
Greater Caucasus
Khoy Ocean
Kopet Dagh
Afghan Block
Alborz
Sabzevar
Birjand-Zahedan
Lut block
Eastern Taurides
Neotethys
2.2
4.2
4.7

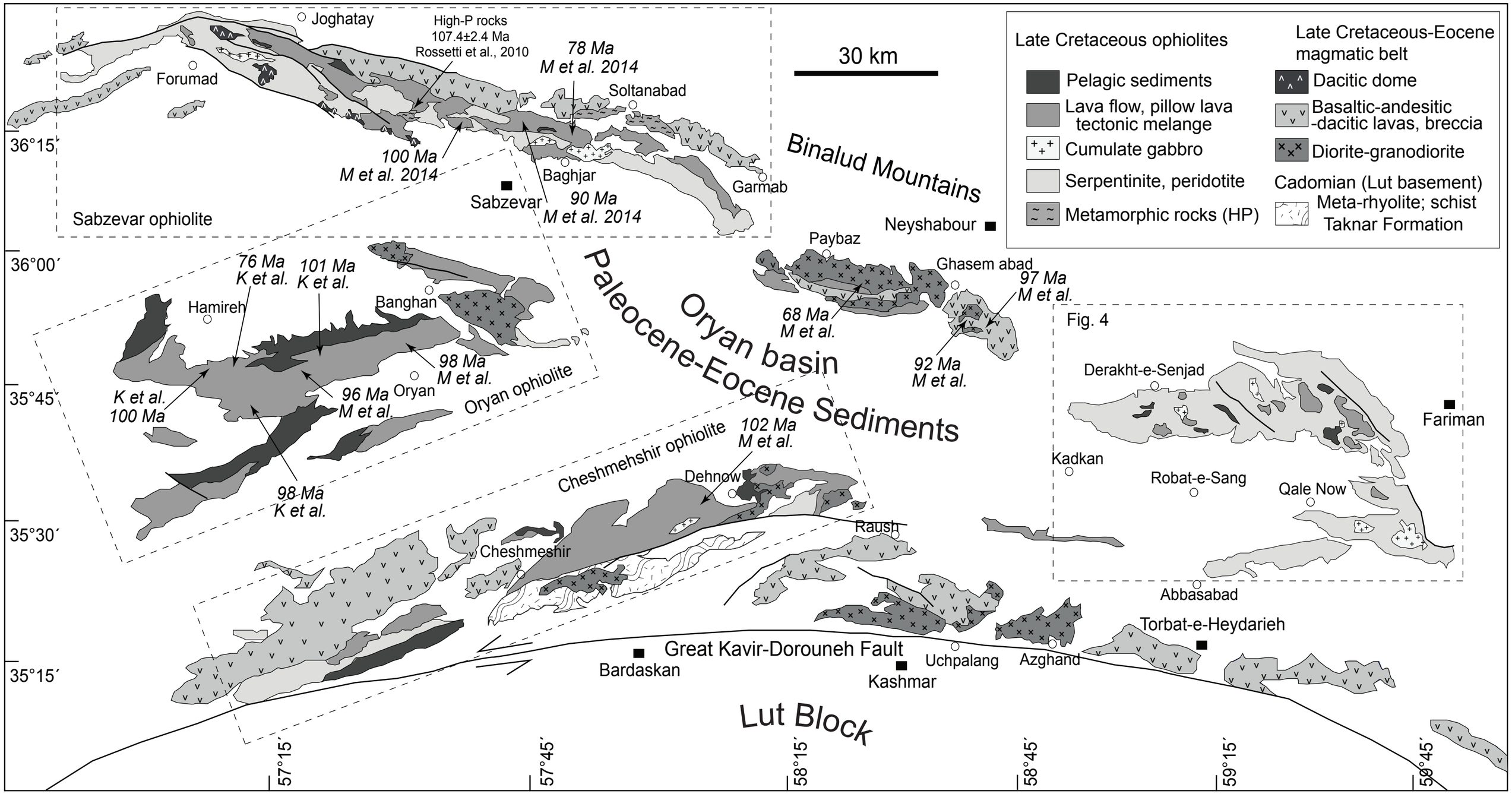
Late Cretaceous ophiolites
Pelagic sediments
Lava flow, pillow lava tectonic melange
Cumulate gabbro
Serpentinite, peridotite
Metamorphic rocks (HP)
Late Cretaceous-Eocene magmatic belt
Dacitic dome
Basaltic-andesitic -dacitic lavas, breccia
Diorite-granodiorite
Cadomian (Lut basement)
Meta-rhyolite; schist Taknar Formation
30 km
Joghatay
High-P rocks
107.4±2.4 Ma
Rossetti et al., 2010
78 Ma
M et al. 2014
Forumad
Soltanabad
100 Ma
M et al. 2014
Baghjar
Garmab
Sabzevar
90 Ma
M et al. 2014
Sabzevar ophiolite
Binalud Mountains
Neyshabour
Paybaz
Ghasem abad
97 Ma
M et al.
68 Ma
M et al.
92 Ma
M et al.
Fig. 4
Derakht-e-Senjad
Fariman
Kadkan
Robat-e-Sang
Qale Now
Abbasabad
Torbat-e-Heydarieh
76 Ma
K et al.
101 Ma
K et al.
Hamireh
Banghan
98 Ma
M et al.
K et al.
100 Ma
96 Ma
M et al.
Oryan
Oryan ophiolite
98 Ma
K et al.
Paleocene-Eocene Sediments
Oryan basin
Cheshmehshir ophiolite
102 Ma
M et al.
Dehnow
Cheshmeshir
Raush
Great Kavir-Dorouneh Fault
Bardaskan
Kashmar
Uchpalang
Azghand
Lut Block
36°15′
36°00′
35°45′
35°30′
35°15′
57°15′
57°45′
58°15′
58°45′
59°15′
60°45′

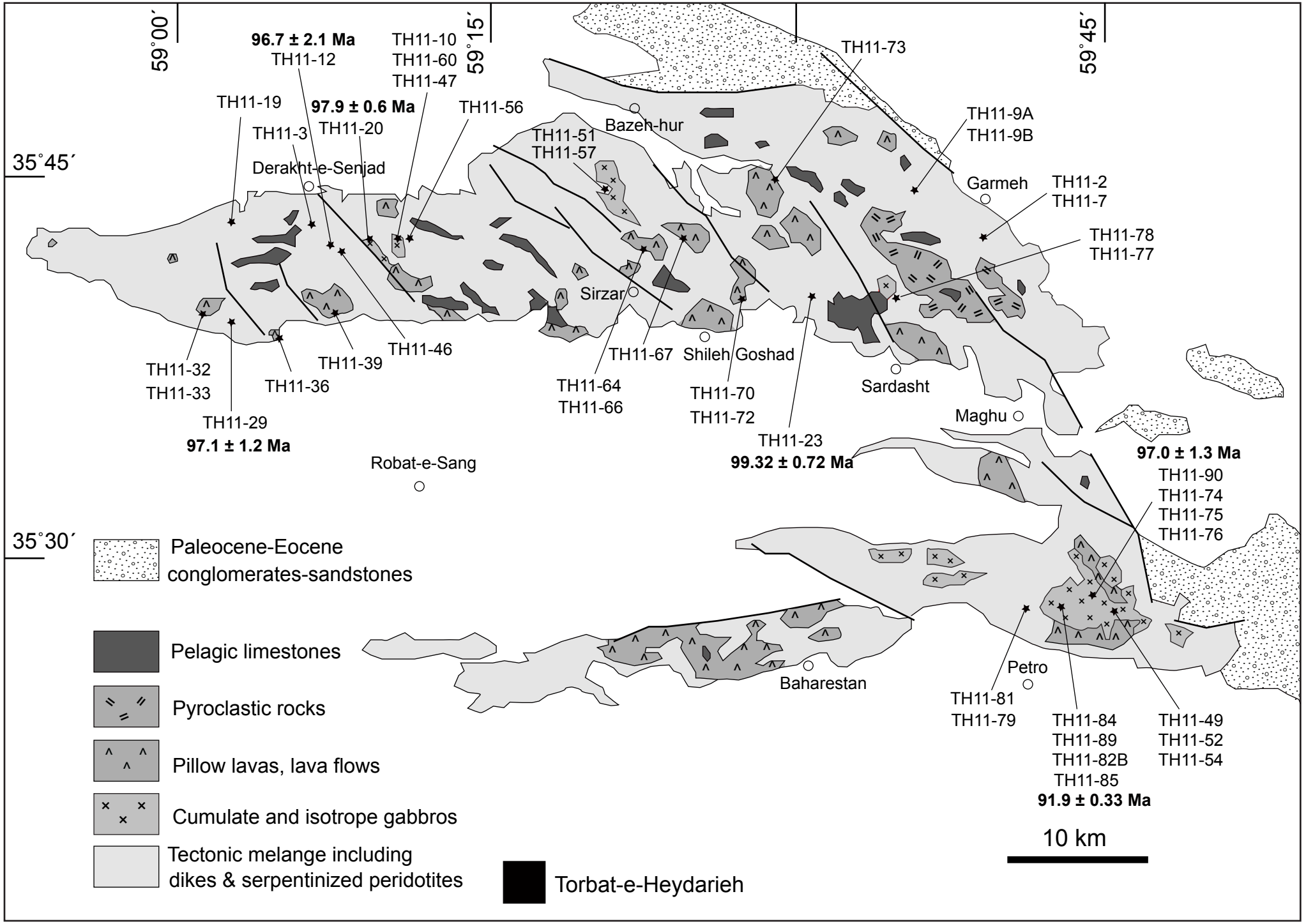
59˚00´
59˚15´
59˚45´
35˚45´
35˚30´
96.7 ± 2.1 Ma
TH11-12
TH11-10
TH11-60
TH11-47
97.9 ± 0.6 Ma
TH11-20
TH11-19
TH11-3
TH11-56
Derakht-e-Senjad
Bazeh-hur
TH11-73
TH11-9A
TH11-9B
TH11-51
TH11-57
Garmeh
TH11-2
TH11-7
TH11-78
TH11-77
Sirzar
TH11-32
TH11-33
TH11-29
97.1 ± 1.2 Ma
TH11-36
TH11-39
TH11-46
TH11-67
Shileh Goshad
TH11-64
TH11-66
TH11-70
TH11-72
Sardasht
TH11-23
99.32 ± 0.72 Ma
Maghu
97.0 ± 1.3 Ma
TH11-90
TH11-74
TH11-75
TH11-76
Robat-e-Sang
Paleocene-Eocene
conglomerates-sandstones
Pelagic limestones
Pyroclastic rocks
Pillow lavas, lava flows
Cumulate and isotrope gabbros
Tectonic melange including
dikes & serpentinized peridotites
Torbat-e-Heydarieh
Baharestan
Petro
TH11-81
TH11-79
TH11-84
TH11-89
TH11-82B
TH11-85
91.9 ± 0.33 Ma
TH11-49
TH11-52
TH11-54
10 km

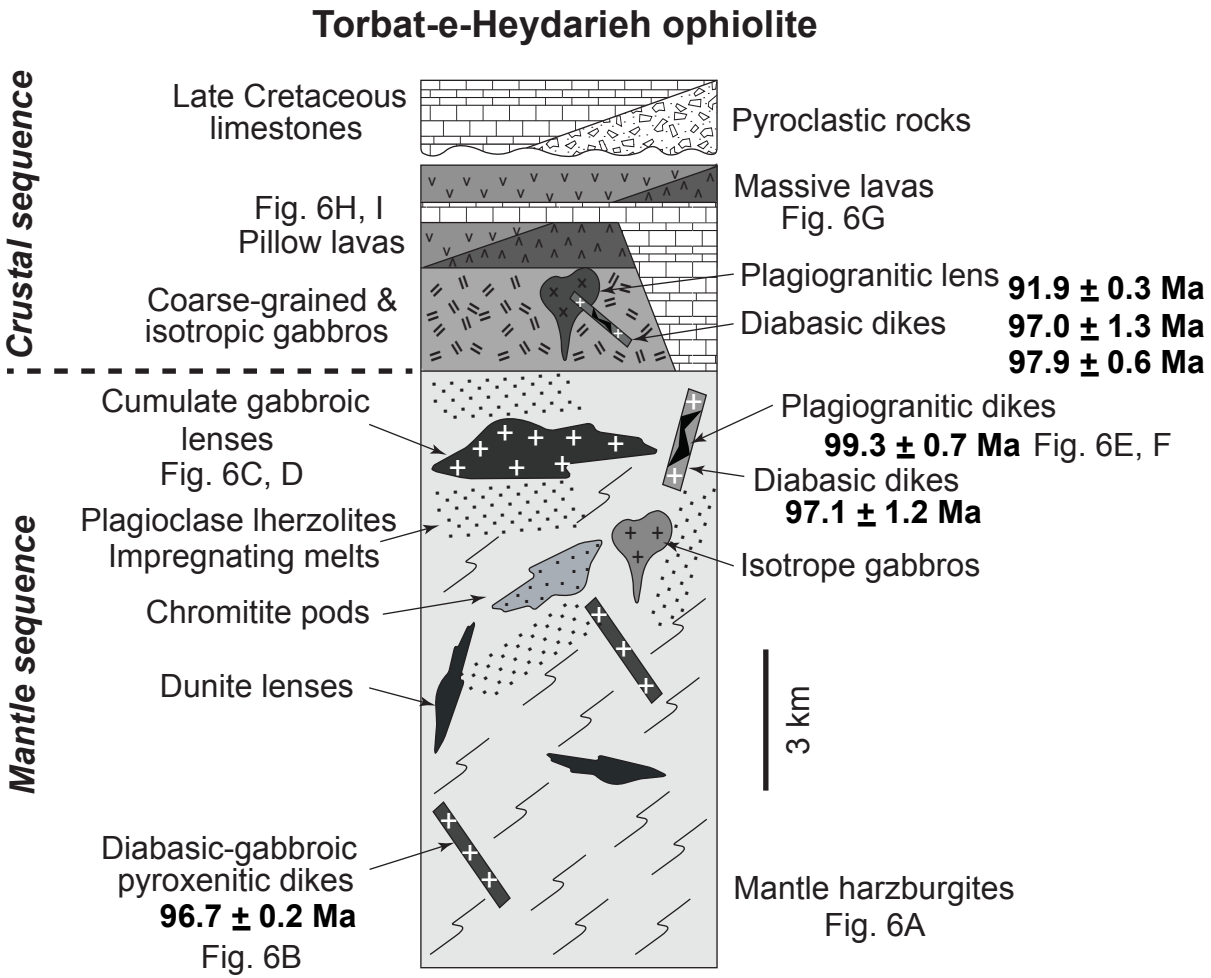
Torbat-e-Heydarieh ophiolite
Crustal sequence
Mantle sequence
Late Cretaceous limestones
Pyroclastic rocks
Massive lavas
Fig. 6G
Fig. 6H, I
Pillow lavas
Plagiogranitic lens
91.9 ± 0.3 Ma
Coarse-grained & isotropic gabbros
Diabasic dikes
97.0 ± 1.3 Ma
97.9 ± 0.6 Ma
Cumulate gabbroic lenses
Fig. 6C, D
Plagiogranitic dikes
99.3 ± 0.7 Ma
Fig. 6E, F
Diabasic dikes
97.1 ± 1.2 Ma
Plagioclase lherzolites
Impregnating melts
Isotrope gabbros
Chromitite pods
Dunite lenses
3 km
Diabasic-gabbroic pyroxenitic dikes
96.7 ± 0.2 Ma
Fig. 6B
Mantle harzburgites
Fig. 6A

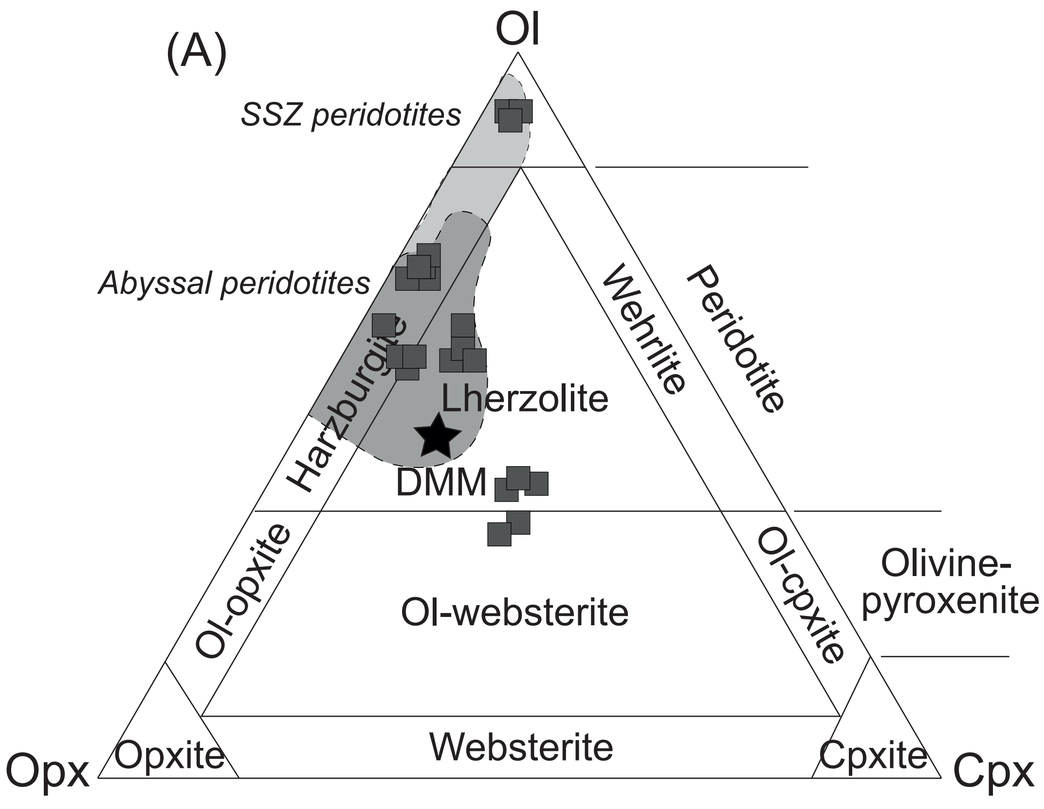
(A)
Ol
SSZ peridotites
Abyssal peridotites
Harzburgite
Lherzolite
DMM
Wehrlite
Peridotite
Ol-opxite
Ol-cpxite
Olivine-
pyroxenite
Ol-websterite
Opx
Opxite
Websterite
Cpxite
Cpx

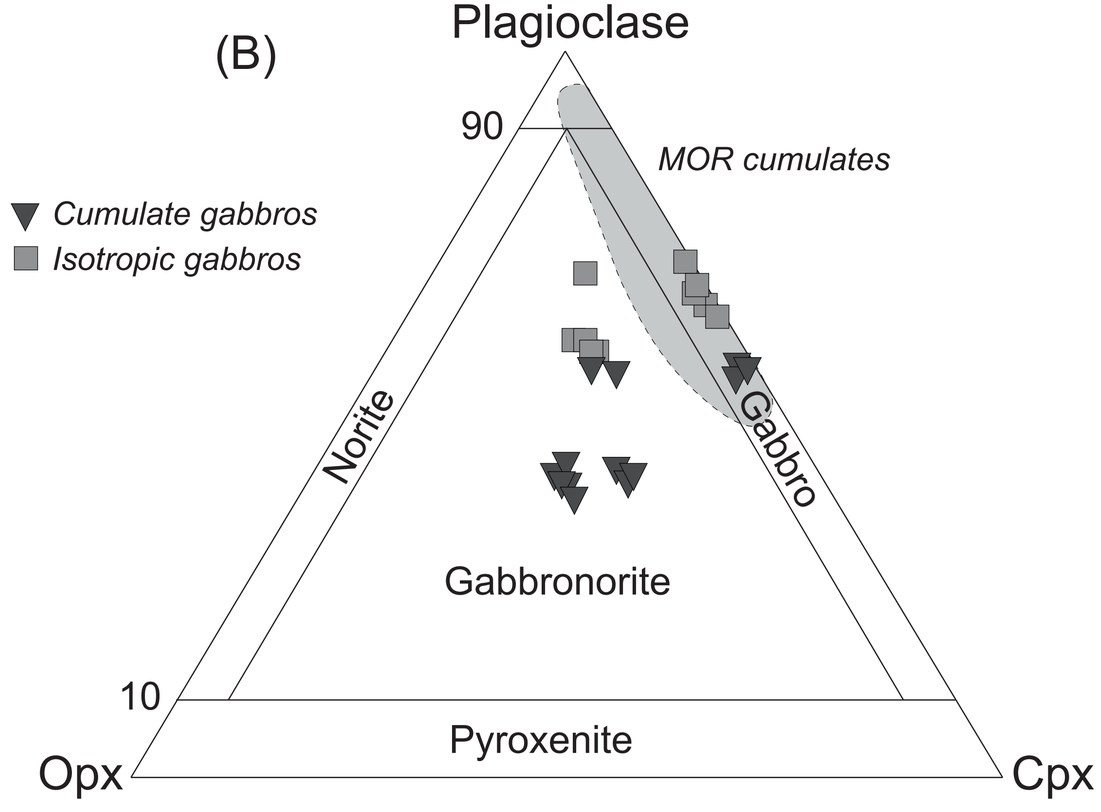
(B)
Plagioclase
90
MOR cumulates
Cumulate gabbros
Isotropic gabbros
Norite
Gabbro
Gabbronorite
10
Pyroxenite
Opx
Cpx

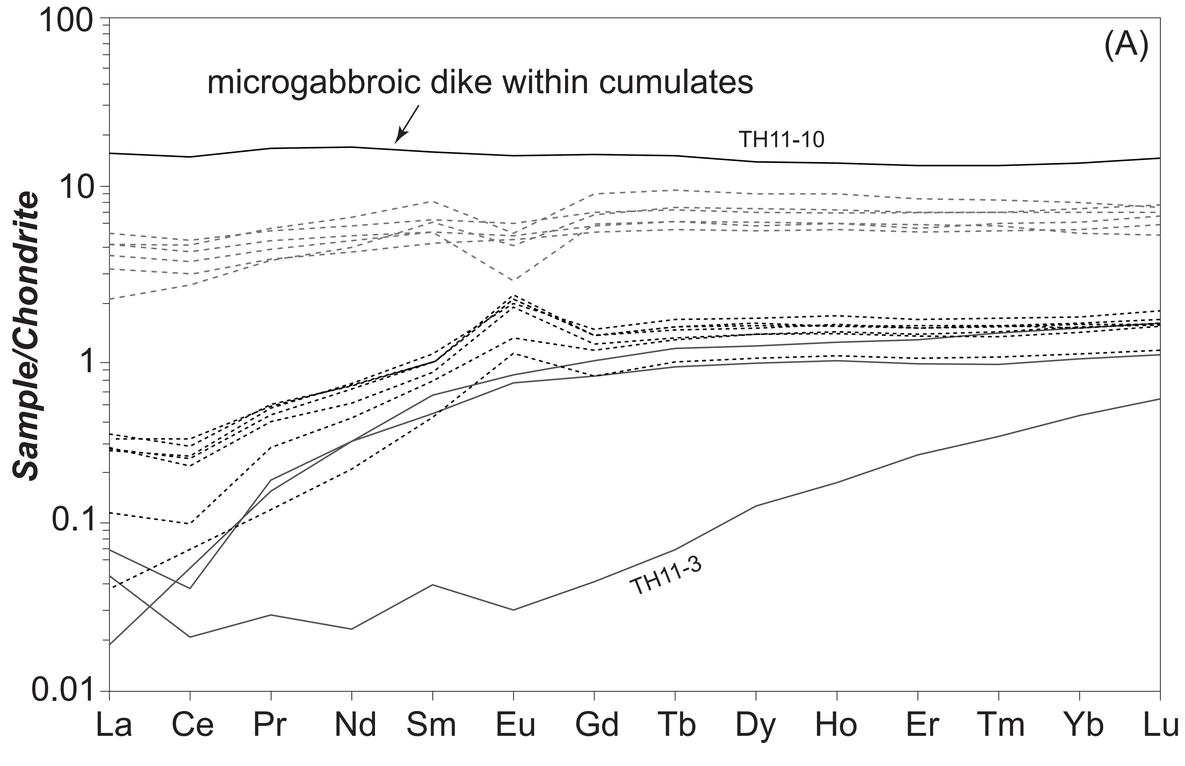
(A)
microgabbroic dike within cumulates
TH11-10
TH11-3
Sample/Chondrite
100
10
1
0.1
0.01
La Ce Pr Nd Sm Eu Gd Tb Dy Ho Er Tm Yb Lu

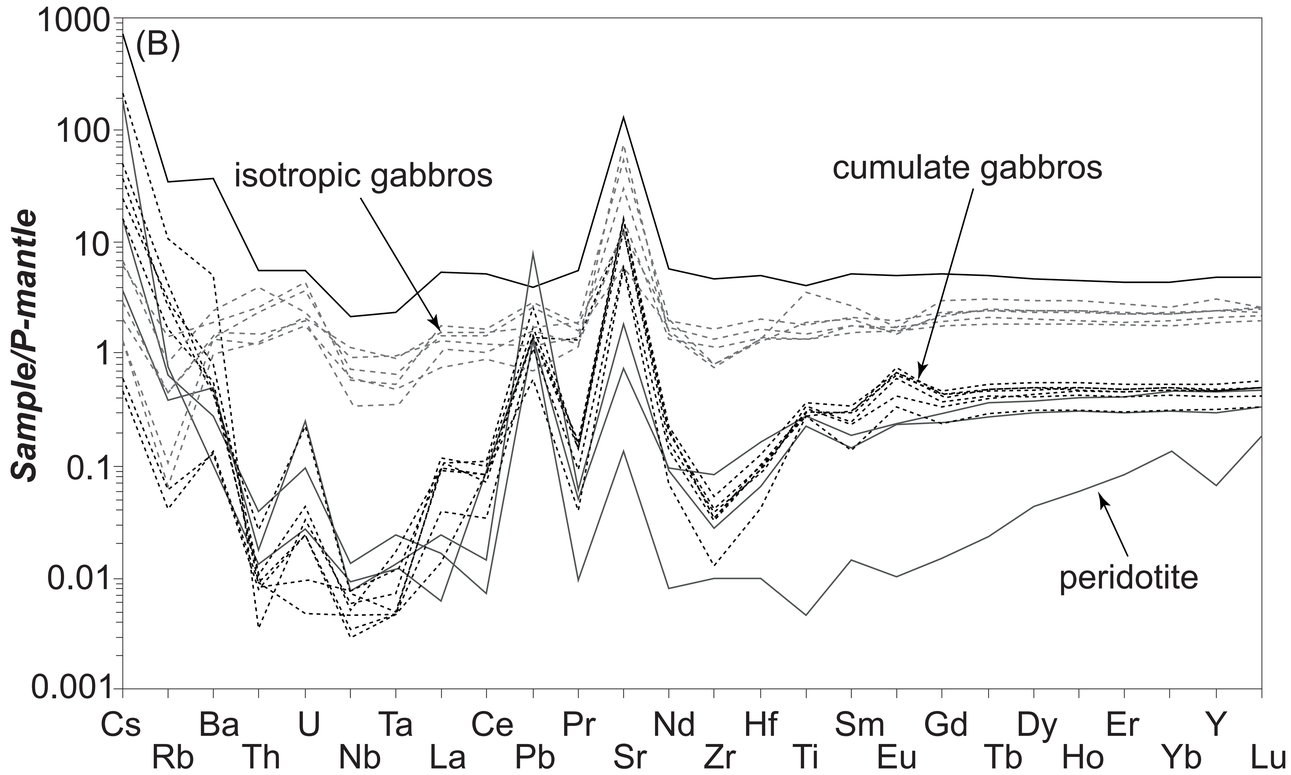
(B)
isotropic gabbros
cumulate gabbros
peridotite
Sample/P-mantle
1000
100
10
1
0.1
0.01
0.001
Cs Rb Ba Th U Nb Ta La Ce Pr Nd Hf Sm Gd Dy Er Y Lu

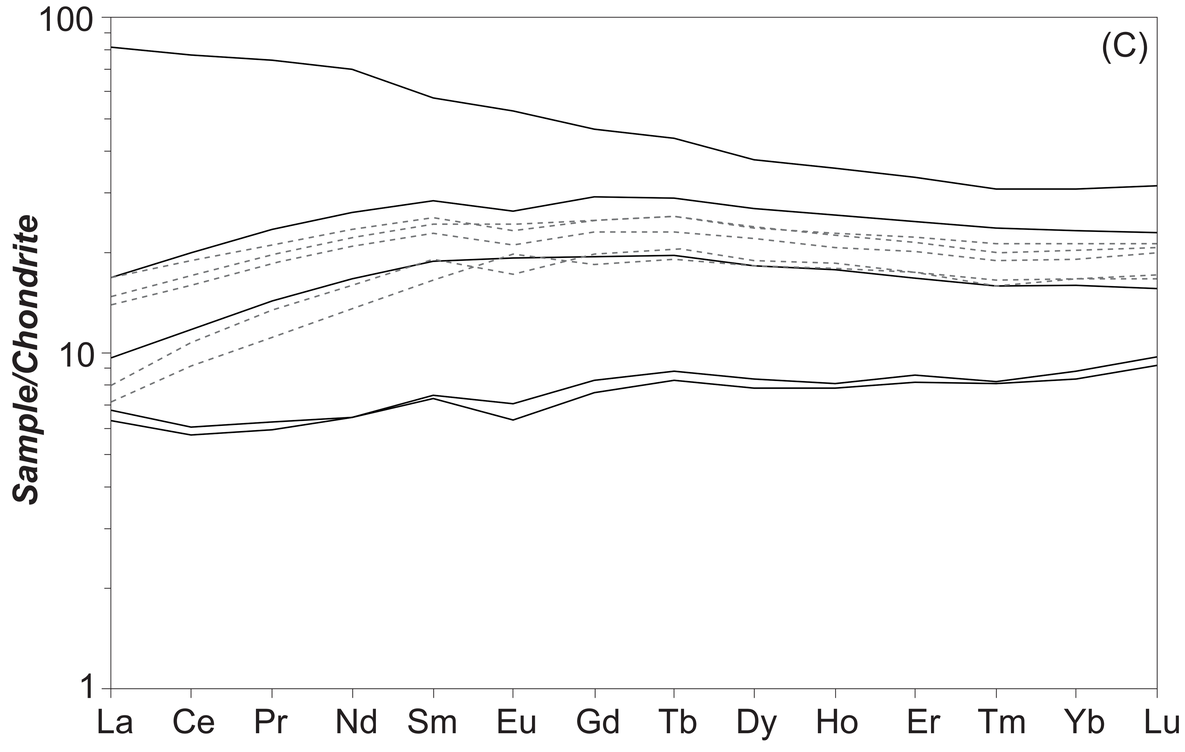
(C)
Sample/Chondrite
100
10
1
La Ce Pr Nd Sm Eu Gd Tb Dy Ho Er Tm Yb Lu

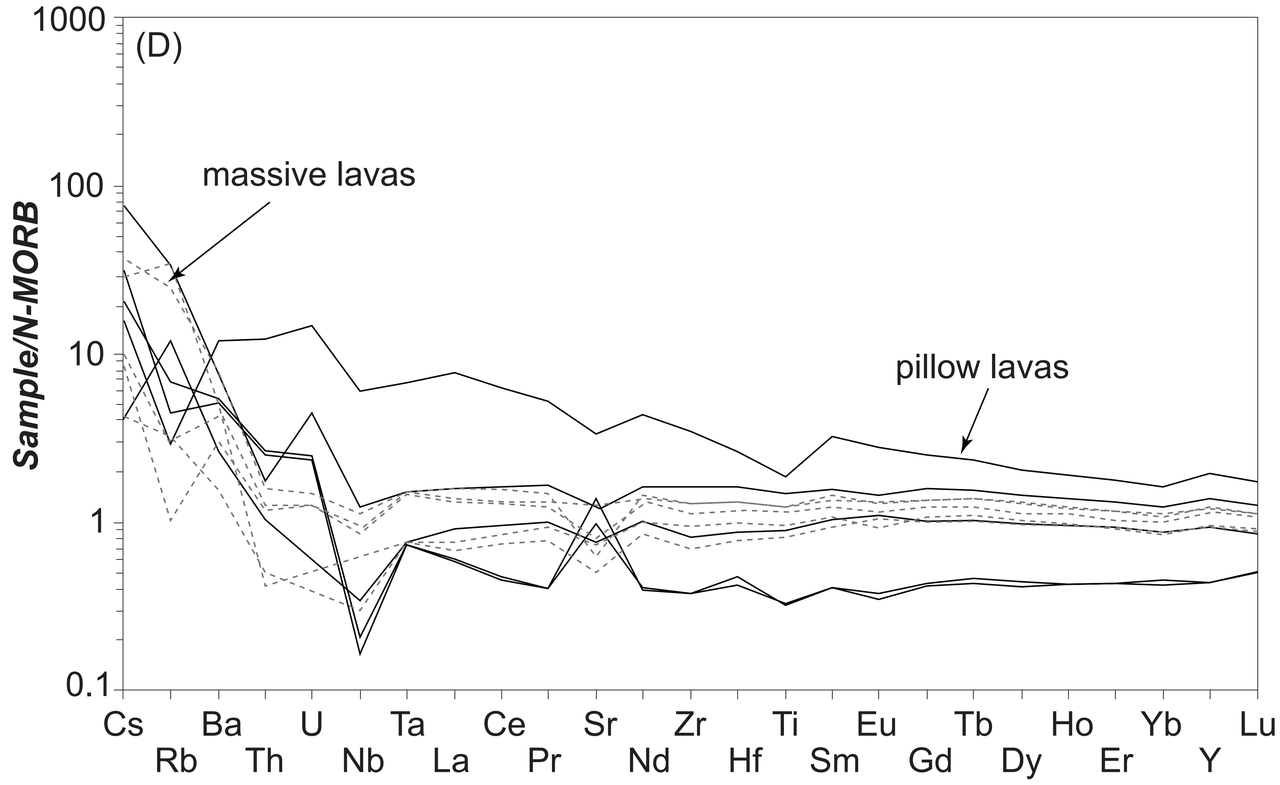
(D)
massive lavas
pillow lavas
Sample/N-MORB
1000
100
10
1
0.1
Cs Rb Ba Th U Nb Ta La Ce Pr Sr Nd Zr Hf Ti Sm Eu Gd Tb Dy Ho Er Y Yb Lu

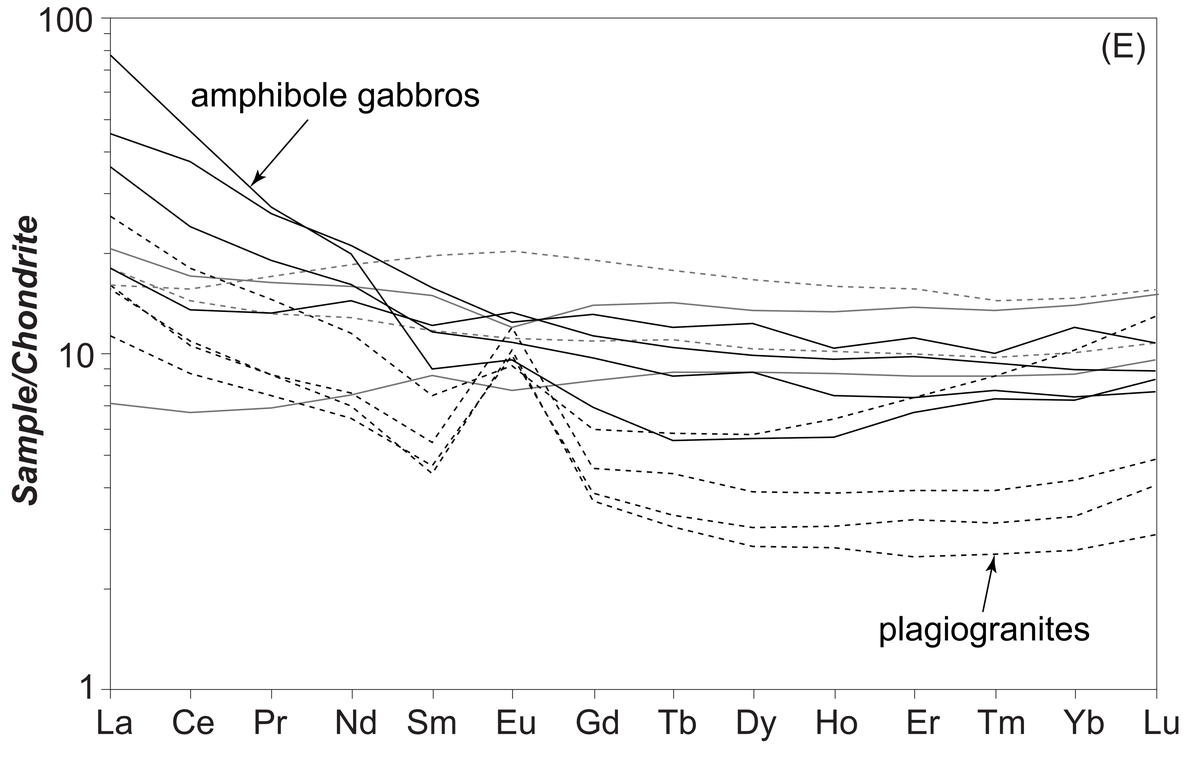
(E)
amphibole gabbros
plagiogranites
Sample/Chondrite
100
10
1
La Ce Pr Nd Sm Eu Gd Tb Dy Ho Er Tm Yb Lu

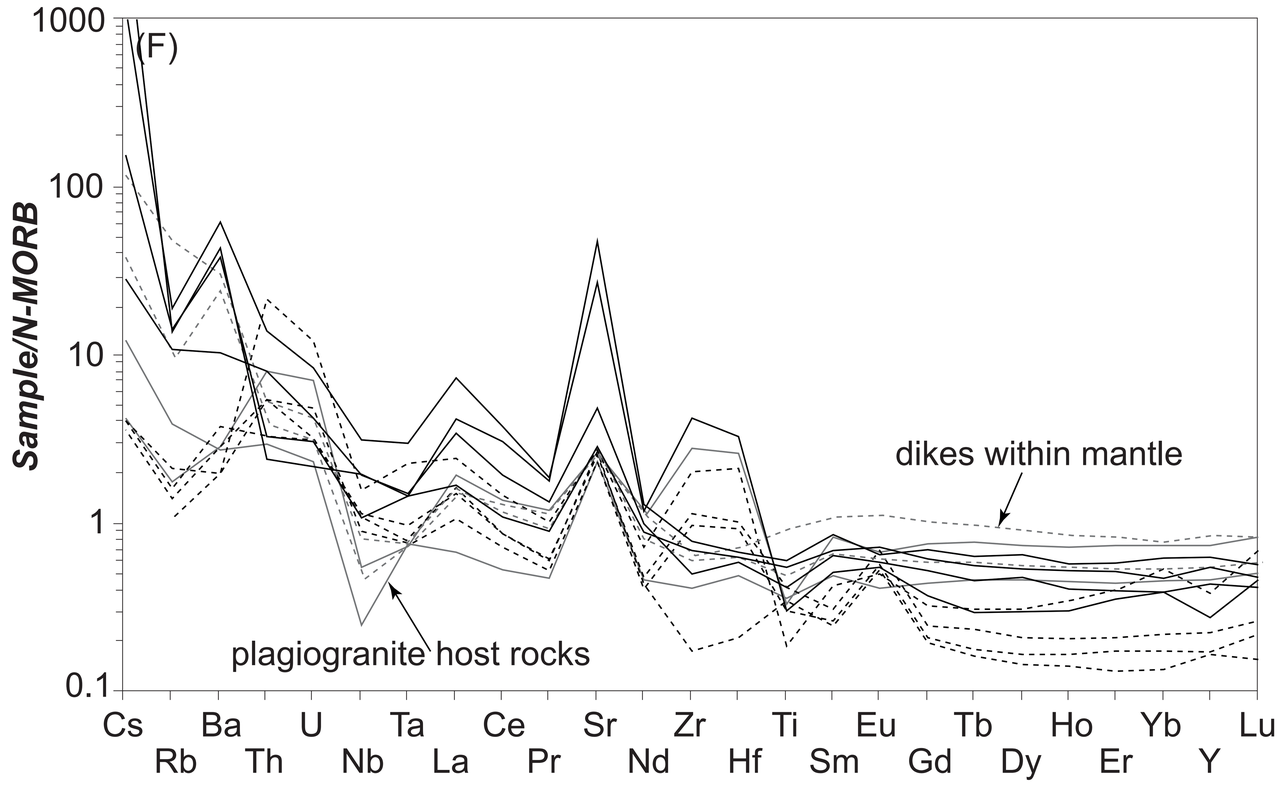
(F)
dikes within mantle
plagiogranite host rocks
Sample/N-MORB
1000
100
10
1
0.1
Cs Rb Ba Th U Nb Ta La Ce Pr Sr Nd Zr Hf Ti Sm Eu Gd Tb Dy Ho Er Y Yb Lu

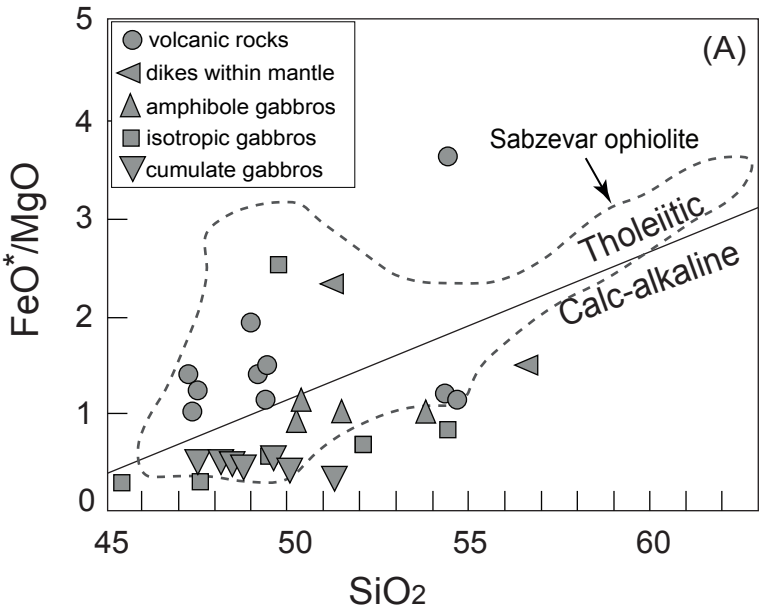
volcanic rocks
dikes within mantle
amphibole gabbros
isotropic gabbros
cumulate gabbros
(A)
Sabzevar ophiolite
Tholeiitic
Calc-alkaline
FeO*/MgO
SiO2
0
1
2
3
4
5
45
50
55
60

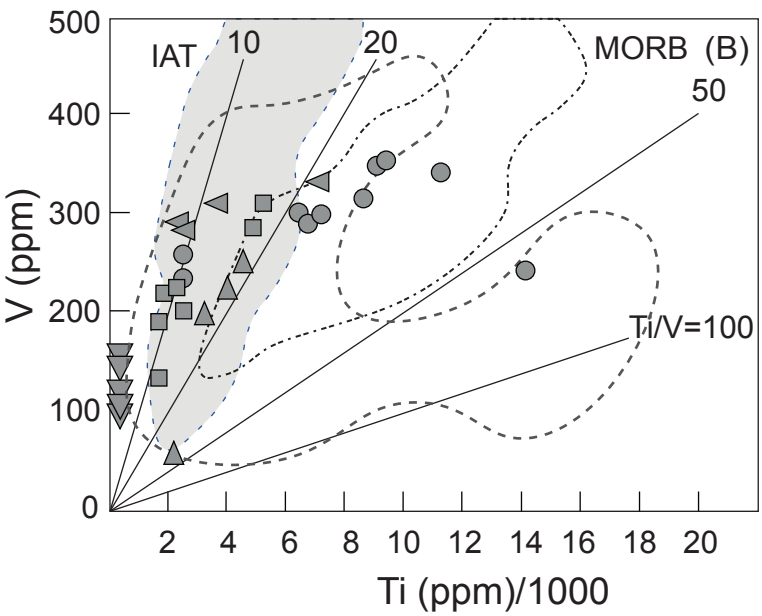
IAT
10
20
MORB
(B)
50
Ti/V=100
V (ppm)
Ti (ppm)/1000
0
100
200
300
400
500
2
4
6
8
10
12
14
16
18
20

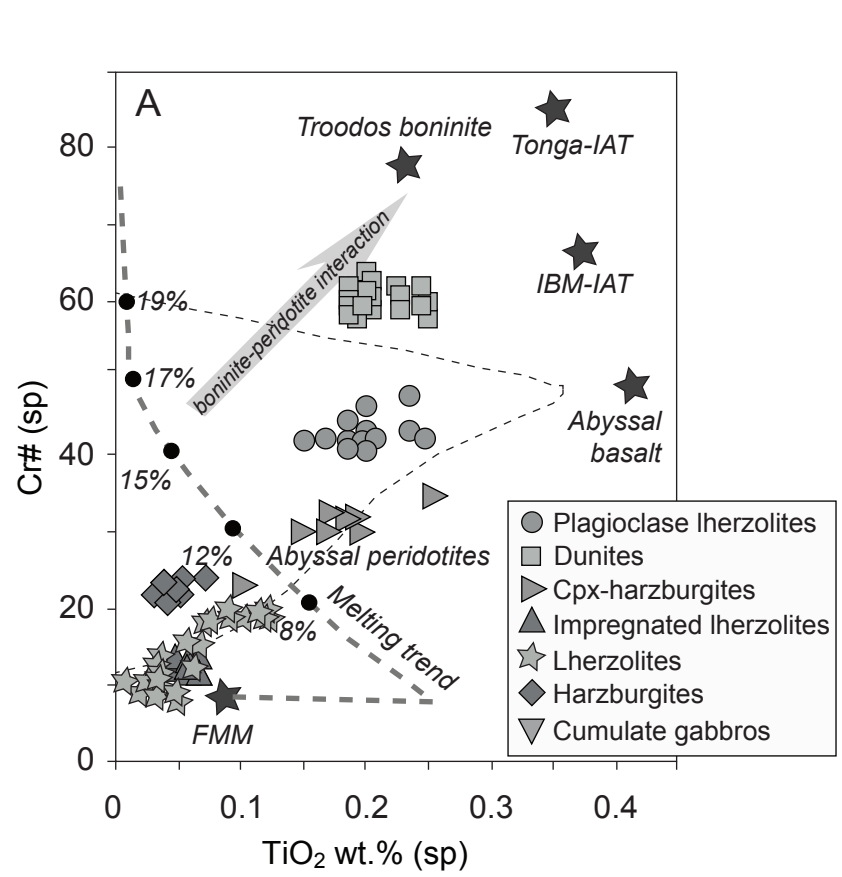
A
Troodos boninite
Tonga-IAT
IBM-IAT
Abyssal basalt
boninite-peridotite interaction
19%
17%
15%
12%
8%
Abyssal peridotites
Melting trend
FMM
Plagioclase lherzolites
Dunites
Cpx-harzburgites
Impregnated lherzolites
Lherzolites
Harzburgites
Cumulate gabbros
Cr# (sp)
TiO2 wt.% (sp)
0
20
40
60
80
0
0.1
0.2
0.3
0.4

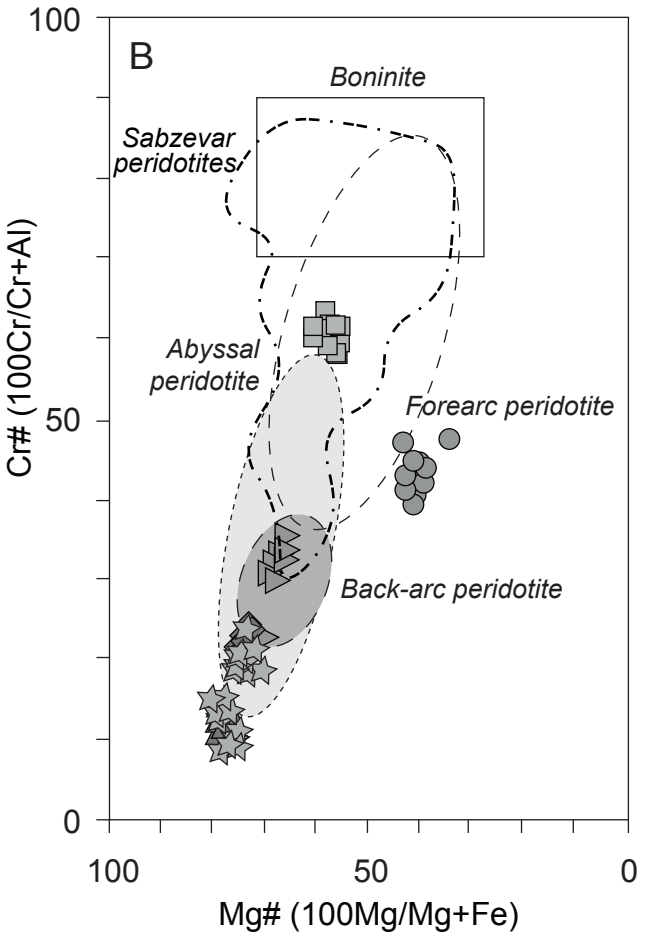
B
Boninite
Sabzevar peridotites
Abyssal peridotite
Forearc peridotite
Back-arc peridotite
Cr# (100Cr/Cr+Al)
Mg# (100Mg/Mg+Fe)
0
50
100
100
50
0

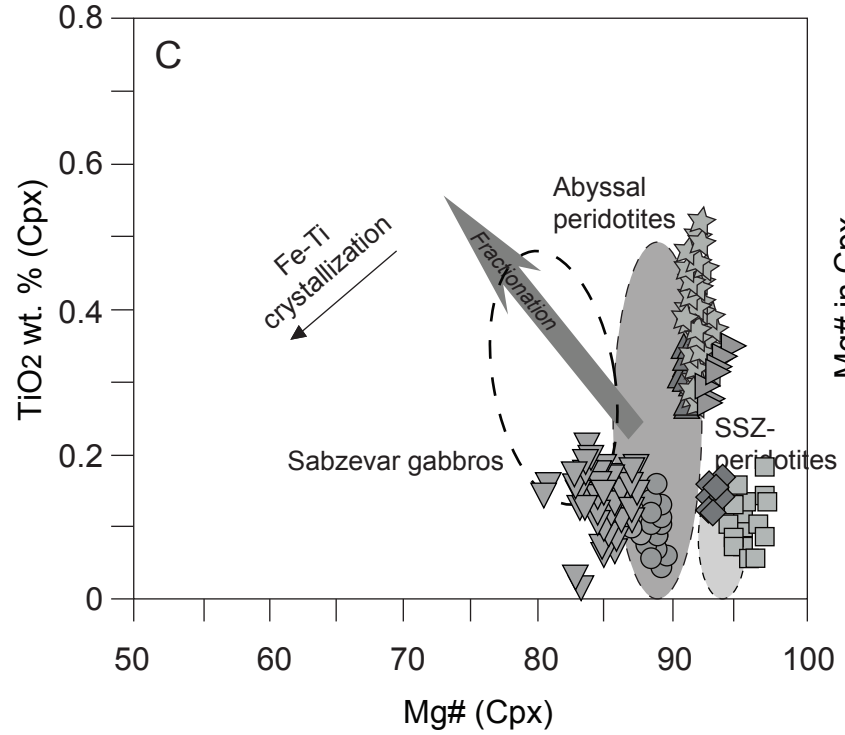
C
Fe-Ti crystallization
Fractionation
Abyssal peridotites
Sabzevar gabbros
SSZ-peridotites
TiO2 wt. % (Cpx)
Mg# (Cpx)
0
0.2
0.4
0.6
0.8
50
60
70
80
90
100

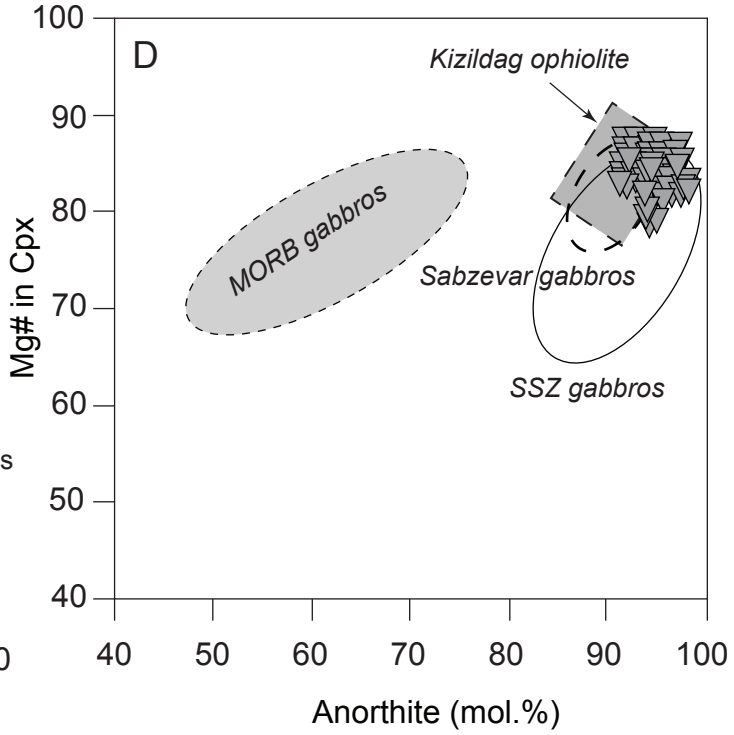
D
Kizildag ophiolite
MORB gabbros
Sabzevar gabbros
SSZ gabbros
Mg# in Cpx
Anorthite (mol.%)
40
50
60
70
80
90
100
40
50
60
70
80
90
100

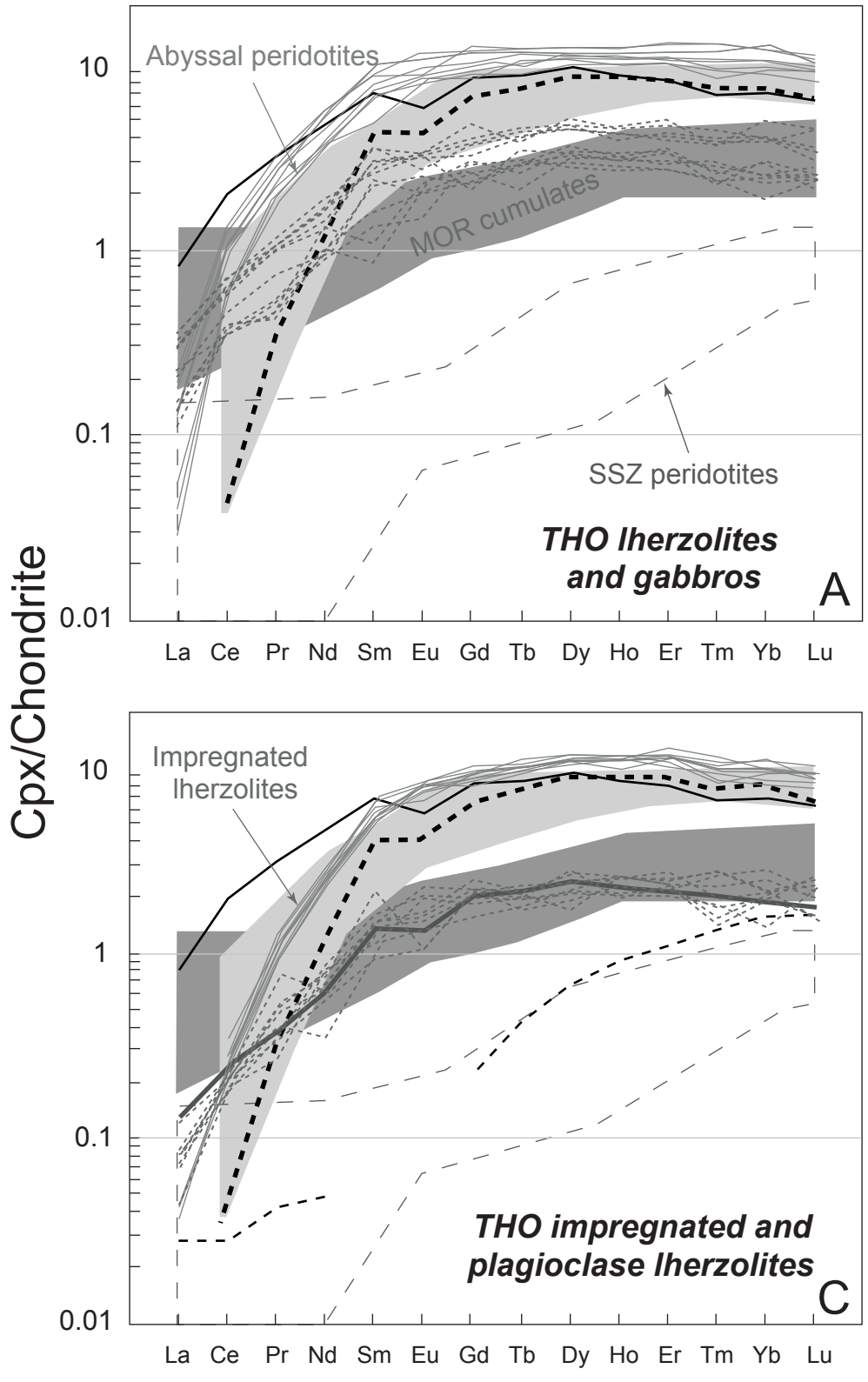
Abyssal peridotites
MOR cumulates
SSZ peridotites
THO lherzolites
and gabbros
A
Cpx/Chondrite
10
1
0.1
0.01
La Ce Pr Nd Sm Eu Gd Tb Dy Ho Er Tm Yb Lu

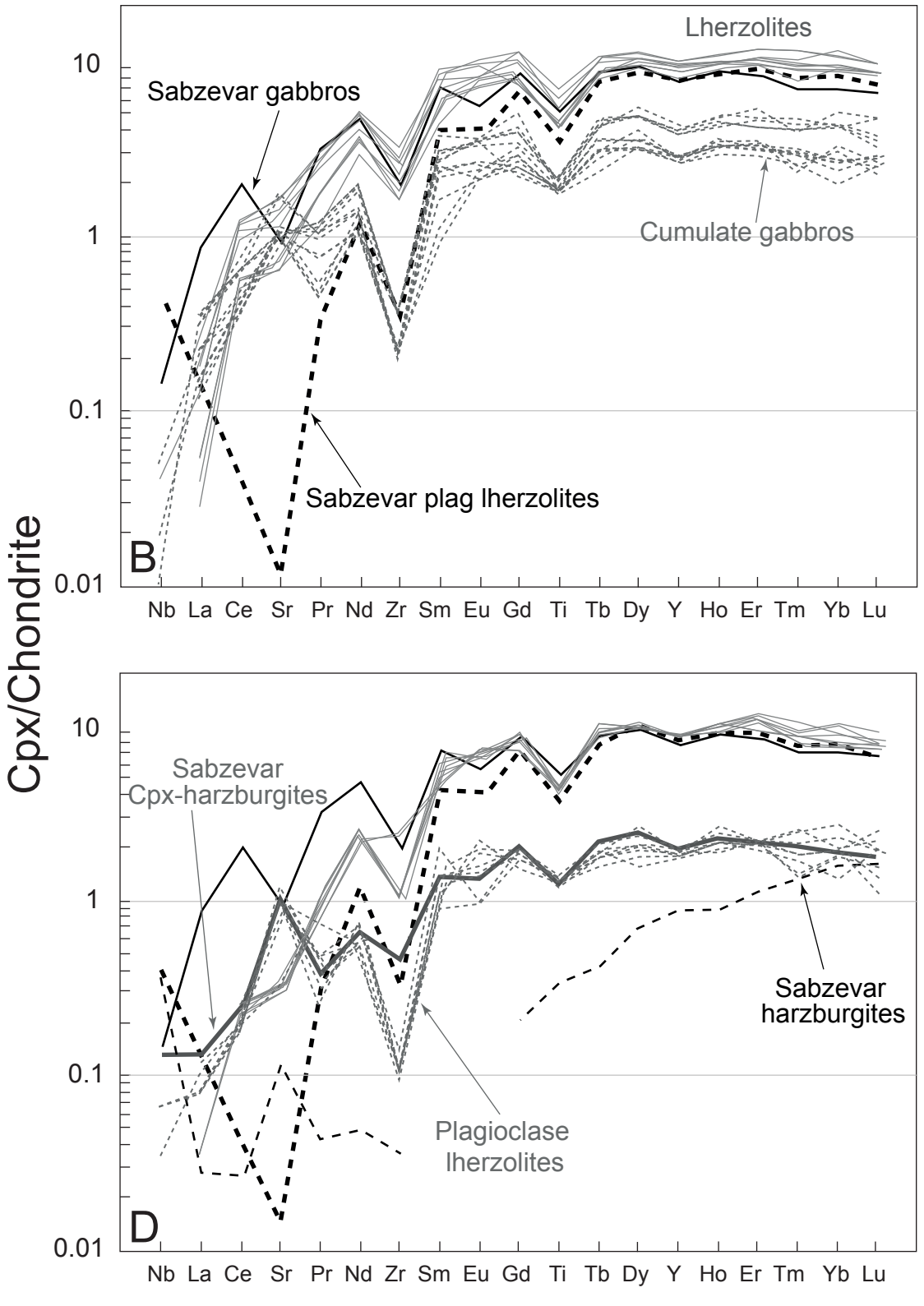
Lherzolites
Sabzevar gabbros
Cumulate gabbros
Sabzevar plag lherzolites
B
Cpx/Chondrite
10
1
0.1
0.01
Nb La Ce Sr Pr Nd Zr Sm Eu Gd Ti Tb Dy Y Ho Er Tm Yb Lu

Impregnated
lherzolites
THO impregnated and
plagioclase lherzolites
C
Cpx/Chondrite
10
1
0.1
0.01
La Ce Pr Nd Sm Eu Gd Tb Dy Ho Er Tm Yb Lu

Sabzevar
Cpx-harzburgites
Sabzevar
harzburgites
Plagioclase
lherzolites
D
Cpx/Chondrite
10
1
0.1
0.01
Nb La Ce Sr Pr Nd Zr Sm Eu Gd Ti Tb Dy Y Ho Er Tm Yb Lu

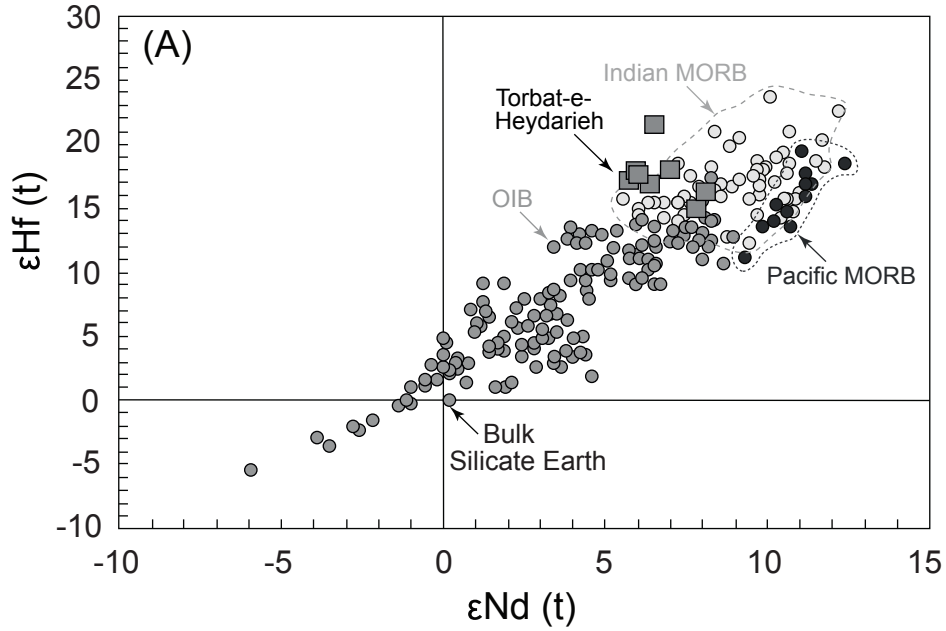
(A)
Indian MORB
Torbat-e-
Heydarieh
OIB
Pacific MORB
Bulk
Silicate Earth
εHf (t)
εNd (t)
30
25
20
15
10
5
0
-5
-10
-10
-5
0
5
10
15

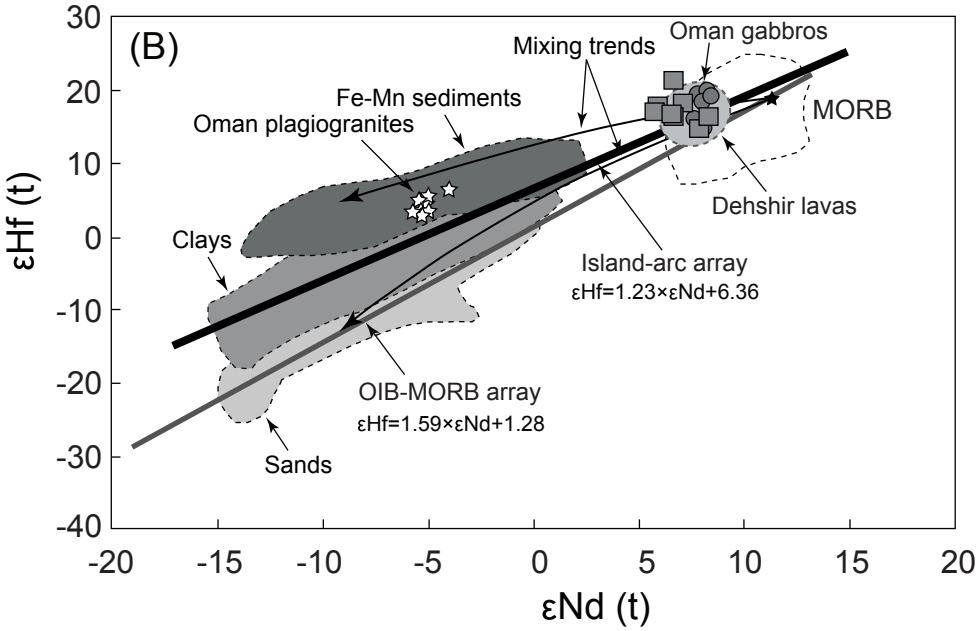
(B)
Mixing trends
Oman gabbros
Fe-Mn sediments
Oman plagiogranites
MORB
Dehshir lavas
Clays
Island-arc array
εHf=1.23×εNd+6.36
OIB-MORB array
εHf=1.59×εNd+1.28
Sands
εHf (t)
εNd (t)
30
20
10
0
-10
-20
-30
-40
-20
-15
-10
-5
0
5
10
15
20

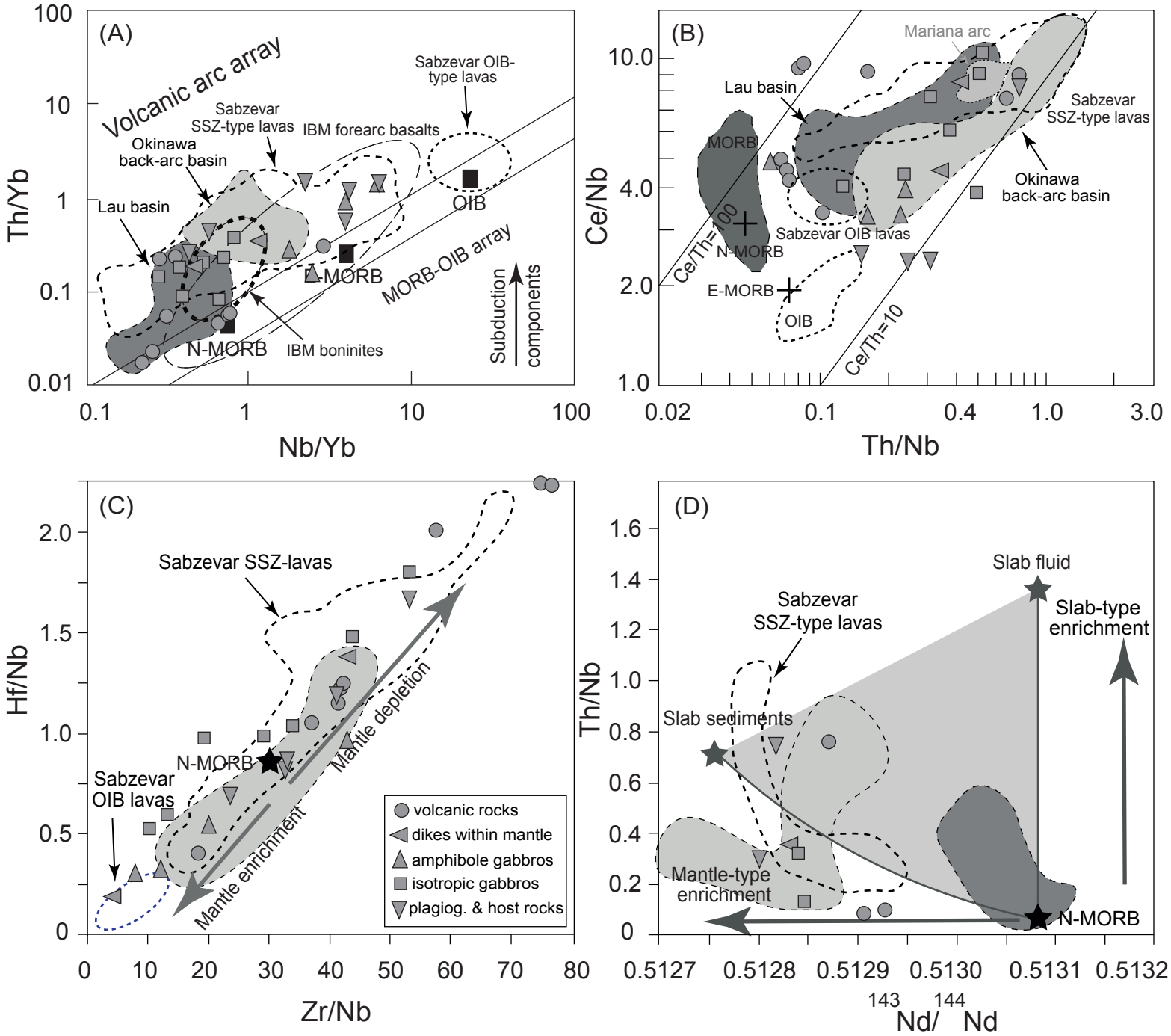
(A)
Volcanic arc array
Sabzevar OIB-type lavas
Sabzevar SSZ-type lavas
IBM forearc basalts
Okinawa back-arc basin
Lau basin
OIB
E-MORB
MORB-OIB array
Subduction components
N-MORB
IBM boninites
Th/Yb
Nb/Yb
(B)
Mariana arc
Lau basin
Sabzevar SSZ-type lavas
MORB
Okinawa back-arc basin
Sabzevar OIB lavas
N-MORB
Ce/Th=100
E-MORB
OIB
Ce/Th=10
Ce/Nb
Th/Nb
(C)
Sabzevar SSZ-lavas
N-MORB
Sabzevar OIB lavas
Mantle depletion
Mantle enrichment
volcanic rocks
dikes within mantle
amphibole gabbros
isotropic gabbros
plagiog. & host rocks
Hf/Nb
Zr/Nb
(D)
Slab fluid
Sabzevar SSZ-type lavas
Slab-type enrichment
Slab sediments
Mantle-type enrichment
N-MORB
Th/Nb
143Nd/144Nd

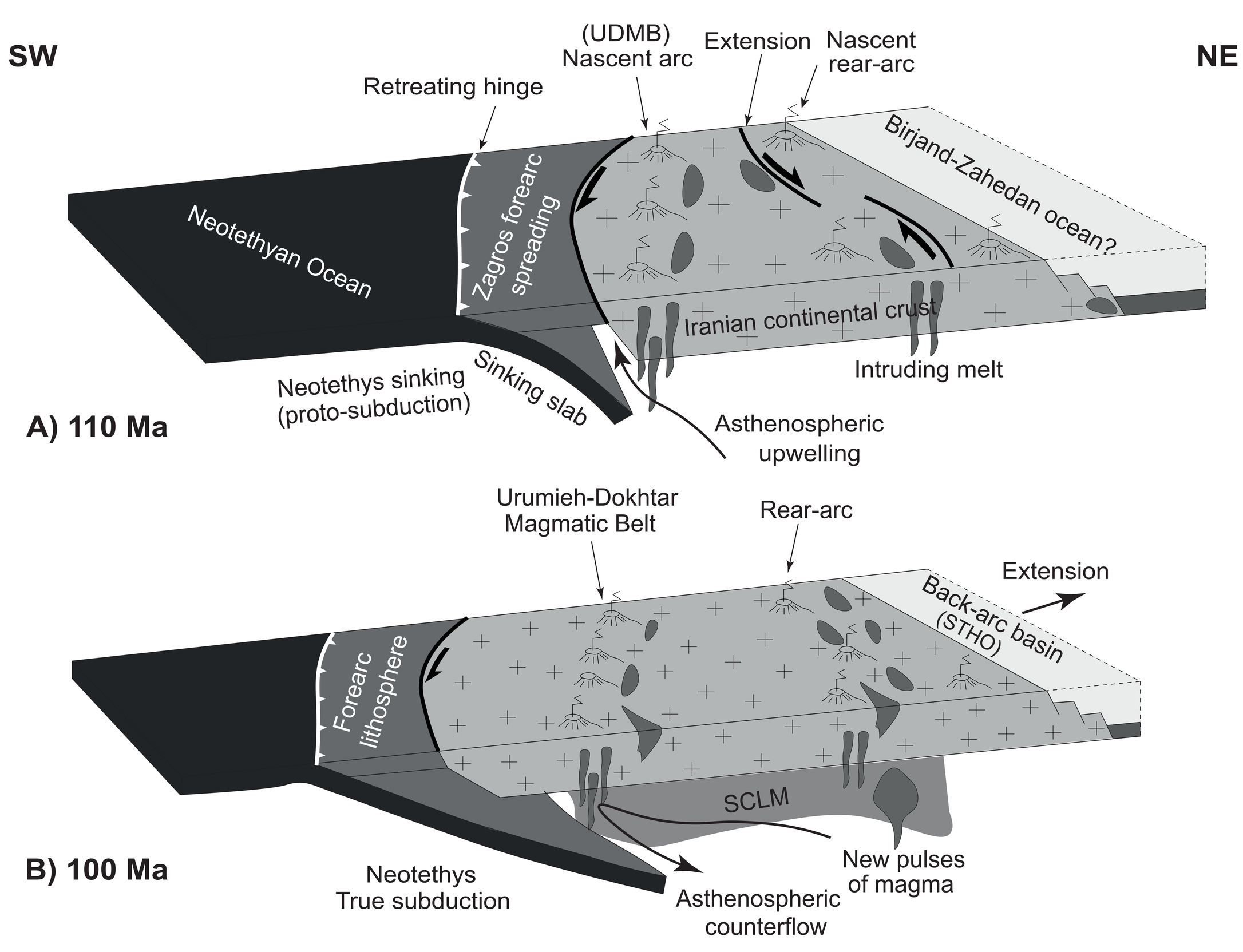
SW
NE
(UDMB)
Nascent arc
Extension
Nascent
rear-arc
Retreating hinge
Birjand-Zahedan ocean?
Neotethyan Ocean
Zagros forearc
spreading
Iranian continental crust
Intruding melt
Neotethys sinking
(proto-subduction)
Sinking slab
A) 110 Ma
Asthenospheric
upwelling
Urumieh-Dokhtar
Magmatic Belt
Rear-arc
Extension
Back-arc basin
(STHO)
Forearc
lithosphere
SCLM
B) 100 Ma
Neotethys
True subduction
Asthenospheric
counterflow
New pulses
of magma